BAND Analysis Note

F. Hauenstein[1,2], E. Segarra[2], T. Kutz[2,3], D. Nguyen[4], C. Fogler[1], A. Denniston[2], and J. Estee[2]

[1]Old Dominion University, Norfolk, VA 23529
[2]MIT, Cambridge, MA
[3]George Washington University, Washington, D.C.
[4]Jefferson Lab

July 14, 2022

Contents

1 Introduction

The BAND detector has been added to the CLAS12 detector in Winter 2018 for tagged high-momentum neutron measurements in very backward direction. The main physics of interest is the measurement of the nucleon modification of highly-virtual high-momentum protons in deuterium. For this purpose, we are interested in $d(e, e'n_S)X$ events, where the electron is detected in the forward detector of CLAS12 while the recoil spectator neutron is detected in BAND.

Data for our measurement has been collected during the RGB data collection period in Spring 2019 and Winter 2019/2020 at various beam energies between 10-11 GeV and at about 4.2 GeV for calibration purposes. All of our data uses the inbending torus setting. We do not use the outbending data from Fall 2019 in this analysis. We are showing results from each of these run periods separately as well as combined. The final plot is a data/MC ratio for tagged events where we are most sensitive to the nucleon modification and a lot of systematic effects cancel to first order.

This document describes in details of the data analysis for the tagged ratio plot. We are showing the used generators in MC for comparisons, the electron and neutron selection cuts for the analysis. Methods for background subtraction of accidental neutrons in BAND and selection of good runs from the different beam times. We also give comparisons of inclusive and tagged events to MC which show very good agreement in shape but not on an absolute scale. We also discuss some of the systematics investigated so far.

Other details about the analysis framework, BAND calibration and detector implementation in GEMC can be found the BAND technical note [7].

1.1 Definition of kinematic variables

From the scattered electron detected in CLAS12, the standard inclusive kinematic variables can be reconstructed in terms of the four momentum of the initial electron

$k = (\overline{k}, E)$, fixed target $P = (0, M)$, and scattered electron $k' = (\overline{k}', E')$

$$\nu = E - E'$$
$$Q^2 = -q^2 = -(k - k')^2$$
$$x_B = \frac{Q^2}{2M\nu}$$
$$W^2 = (P + q)^2$$
$$y = \frac{\nu}{E}$$

If a DIS event is tagged with a recoiling high-momentum neutron $p_n = (\overline{p}_n, E_n)$, one can construct variables sensitive to the proton's initial momentum within the nucleus, $\overline{p}_i = -\overline{p}_n$ (in the regime of interest where the proton and neutron are in a short-range correlated state). Additional tagged kinematic variables can then be reconstructed:

$$(W')^2 = (p_i + q)^2$$
$$x' = \frac{Q^2}{(W')^2 - M_n^2 + Q^2}$$
$$\alpha_S = \frac{E_n - |\overline{p}_n| \cos\theta_{nq}}{M_n}$$

. The "primed" tagged variables x' and W' are analogous to the the inclusive x_B and W, but accounting for the proton's initial momentum within the nucleus. The variable α_S is the lightcone momentum fraction of the spectator neutron, and depends on θ_{nq}, the angle between the recoiling neutron and the virtual photon.

1.2 Tagged double ratio

Our observable of interest involves a ratio of experimental to theoretical yields. The experimental yield is obtained from our tagged DIS data, while the theoretical yield is obtained from events generated with a theory cross section model and propagated through a full GEANT4 simulation of the experimental apparatus.

A standard procedure for obtaining experimental Born cross sections is the yield ratio method:

$$\sigma_{exp}^{Born} = \frac{Y_{exp}}{Y_{sim}} \sigma_{theory}^{Born} \tag{1}$$

where Y_{exp} is the experimental yield, Y_{sim} is the simulated yield, and σ_{theory}^{Born} is the Born-level theoretical cross section that is used to generate the simulated events.

After QED radiative effects are applied to the generated events, they must be run through a simulation that accurately models the apparatus and detectors in order to properly account for experimental effects such as bin migration and detector acceptance. The experimental to simulated yield ratio can thus be described as the ratio of the experimental to theoretical Born cross section:

$$\frac{\sigma_{exp}^{Born}}{\sigma_{theory}^{Born}} = \frac{Y_{exp}}{Y_{sim}} \tag{2}$$

Thus, if the simulation used to obtain the simulated yields accurately models the experimental apparatus, the ratio of experimental to simulated yields is equivalent to the ratio of the experimental to theoretical cross sections.

This experimental to theoretical ratio is used to form a double ratio, but individually normalizing the data and simulated yields (which are functions of x') by the yield at a fixed kinematic point x'_0:

$$R_{tag} = \frac{Y_{exp}(x')/Y_{exp}(x' = x'_0)}{Y_{sim}(x')/Y_{sim}(x' = x'_0)} \tag{3}$$

The normalization to a fixed kinematic point results in the exact cancellation of the experimental and simulated luminosity, and the partial cancellation of the neutron detection efficiency. Residual effects due to possible momentum dependence of the neutron detection efficiency are discussed in Section 9.1. Furthermore, acceptance and bin migration effects in CLAS12 cancel to first order.

In this analysis, we have chosen the fixed kinematic point for normalization to be $x' = 0.3$. While to some extent this is an arbitrary choice, inclusive measurements of the EMC effect in nuclei tend to be close to unity in the vicinity of $x \approx 0.3$, indicating the minimization (or at least large cancellation) of nuclear effects. Thus our choice normalizes to a point where one expects the EMC effect to be smallest.

Following the logic of Equation 2, this double ratio is equivalent to the double ratio of experimental to theoretical cross sections:

$$R_{tag} = \frac{\sigma_{exp}(x')/\sigma_{exp}(x' = x'_0)}{\sigma_{theory}(x')/\sigma_{theory}(x' = x'_0)} \tag{4}$$

The theoretical cross section model used to generate neutron-tagged DIS events for the simulated yield will require the proton structure function F_2^p as input. The free proton structure has been thoroughly mapped by inclusive DIS measurements, while our neutron-tagged DIS measurement is senstive to the structure of protons bound in deuterium. If our input model uses the free proton structure function as input, and in the limit of no rescattering of the recoil neutron (i.e., PWIA), then the double ratio is sensitive to the ratio of the bound to free proton cross section. Finally, under the standard assumption that $\sigma_A/\sigma_B = F_2^A/F_2^B$, the double-ratio is proportional to ratio of the bound to free proton structure:

$$R_{tag} \propto \frac{F_2^* \left(x'\right) \Big/ F_2^* \left(x' = x'_0\right)}{F_2 \left(x'\right) \Big/ F_2 \left(x' = x'_0\right)} \tag{5}$$

2 Monte Carlo Generators and Smearing

This chapter describes the various event generators used in our GEMC simulations as well as the further smearing applied on reconstructed MC events.

For all simulations, we use `GEMC 4.4.1` with a custom GCARD for RGB, where BAND and upstream geometry implemented. Details of the GEMC implementation of BAND and other upstream material between the detector and the target can be found in the BAND technical note [7]. We used the same GCARD for inclusive and tagged simulations for consistency. All three beam energies were simulated (10.2, 10.4, and 10.6 GeV) separately. Each inclusive simulation included background merging in GEMC using random trigger data taken at 50 nA for 10.2, 40 nA for 10.4, and 50 nA for 10.6 GeV.

We have an inclusive event generator using the deuteron structure function and tagged exclusive generators based on Plane-Wave Impulse Approximation(PWIA) models. We generated events for each of the beam energies separately with a statistics of 25 to 100 million depending on the channel and generator of interest.

2.1 Generators

For the simulation of tagged events, an event generator was implemented using a cross section model based on the formalism of Ref. [14]. This uses the Plane-Wave Impulse Approximation (PWIA) to factorize the cross section for deep-inelastic scattering from a neutron in the deuteron in terms of the light-front spectral function of the deuteron. The only change made consisted of interchanging the proton and the neutron, as in this measurement the scattering from the bound proton was observed. The formalism was used to construct a differential cross section for spectator-tagged DIS from the deuteron:

$$\frac{d\sigma[ed \to e'Xn]}{dx_B dQ^2 d\phi_{e'} \frac{d\alpha_s d^2\mathbf{p}_s^\perp}{\alpha_s}} = \frac{2\alpha_{em}^2 y^2}{(2-\alpha_s)Q^6} w_{\mu\nu} W_N^{\mu\nu}(p,\tilde{q}) S(\alpha_s, \mathbf{p}_s^\perp) \tag{6}$$

The spectral function is

$$S(\alpha_s, \mathbf{p}_s^\perp) = \frac{\sqrt{m_N^2 + k^2}}{2-\alpha_s} |\tilde{\phi}(k)|^2 \tag{7}$$

where

$$k^2 = \frac{m_N^2 + \left(\mathbf{p}_s^\perp\right)^2}{\alpha_s(2-\alpha_s)} - m_N^2 \tag{8}$$

was taken from the model of Ref. [13], using the AV18 interaction to describe the momentum distribution $|\tilde{\phi}(k)|^2$. The proton structure functions were taken from Ref. [8].

This cross section was used to construct a weighted event generator. For a given event, the following procedure was used:

The generating variables x_B, Q^2, $\phi_{e'}$, α_s, and $\mathbf{p}_s^\perp$ were sampled from a phase-space distributions of choice:

$$x_B,\ Q^2,\ \phi_{e'},\ \alpha_s,\ \mathbf{p}_s^\perp \sim P(x_B, Q^2, \phi_{e'}, \alpha_s, \mathbf{p}_s^\perp) \tag{9}$$

The kinematics of the event were calculated, being fully constrained by the selected variables. From this, the differential cross section was evaluated at the selected variables. The weight of the event was then calculated using the ratio between the cross section and the generating function:

$$w_i = \frac{1}{P(x_B, Q^2, \phi_{e'}, \alpha_s, \mathbf{p}_s^\perp)} \frac{d\sigma[ed \to e'Xn]}{dx_B dQ^2 d\phi_{e'} d\alpha_s d^2\mathbf{p}_s^\perp} \tag{10}$$

This process was used to produce a large number of weighted events distributed across the measured phase space, with weights spanning many orders of magnitude. To avoid spending computational resources simulating many events with relatively small weights, weighted random sampling (WRS) was used to select a subset of events according to the weight distribution. This resulted in a set of unweighted events distributed according to the model cross section.

A fully inclusive event generator, independent of PWIA factorization and using the deuterium structure function, was also used for comparisons to data.

All events are generated at the scattering vertex. While external radiative effects after scattering are handled by GEANT4, external radiative effects prior to scattering must be applied in the generator. External Bremsstrahlung was applied following the formalism described in Section IV.B of Ref. [12].

Internal radiation was applied using the `RADGEN` subroutine from the `clasdis` event generator. `RADGEN` was used to calculate the ratio of the radiated to Born cross section, $w_{rad} = \sigma_{rad}/\sigma_{Born}$, in a fine grid covering the relevant range of (x_B, Q^2). Two such tables were produced, for deuterium and proton. For inclusive scattering from deuterium, the radiative effects were taken to be

$$w_{rad}^{inc} = \frac{\sigma_{rad}^D(x_B, Q^2)}{\sigma_{Born}^D(x_B, Q^2)}, \tag{11}$$

while for tagged scattering from the bound proton, the radiative effects were taken to be

$$w_{rad}^{tag} = \frac{\sigma_{rad}^{p}(x', Q^2)}{\sigma_{Born}^{p}(x', Q^2)}. \tag{12}$$

These tables were used to interpolate the value of w_{rad} for each generated event, which was added as a multiplicative factor in the event weight.

A number of systematic checks were performed to validate the sampling methods and ensure consistency of the cross section models (both internally and with other available generators).

To validate the algorithm used to perform WRS on a population of weighted events, two generator samples were produced. The first sample contained weighted events, and the second sample used the WRS algorithm to produce unweighted events distributed according to the cross section. Two-dimensional plots showing correlations between key generated values (momentum and angles of the generated electron and neutron) are shown in Figure 1. As can be seen, the WRS preserves both the shape and normalization of the weighted events.

As a check of both the input cross section model, and its technical implementation in the generator, our generated distributions were also compared to a similar tagged DIS generator authored by W. Cosyn (based on [11]). Figure 2 shows a comparison of the generated electron and neutron vectors, and Figure 3 shows a comparison of some resulting tagged kinematic variables. The two generators largely agree, with $\leq 20\%$ discrepancies in shape and normalization.

Lastly, the internal consistency of the BAND generators was checked by comparing the inclusive generator to the PWIA generator integrated over all of deuterium. For the tagged DIS analysis, events of interest involve scattering from the proton in deuterium with a high-momentum recoil spectator neutron. If the PWIA generator includes scattering from either nucleon in deuterium, integrated over the entire deuterium wavefunction (not just the high-momentum region), one effectively obtains inclusive DIS events. Figure 4 shows the comparison of generated electron vectors and inclusive DIS variables between the standard inclusive generator and integrated PWIA generator. The shape and normalization of the two generators agree to better than 20% (aside from a larger discrepancy on the lower edge of the generated x_B range).

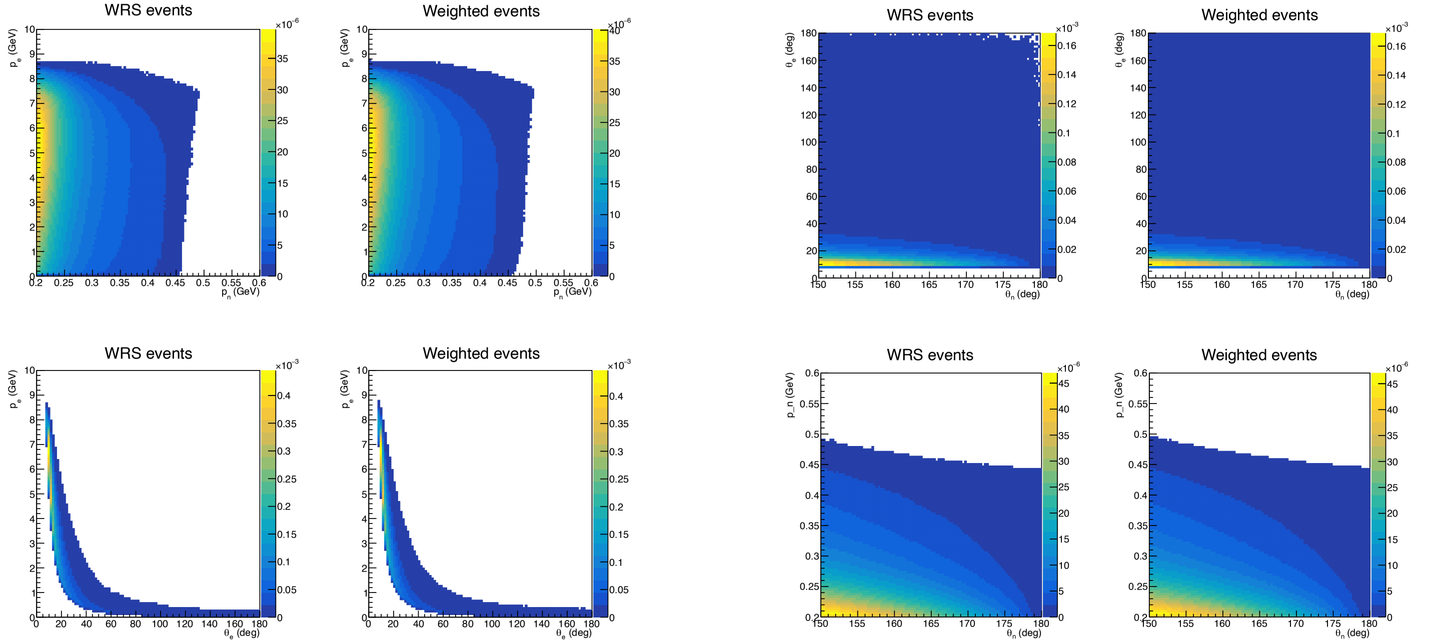

Figure 1: Comparisons of various correlations between momentum and angles of generated electrons and neutrons. For each pair of distributions, the left figure is from WRS generator samples, while the right figure is from weighted samples.

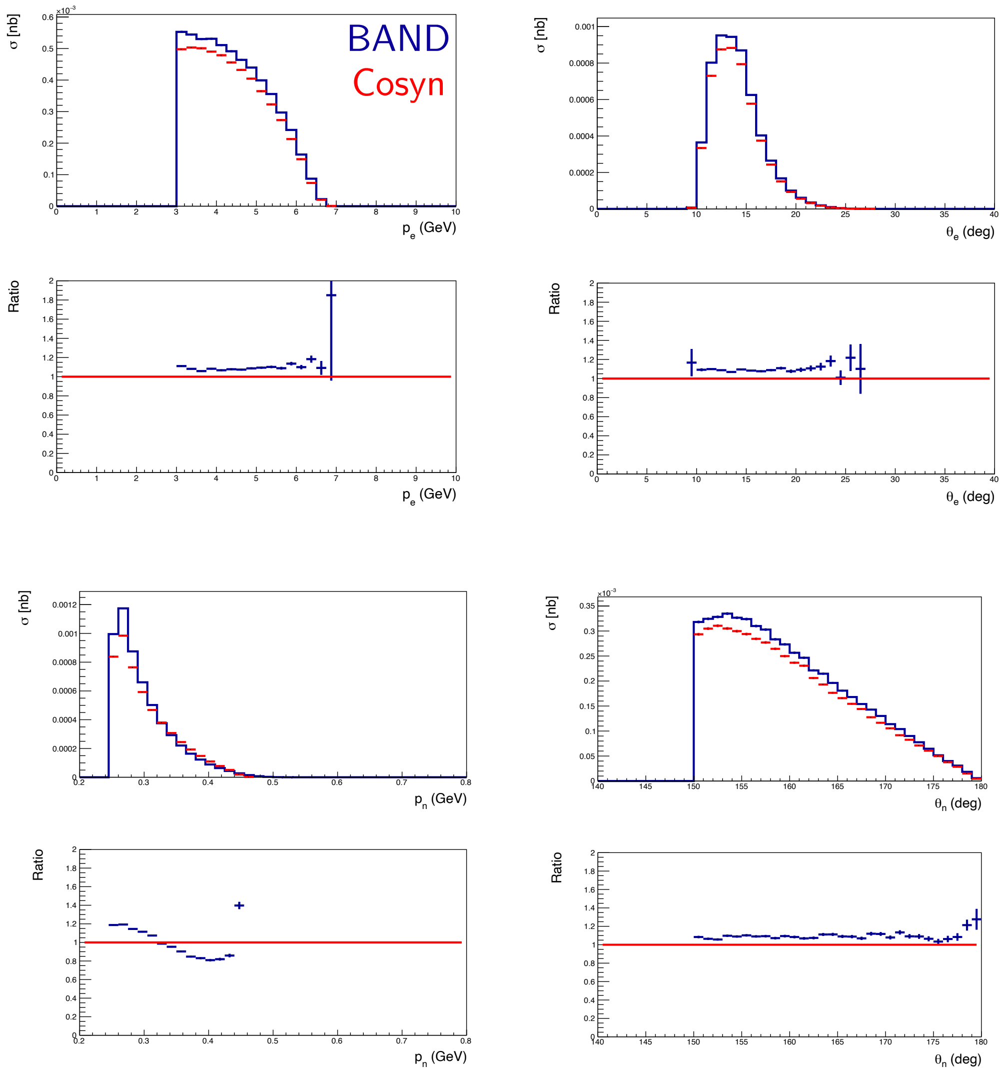

Figure 2: Comparisons of electron and neutron variables from the PWIA generator used for the BAND analysis (based on Ref. [14]) with the independent PWIA generator from W. Cosyn (based on Ref. [11]).

2.2 Smearing

We looked at $d(e,e'p)$ distributions to compare resolutions in simulation versus data for the low energy runs (LER) at 4.2 GeV in Winter 2019. For that purpose, we used a quasi-elastic generator based on PWIA and proton momentum distribution.

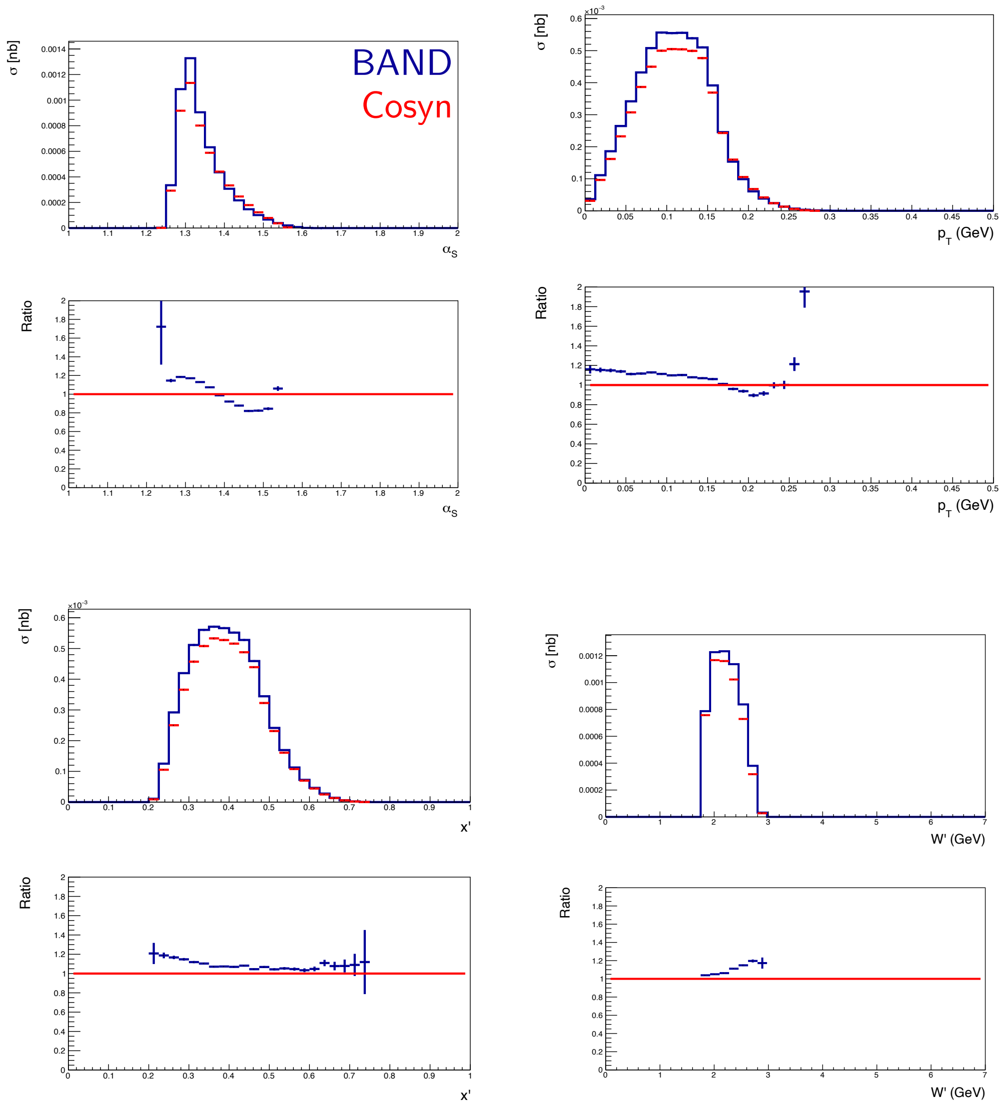

Figure 3: Comparisons of tagged kinematic variables from the PWIA generator used for the BAND analysis (based on Ref. [14]) with the independent PWIA generator from W. Cosyn (based on Ref. [11]).

In this case the proton is detected in CLAS12. The electron selection uses the same cuts as the tagged analysis (see Section 3). For the proton selection, we applied event builder PID and χ^2_{PID} cuts.

We found that the missing mass distributions in data and simulation were in-

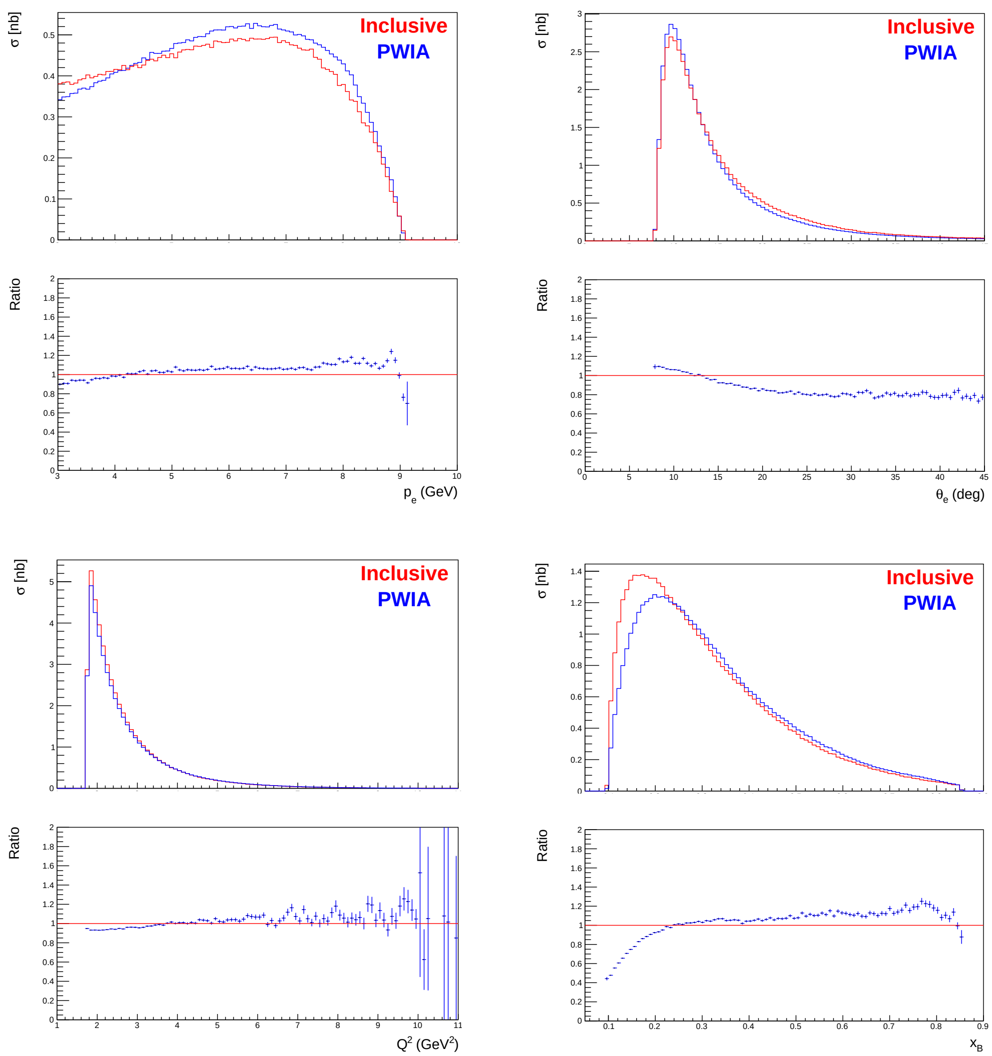

Figure 4: Comparison of electron and inclusive DIS variables obtained from the standard inclusive generator (using F_2^D as input) and the integrated PWIA generator (using F_2^p and F_2^n as input).

consistent. While the shape and peak center agreed, the missing mass width of data was more than double the simulation width (Fig. 5).

Run Group A has extracted electron smearing functions from elastic scattering (private communication with FX Girod and Giovanni Angelini). The total smearing of the electron momentum variables is represented by the following functional forms

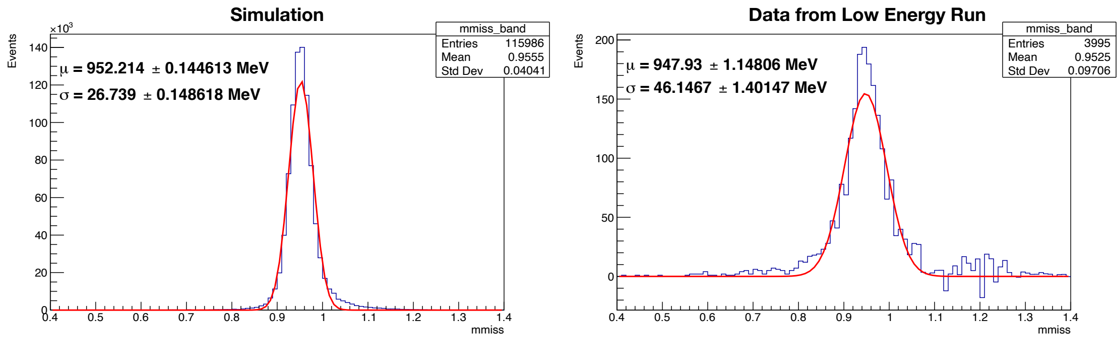

Figure 5: (Left) width of d(e,e'p) missing mass peak for simulation using GEMC. (Right) width of d(e,e'p) missing mass peak for low energy run data. Note the discrepancy between the widths of the data and the simulation.

defined from RG-A.

$$\sigma_{\frac{\Delta p}{p}} = c_0(c_1 + c_2\theta + c_3\theta^2 + c_4\theta^3 + c_5\theta^4)\sqrt{(}p^2 + c_6^2) \tag{13}$$

$$\sigma_{\Delta\theta} = c_0\sqrt{(c_1\theta + c_2)^2 + (c_3\theta + c_4)^2\frac{p^2 + c_5^2}{p^4}} \tag{14}$$

$$\sigma_{\Delta\phi} = c_0\sqrt{(c_1\theta + c_2)^2 + (c_3\theta + c_4)^2\frac{p^2 + c_5^2}{p^4}} \tag{15}$$

The values of the parameters where extracted from elastic scattering in RG-A. To account for the discrepancy between data and simulation, we applied the RG-A electron smearing to our data set. After smearing, our missing mass widths become consistent (see Fig. 6).

Therefore, we implement this smearing in our analysis framework. The MC to data comparisons in this note use the smeared electron momentum vector and corresponding kinematic values.

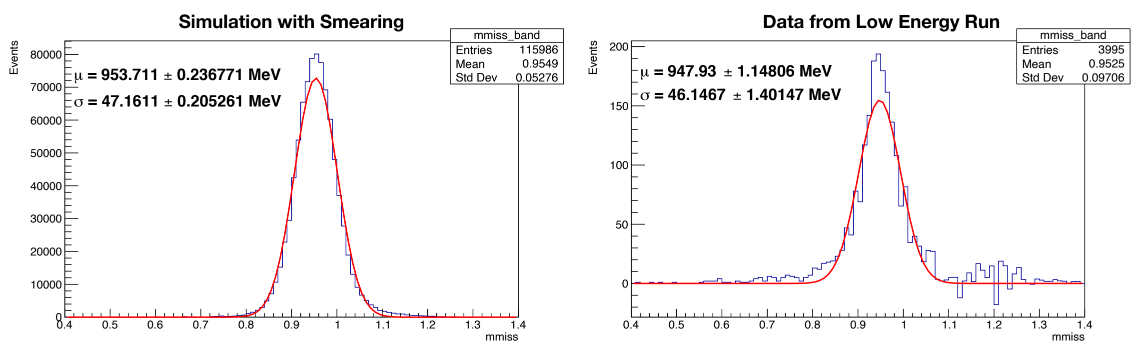

Figure 6: (Left) width of d(e,e'p) missing mass peak for simulation with RG-A smearing included. (Right) width of d(e,e'p) missing mass peak for low energy run data.

3 Particle Selection Cuts

This chapter describes the electron cuts (PID and fiducial), further detector fiducial cuts due to problematic detector channels and the neutron selection cuts. The selection of electrons are based on procedures from the RGA analysis note [10]. These selections are implemented in our *bandsoft_tools* skimmers (see [7]) and used to select events with a good electron and/or a neutron. Overall, we used the same selection methods for the different beam energy data sets of RGB (10.2, 10.4, 10.6 and 4.2 GeV). Only inbending data is considered in this analysis.

3.1 Electron Fiducial Cuts

3.1.1 DC fiducial cuts

The parameters for DC fiducial cut in this analysis comes from the RGA fitting procedure using a linear cut in the local xy-plane approaches. The DC fiducial cuts based on the distribution of χ^2/NDF from the track. In bins of x and y the average tracking χ^2/NDF is calculated. The y was sliced into 15 bins between 25.7 cm and 151.2 cm, 28.8 cm and 262.8 cm, 31.8 cm and 355.8 cm in region 1, 2 and 3 respectively. In each slice of y, the x distribution of averaged χ^2/NDF is analyzed. The center of this distribution are fitted with a constant around $x = 0\,\text{cm}$. Then the x values are determined where 20% increase or 50% decrease in the averaged χ^2/NDF level is reached compared to the fitted value at center, whichever occurs first. The DC fiducial cuts from RGA are applied on RGB data as shown in Fig. 7 and Fig. 8. The survival rate for electron are determined by the fraction of event what passed the cuts. It is consistent between the RGA and RGB data (both 10.2 GeV and 10.6 GeV) as well as the RGB simulation. The comparison is summary in Table 1. This was shown also at the RGB meeting in December 4, 2020 (here)

	RGA (%)	RGB(10.2 GeV) (%)	RGB(10.6 GeV) (%)	RGBGEMC (%)
Region 1	97.7	97.6	97.5	97.6
Region 2	98.4	98.3	98.3	97.7
Region 3	95.7	94.9	94.7	93.9

Table 1: Electron survival rate

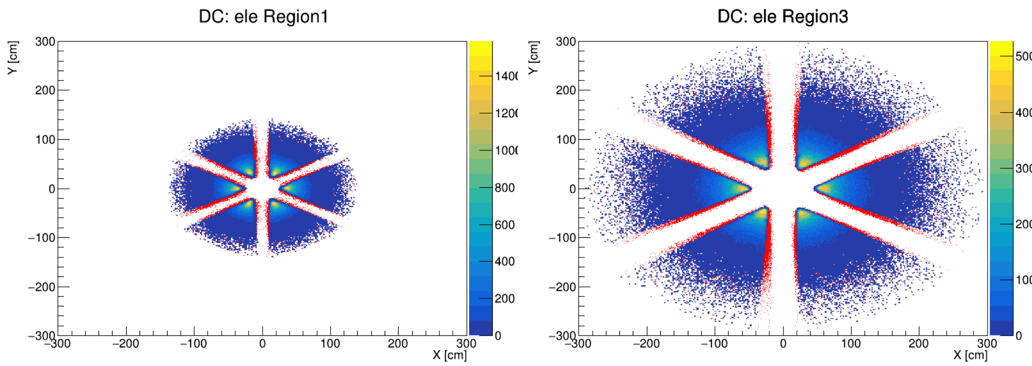

Figure 7: The event distribution as function of DC xy position from RGB, 10.2 GeV data. The red and the colored are before and after DC-fiducial cuts using RGA parameters. The left and right plots are for region 1 and region 3, respectively.

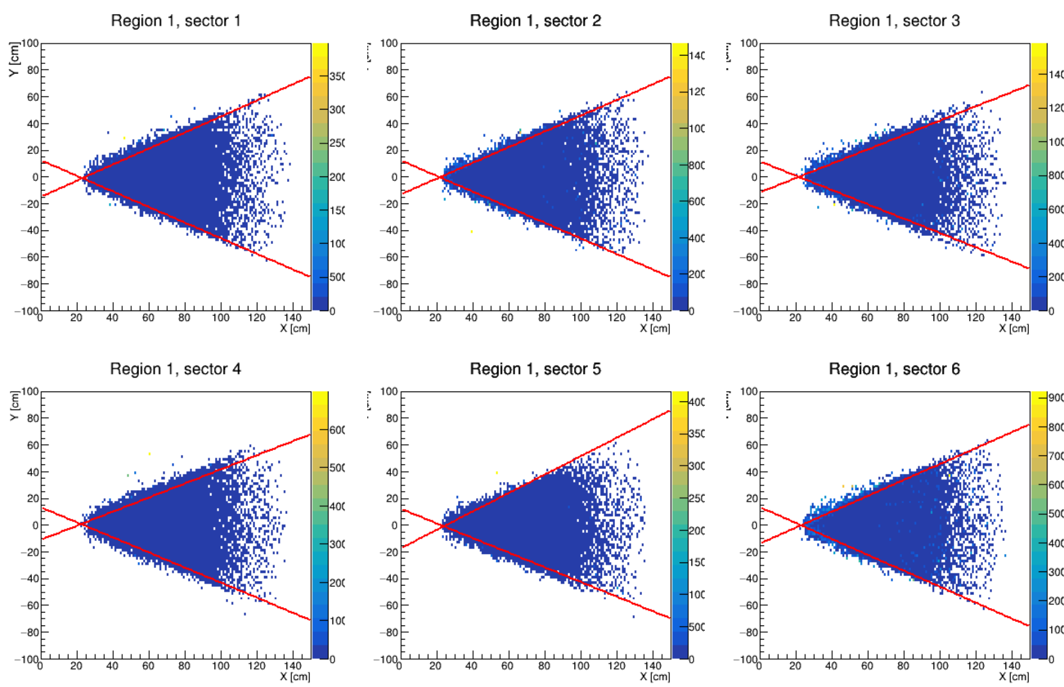

Figure 8: The average $\chi 2/\mathrm{NDF}$ distribution as a function of DC rotated xy positions for region 1 for 6 sectors. The red lines show the xy linear DC-fiducial cuts using the RGA's parameters.

3.1.2 Calorimeter Cuts

Fiducial cuts are placed on the edges of the calorimeter to reduce events where the electromagnetic shower was not fully contained in the detector. The sampling calorimeter is made up of alternating layers of lead and scintillators. Our fiducial cut should be placed between scintillators. We chose to cut out the two outermost scintillators on the sides of each calorimeter. Fig. 9 and Fig. 10 show the sampling faction of the hits over the range of hit position for Run 6437 of RGB. We also checked other runs for consistency of the cut. We choose a cut value of 14 cm consistent with the cuts from RGA (see also RGB meeting slides at (here)).

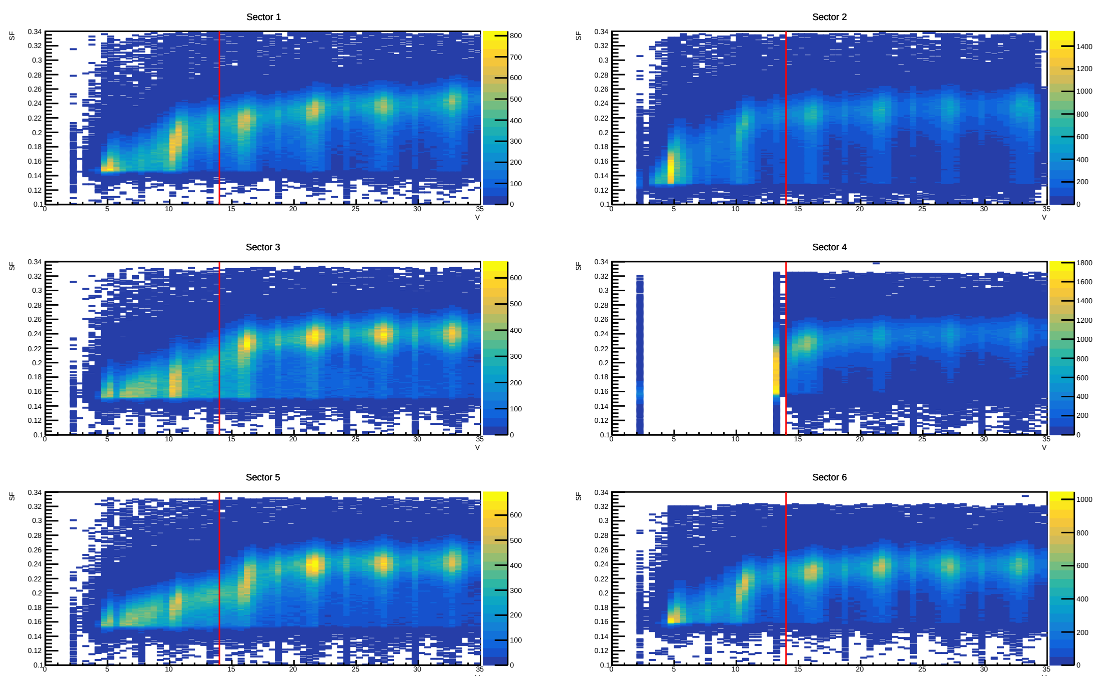

Figure 9: Sampling Fraction vs. electron hit position in coordinate V. The red line denotes the location of the cut at 14 cm to the two outer scintillators.

3.2 Electron PID

In this analysis of the RGB data set, an event is defined by an electron detected in the Forward Detector of CLAS. To identify a negatively charged particle traveling through the FD, the torodial magnetic field is configured to bend negative particles

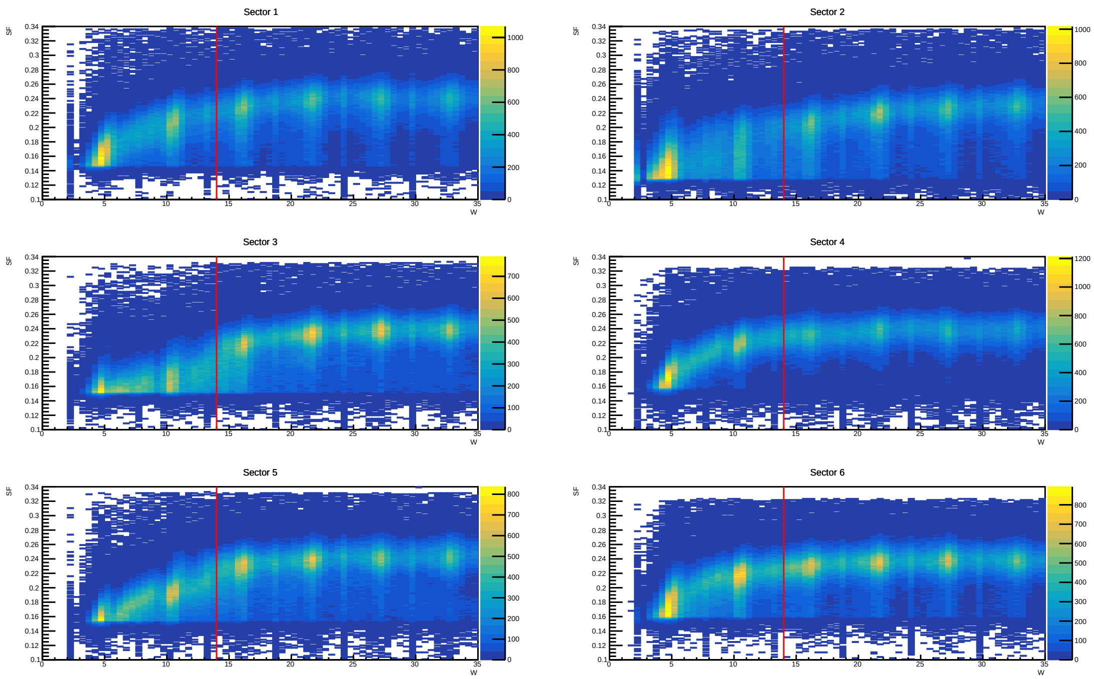

Figure 10: Sampling Fraction vs. electron hit position in coordinate W. The red line denotes the location of the cut at 14 cm to the two outer scintillators.

outward. However, electrons can be confused with negatively charged minimum ionizing particles such as π^-. To minimized this effect, CLAS is equiped with a HTCC and ECAL that can help with e^- PID at low and high momentum respectively. Table 2 shows the cuts we place on the PID for the FD electron

3.2.1 Sampling Fraction Cut

To obtain the sampling fraction cut as a function of E_{PCAL}, SF distributions are produced in small bins of E_PCAL and fit to Gaussian functions for each sector separately. The means and sigmas of these individual distributions can then be fit to the following functional form:

$$\mu_{SF}(x) = a + \frac{b}{x} + \frac{c}{x^2} \tag{16}$$

Cut	Limits	Notes
Charge	-1	
Event Builder PID	11	
SF vs E_{PCAL}	$\pm 5\sigma$	Sector Dependent
SF vs p	$\pm 5\sigma$	Sector Dependent
SF of $PCAL + EC_{in}$	$\frac{E_{PCAL}+E_{ecin}}{p} > 0.2$	only for e^- with $p > 4.5\,\mathrm{GeV}$

Table 2: Overview of Electron PID cuts.

$$\sigma_{SF}(x) = a + \frac{b}{x} + \frac{c}{x^2} \tag{17}$$

The results of the fit can then be used to cut out events when the Sampling Fraction is 5σ away from the mean as a function of E_{PCAL}. This must be done for each sector individually.

The fits were made for the 10.2 GeV, 10.4 and 10.6 GeV run periods separately. The fits were also cross check with a few individual runs over the run periods to confirm that there were no significant changes over the run period. The data from run number 6437 is shown in Fig. 11 along with the location of this cut.

This procedure was repeated for the Sampling fraction as a function of e^- momentum after the initial cut was already made. This can be see in Fig. 14 along with the location of this cut.

3.2.2 PCAL and ECAL Correlation Cut

At HTCC threshold of 4.5 GeV there is a significant pion contamination (see RGA note [**RGAnote**]). So another cut is made on the correlation between the $PCAL_{dep}$ and $ECAL_{in,dep}$. The cut is the following:

$$\frac{E_{PCAL} + E_{ecin}}{p} > 0.2 \quad \text{if} \quad p > 4.5\,\mathrm{GeV} \tag{18}$$

The data before and after this cut is shown in Fig. 13. After all cuts, the sampling fraction versus electron momentum is shown in Fig. 14.

The electron PID cuts were also shown at the RGB meeting on December 4, 2020 (here).

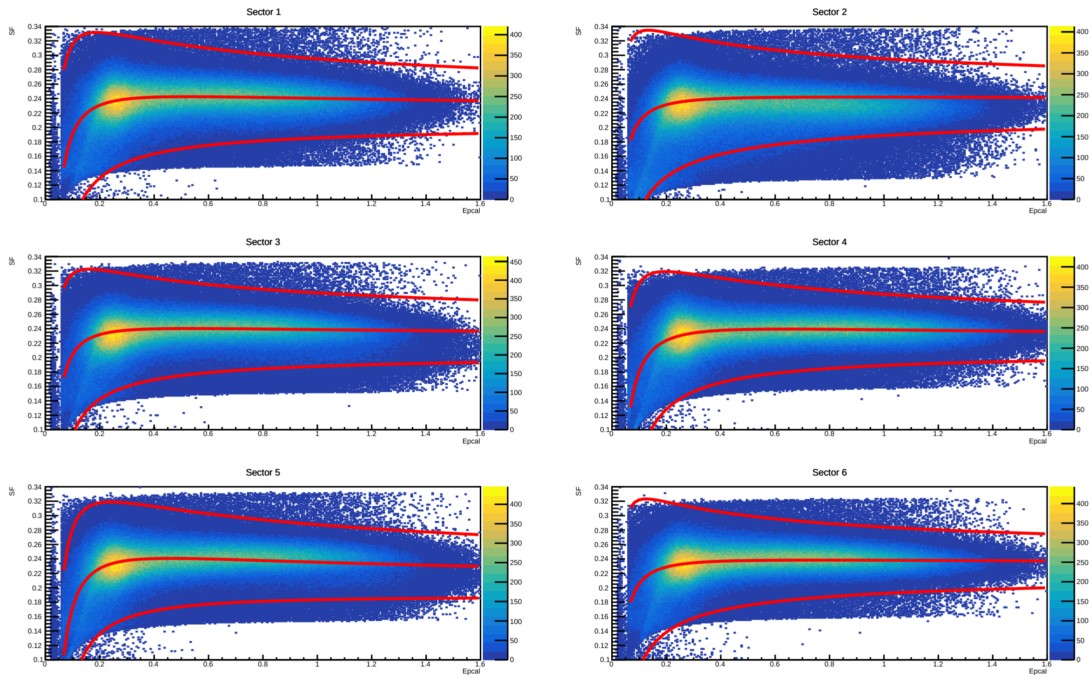

Figure 11: Sampling Fraction vs. Energy deposited in PCAL. Center red line denotes the mean of the distribution while outer red lines denote the 5σ where the cut is placed.

3.3 Detector response cuts

During data taking, there may be faulty detector components which can vary run-by-run. For example, during RGB data taking, some readout channels in the calorimeter system became problematic but fixed later. In this analysis, runs that had problematic detector responses were simply thrown away 6.2. Persistent problematic detector responses were solved by cutting these regions out in both data and simulation.

3.3.1 FTOF cuts

Looking at the occupancy in data of the FTOF bars, it was found that in Sector 2, FTOF Layer 1 has Bars 6 and 10 missing, and in Sector 5, FTOF Layer 2 has Bars 12 and 13 missing. See Fig. 15 for a plot demonstrating the latter issue. To ensure consistency in simulation, events with hits in any of these bars are manually removed. For the missing Layer 1 bars, only simulation hits are removed if the event

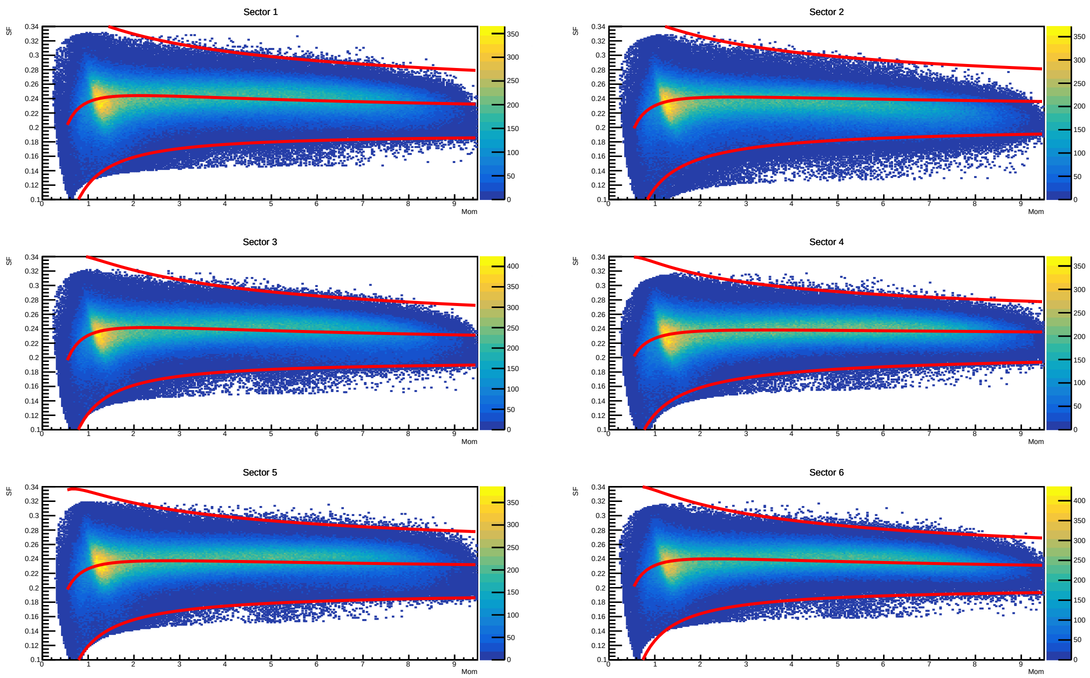

Figure 12: Sampling Fraction vs. momentum. The SF vs. PCAL energy cut has already been placed. Center red line denotes the mean of the distribution while outer red lines denote the 5σ where the cut is placed.

also has no Layer 2 hits. These strips were problematic during the entire run period, and permanently removed from simulation and data.

3.3.2 PCAL cuts

The occupancy in data of the PCAL U, V, and W strips was also investigated to find any problematic regions. It was found that in Sector 1, events that had hits in $W \in [72, 93]$ cm or $W \in [212, 231]$ cm needed to be removed. Similarly, for Sector 2 with hits in $V \in [30, 50]$ cm or $V \in [95, 120]$, Sector 4 with hits in $V \in [227, 245]$ cm, and Sector 6 with hits in $W \in [172, 192]$ cm. See Fig. 16 for a plot demonstrating the Sector 1 issue. These strips were problematic during the entire run period, and permanently removed from simulation and data.

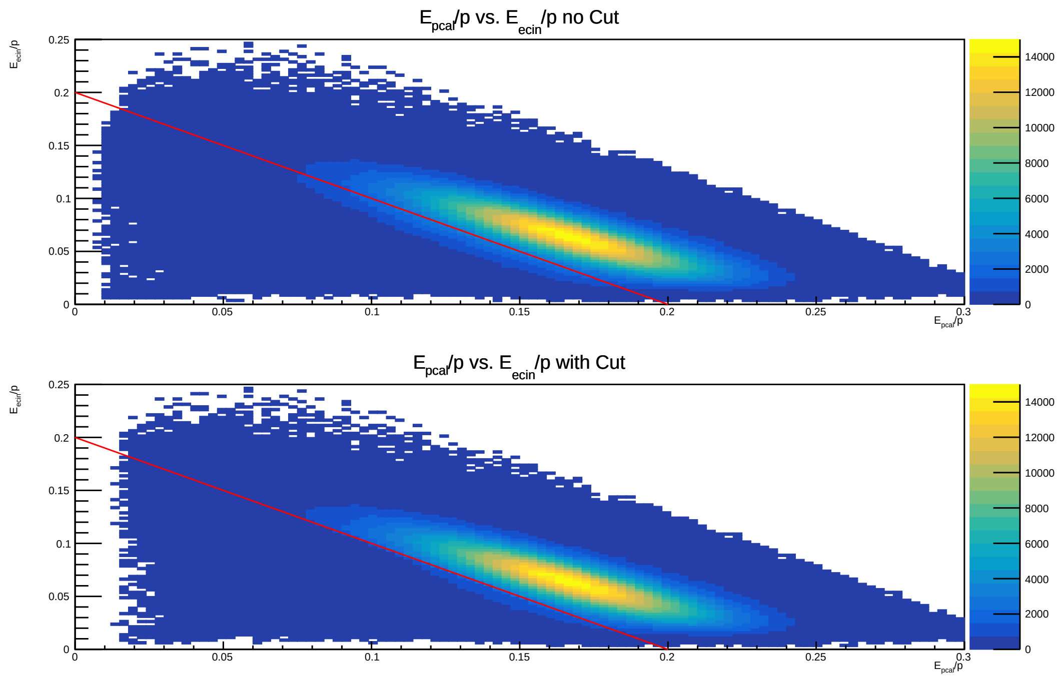

Figure 13: $\frac{E_{pcal}}{p}$ vs. $\frac{E_{ecin}}{p}$ before and after cut for $p > 4.5\,\text{GeV}$.

3.3.3 DC cuts

The response of the DCs can be monitored by looking at $p - \theta$ distributions in bins of ϕ for each region. Any problematic strips will appear as deficits independent of p. While there were areas of the DCs that seemed problematic, the PCAL response cuts, described above, fixed these deficiencies. There was no permanent DC response cut implemented over the run period.

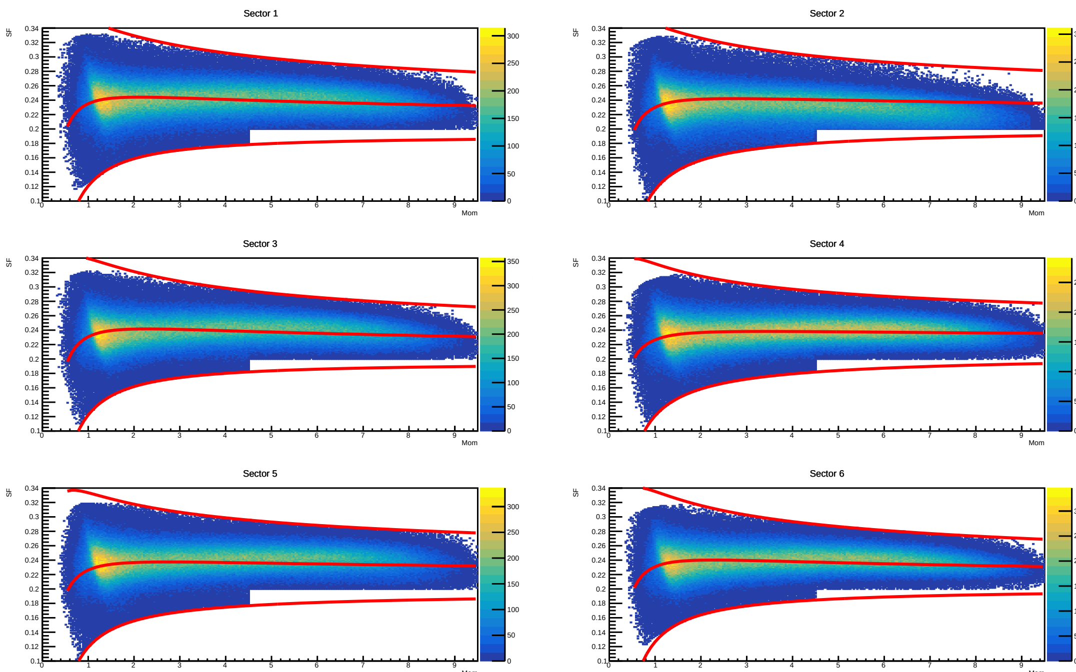

Figure 14: Sampling Fraction vs. momentum. The SF vs. PCAL energy cut and SF vs. momentum cut have already been placed. The additional high momentum-low SF cut has been placed.

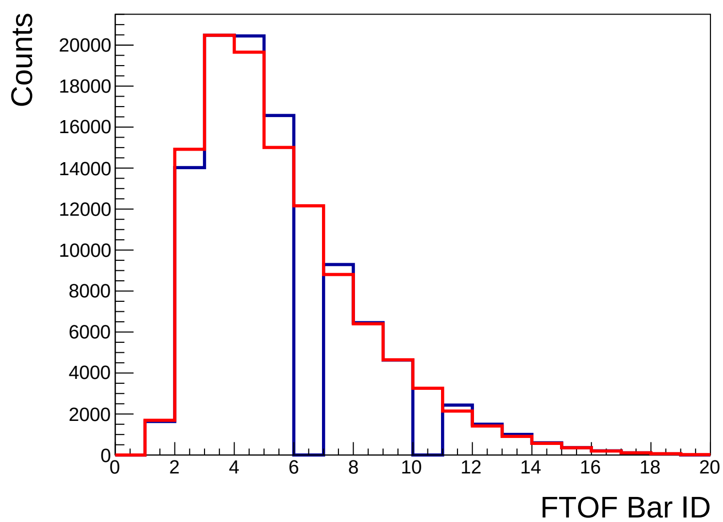

Figure 15: FTOF occupancy in Sector 2, Layer 1 from RGB data (blue), as compared to simulation (red). Simulation has been normalized to the data yield at Bar 3. Data shows missing Bars 6 and 10.

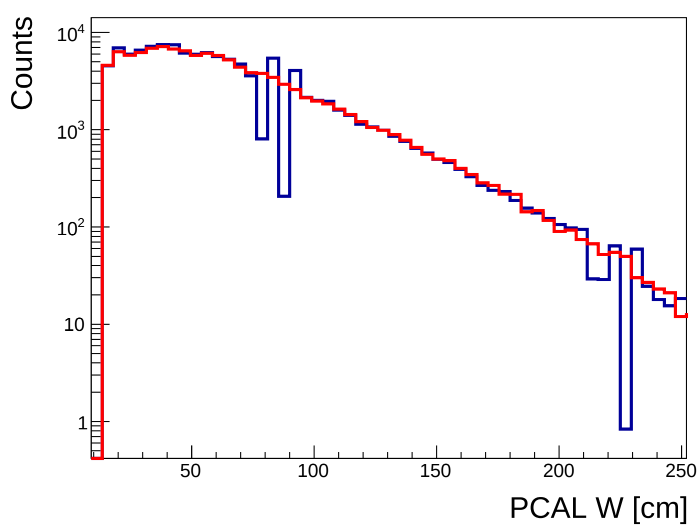

Figure 16: PCAL W occupancy in Sector 1 from RGB data (blue), as compared to simulation (red). Simulation has been normalized to the integral of the data. The two problematic regions are clearly visible.

3.4 Neutron Selection and Cuts

The selection of neutrons happens in two steps. First a good neutron candidate is selected from the list of BAND hits per event. All candidates are required to have energy deposition 2 MeVee in order to have reliable time-walk corrections. The time-of-flight window for candidate neutrons depends on the physics analysis of interest. This is done in the *bandsoft_tools* package (seeand [7]. Second a good neutron is selected from a list of candidates. The second step happens in the *bandsoft_ana* package or other analysis scripts which use skimmed root files as input. In the following, we describe the algorithm for finding a good neutron candidate.

Events with "good-neutrons" are selected using a blocking-algorithm. Events that survive this algorithm are called "good-neutron" events, and are used for analysis.

In a single event, multiple bars may register a signal-above-threshold. The challenge is to either accept or reject an event based on the topology of multiple hits in BAND. Charged particles are easy to reject with BAND as they leave tracks through the scintillator layers. Photons can be easily rejected via time-of-flight and energy deposition thresholds. Neutrons can leave "showers" or have a single interaction, where the former is favored with lower energy neutrons as they slow down and stop.

Our job is further complicated with upstream material between BAND and the target. Any neutron interactions in the material along the way will scatter and slow the neutron before reaching BAND. While the momentum distribution for neutrons in nuclei is dominated by low-momentum neutrons, these neutrons have a much higher interaction probability with the material upstream of BAND. Slower neutrons also have a higher probability to interact with the Pb wall of BAND, and in the veto layer (closest to the target). To prioritize purity over statistics, our algorithm selects events where either a shower has started in BAND, or a single interaction has occurred, minimizing the contribution of charge particles, photons, and low-momentum neutrons that have scattered on the way to BAND.

To select this topology in BAND, our blocking-algorithm loops through all hits in BAND, and asks if the hit is "blocked" by another hit, see Fig. 17. What we are left with are the lead-hits of a shower, or a single interaction. The exception of this is when two hits are close enough in space and time such that the single-neutron-interaction energy was shared among two adjacent bars – these events are clustered together and taken as "good". Any ambiguous events where we have multiple showers or multiple single-hits are thrown away.

The blocking criteria uses spacial and time information to determine whether a hit has been blocked or not. For example, hits that are adjacent but separated by

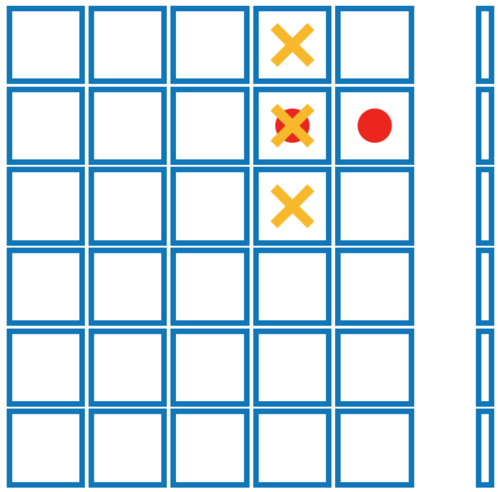

Figure 17: Cartoon schematic of the goal of blocking-algorithm. The thin rectangles represent the veto layer of BAND and the 6x5 array of squares represents 30 of the BAND scintillators. The target is 3-m to the right. The two red dots represent two hits (red) in adjacent layers in BAND. The yellow "X"s represent the BAND scintillators "blocked" by the hit closest to the target. In the blocking algorithm, the hit closest the target blocks the hit behind it, and the unblocked hit is used in the analysis.

more than $\sim$ 10ns are not related to one another and will be taken as two separate hits. The blocking-algorithm works as follows - for each hit, ask if there is another hit that is

1. In front of it ($\text{layer}_{\text{other}} = \text{layer}_{\text{me}} + 1$),
2. In adjacent y ($y_{\text{other}} = y_{\text{me}} \pm 8\text{cm}$),
3. In similar x ($x_{\text{other}} = x_{\text{me}} \pm 15\text{cm}$ - expect for veto bars as "other", no $x-$requirement is made),
4. In similar ToF ($\text{ToF}_{\text{other}} = \text{ToF}_{\text{me}} \pm 3\text{ns}$ - except for veto bars, the window is $\pm 15\text{ns}$),

and if all these conditions are true, then the hit is blocked by the other hit. We then ask how many surviving hits are left in the event. Hits in veto bars can block hits in bars behind them but are not considered as neutron candidates. If there are more than 2 unblocked hits, the event is thrown away. For two unblocked hits, we further ask if we can cluster these together (i.e. they came from the same neutron interaction and the energy deposition was shared among the two bars). For these to be clustered into one hit, we ask for the same conditions as above, but removing the layer-requirement. If all of those conditions are true, then we cluster the two hits together, and take the hit with the earliest ToF to be used in the analysis.

With this algorithm, we throw away $\sim 5\%$ of events due to ambiguity. See Fig. 18 for a time-of-flight response in BAND with this algorithm implemented - a sharp photon peak, neutron shoulder, and random neutron background is clearly visible. The subtraction of the random background is shown in Sec. 4. For the physics analysis, neutron events will be selected based on a TOF and energy deposition cut on the "good-neutrons" found by the neutron algorithm.

We added neutron fiducial cuts on band to remove events within $\approx$ 10 cm of the bar ends due to light reflection from the light pipes. We added angular cuts $\theta_n < 168.5^\circ$ to remove neutrons traveling at very shallow angles thru the beam pipe material. We also removed the top row of scintillators due to unexplained hot spots near the edges, due to beam-correlated room background.

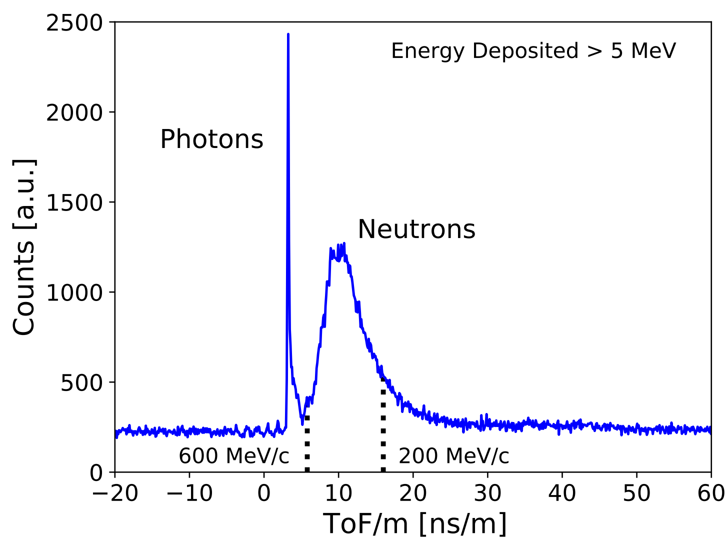

Figure 18: Time-of-flight per meter spectrum of "good-neutron" events in BAND.

To select a reasonable value for the required energy deposition, we examined the impact of different E_{dep} cuts on our signal and background. The resulting ratio of signal to background, and total statistical uncertainty, are shown in Figure 19. The values for signal and background include all kinematic cuts used in our tagged

405 analysis (Table 3, with the additional requirement of $p_T < 0.1$ GeV/c).

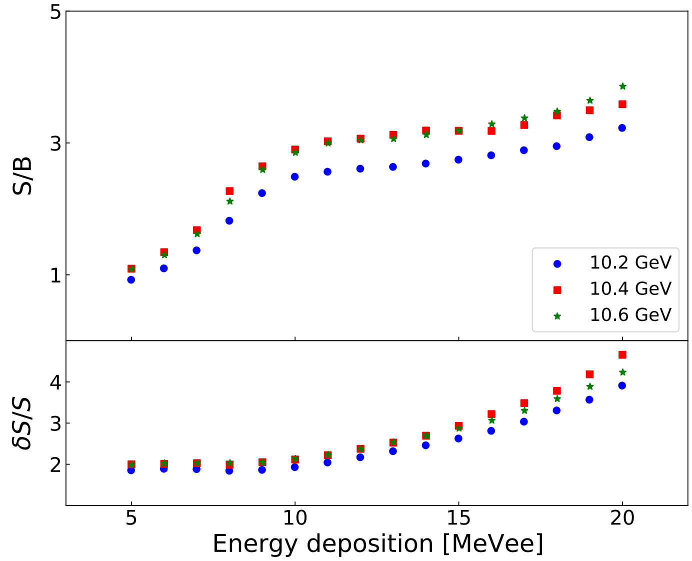

Figure 19: S/B ratio and relative statistical uncertainty $\delta S/S$ as a function of minimum required E_{dep} for the three different run periods. The 10.2 GeV run was at a higher beam current and therefore a lower signal to background ratio.

406 Based on this study, we chose to require an minimum energy deposition of
407 $E_{dep} = 10$ MeVee. This requirement is large enough to have reached the approximate
408 plateau in S/B, without significantly increasing the statistical uncertainty.

4 Random Neutron Background Subtraction

In additional to signal neutrons, BAND also detects a constant rate of background neutrons. Event mixing was used to generate a high-statistics sample of background neutrons to perform background subtraction.

Background neutrons for event mixing were chosen from early off-time events (TOF between -56 ns and -4 ns). For every neutron in this region, the TOF was increased by 4 ns increments until it was in the signal region (TOF between 12 ns and 100 ns). This was done to properly subtract structure in the background distribution arising from the 4 ns beam bunches of the electron beam. The neutron was then paired with a random inclusive electron, allowing the calculation of all tagged DIS kinematic variables. To enhance statistics, the same off-time neutron was used repeatedly for each 4 ns bunch in the signal region.

The event-mixed background was normalized to the number of background events in the off-TOF region used to generate the sample. All kinematic cuts applied to data are also applied to the background sample. For any quantity of interest, a histogram is made for both data and background and subtraction yields the background-subtracted distribution.

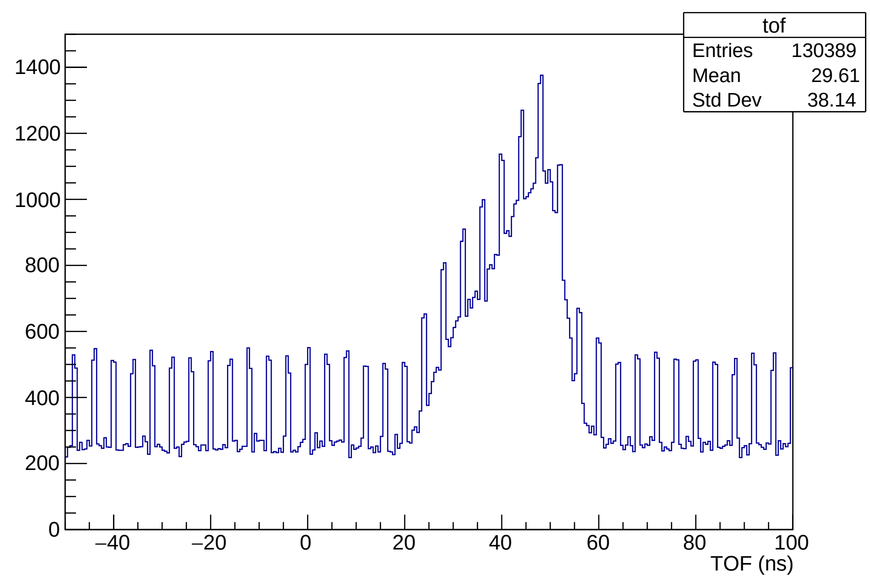

Figure 20: Simulated signal and background TOF distribution

A GEMC simulation was used to validate this procedure. Separate simulations of signal and background events were combined into a single simulated data file. In order to assess the procedure's ability to account for time structure in the background, an exaggerated time structure was included in the background. This is shown in Figure 20, where the simulated signal peak (TOF between 20 ns and 60 ns) sits on a constant background with periodic pulses. The event mixing procedure was then run on the simulation, and the event-mixed background distribution was compared to the true background distribution. Figure 21 shows this comparison for the TOF distribution with all kinematic cuts used in the BAND analysis. Figure 22 shows the same comparison for x' distributions in bins of α_S. As can be seen, the event mixing procedure is able to excellently reproduce the true background distribution in the signal region, including the periodic background pulses visible in the TOF spectrum.

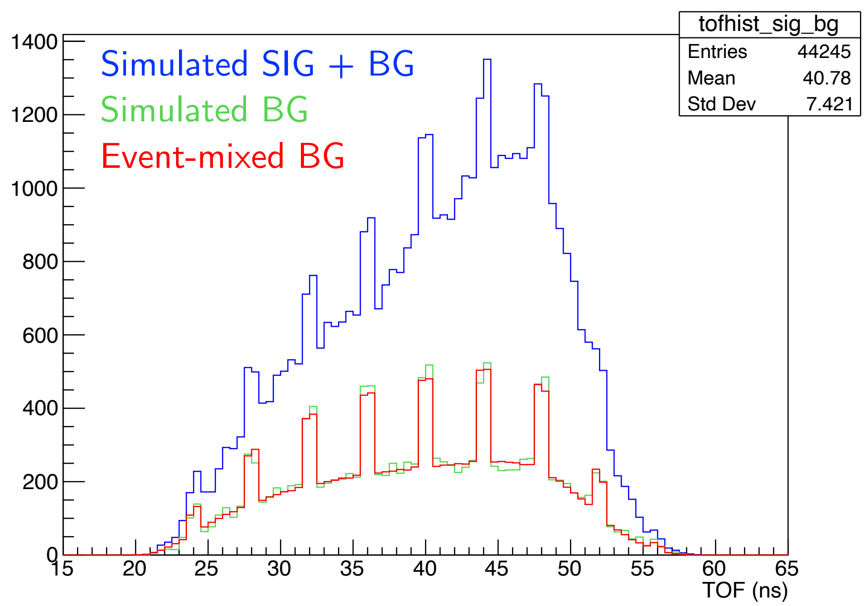

Figure 21: Simulated TOF distribution for Signal and Background (blue), Background (green) and event-mixed background (red).

A final validation was to directly compare distributions of off-time background events to the mixed background events. Clearly such comparisons can not be made for variables sensitive to neutron TOF, but they can be made for geometric quantities such as θ_n and θ_{nq}, shown in Figure 23. Both the shape and normalization of the distributions are in excellent agreement.

The background subtraction procedure was presented in the RGB meeting on January 9, 2021 (here)

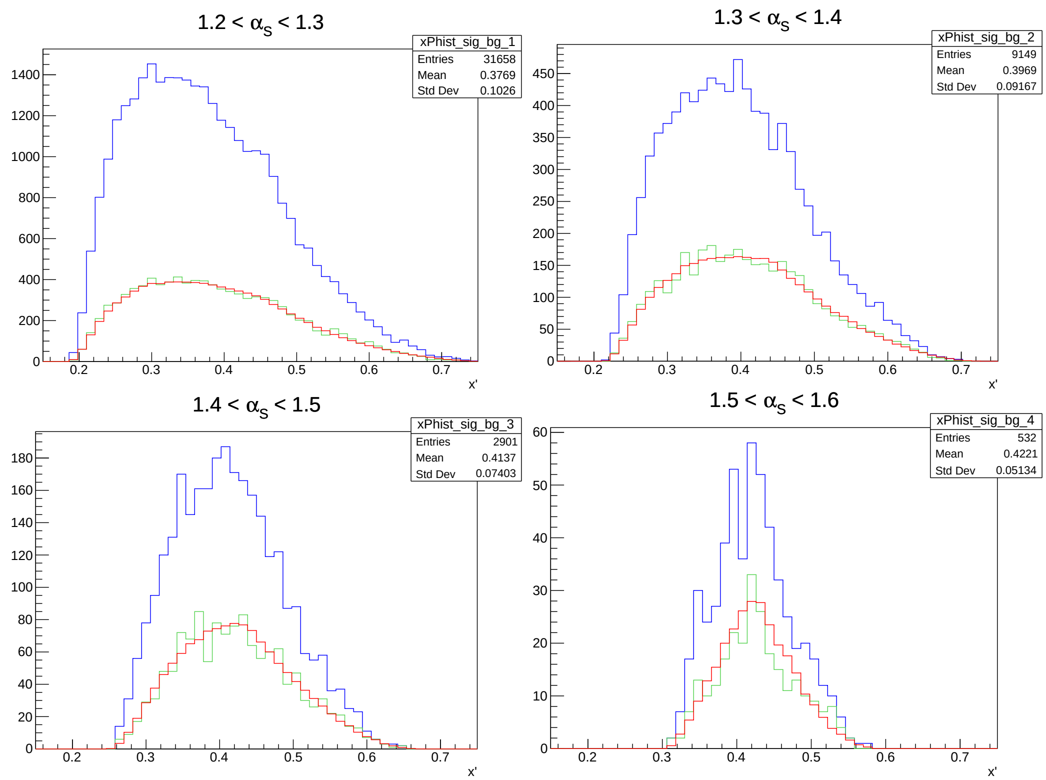

Figure 22: Simulated x' distributions in bins of α_S for signal and background (blue), background (green) and event-mixed background (red).

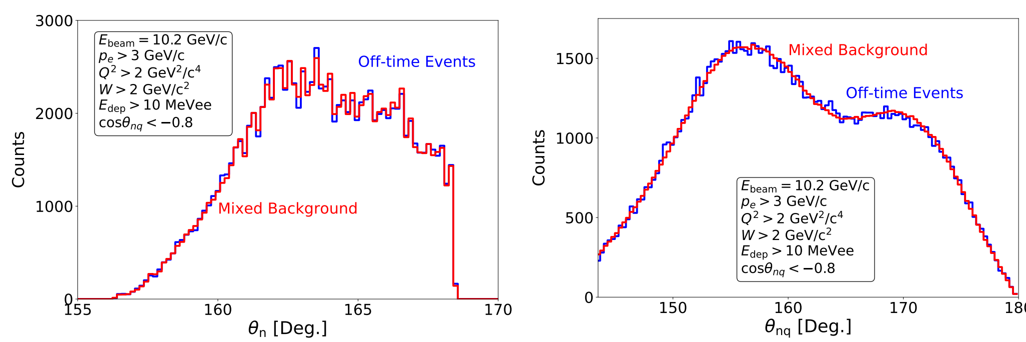

Figure 23: Direct comparison of θ_n (left) and θ_{nq} (right) for off-time background events (blue) and mixed background events (red).

5 Assessing Impact of Target Wall

In our analysis, we also need to assess the contributions of the target wall endcaps to data. This was also presented in the RGB meetings on February 12 and 19, 2021 (see (here) and (here).

In order to asses the impact of the target wall contribution in production data, the empty target runs (6599, 6601 and 6603) are used for 10.2 GeV beam energy setting. The ratio of total accumulated charge from production runs to empty runs is used as normalization factor. We apply similar cuts as for the tagged analysis:

Electron selection cuts:

- Eventbuilder PID = -11
- DC and ECAL fiducials (see Section 3)
- ECAL PID cuts (see Section 3.2)
- $Q^2 > 2$ GeV^2
- $W^2 > 4$ GeV^2
- $3\,\text{GeV} < p_e < E_{beam}$
- $-5 < V_z < 2$ cm

Neutron selection cuts:

- Neutron good candidate as described in 3.4
- $-1 < cos\theta_{nq} < -0.8$
- $E_{dep} > 10$ MeV

First we compare the time-of-flight spectrum and the z-vertex distribution of the empty target runs with one single 10.2 GeV run (6420) (see Fig. 24)

In the next step, we apply also the momentum cuts on the neutron as in the tagged analysis (see Sec 8). The resulting time-of-flight spectrum and z-vertex distribution are shown in Fig. 25. We obtain that the target wall contribution is around 2% for the 10.2 GeV data and, therefore, we do not subtract explicitly for target wall contributions in the tagged analysis.

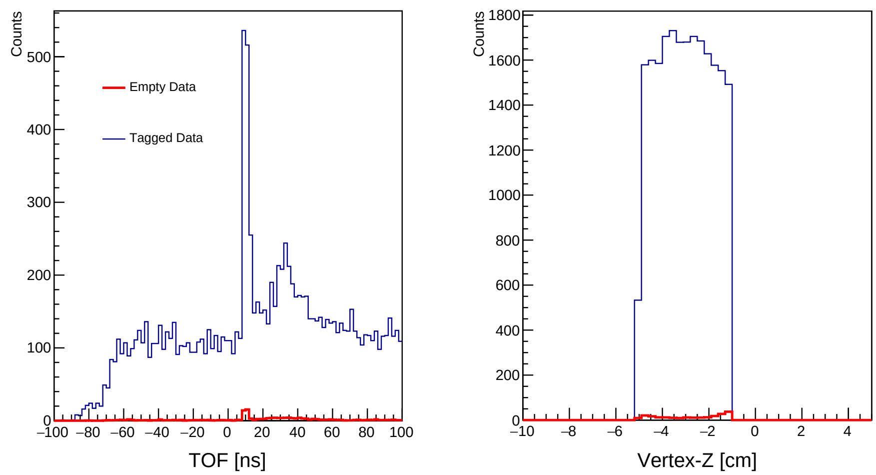

Figure 24: Distributions of the 10.2 GeV production data (a single run 6420) and target wall data. (Left) TOF distribution for BAND. (Right) z-vertex distribution.

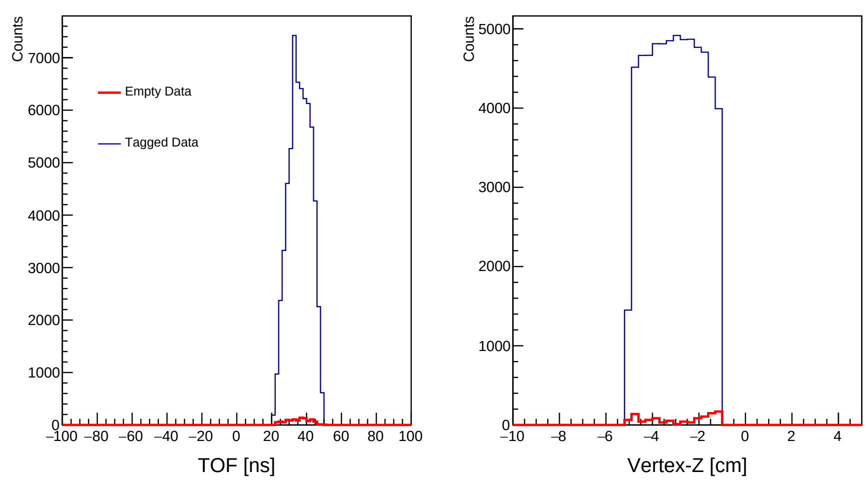

Figure 25: Distributions of the 10.2 GeV production data (all good runs) and target wall data with all tagged analysis cuts. (Left) TOF distribution for BAND. (Right) z-vertex distribution.

In addition to the quantitative analysis, we have made some comparisons in the TOF spectrum between full and empty target runs with different cuts. One motivation for these comparisons is to investigate the source of an anomalous peak in the TOF spectrum around 34 ns (listed as a known open issue in Section A).

For the purpose of these comparisons, events are required to have both an electron satisfying the PID and fiducial cuts detailed in Section 3, as well as a good neutron candidate satisfying the veto algorithm detailed in Section 3.4. A cut on event vertex of $v_z < 2$ cm was applied to ensure events originated in the vicinity of the target, but the tight vertex cut used in the main analysis was not applied. No further kinematic cuts were applied to the events.

Both the charge- and luminosity-normalized comparisons for three different E_dep cuts are shown in Figure 26. One sees from the charge-normalized comparisons that the empty target rates are orders of magnitude smaller (at least 10^{-3}) than the full target rates. While raising the E_{dep} cut suppresses the anomalous 34 ns peak (see also A) for both the full and empty target, the suppression appears stronger for the empty target.

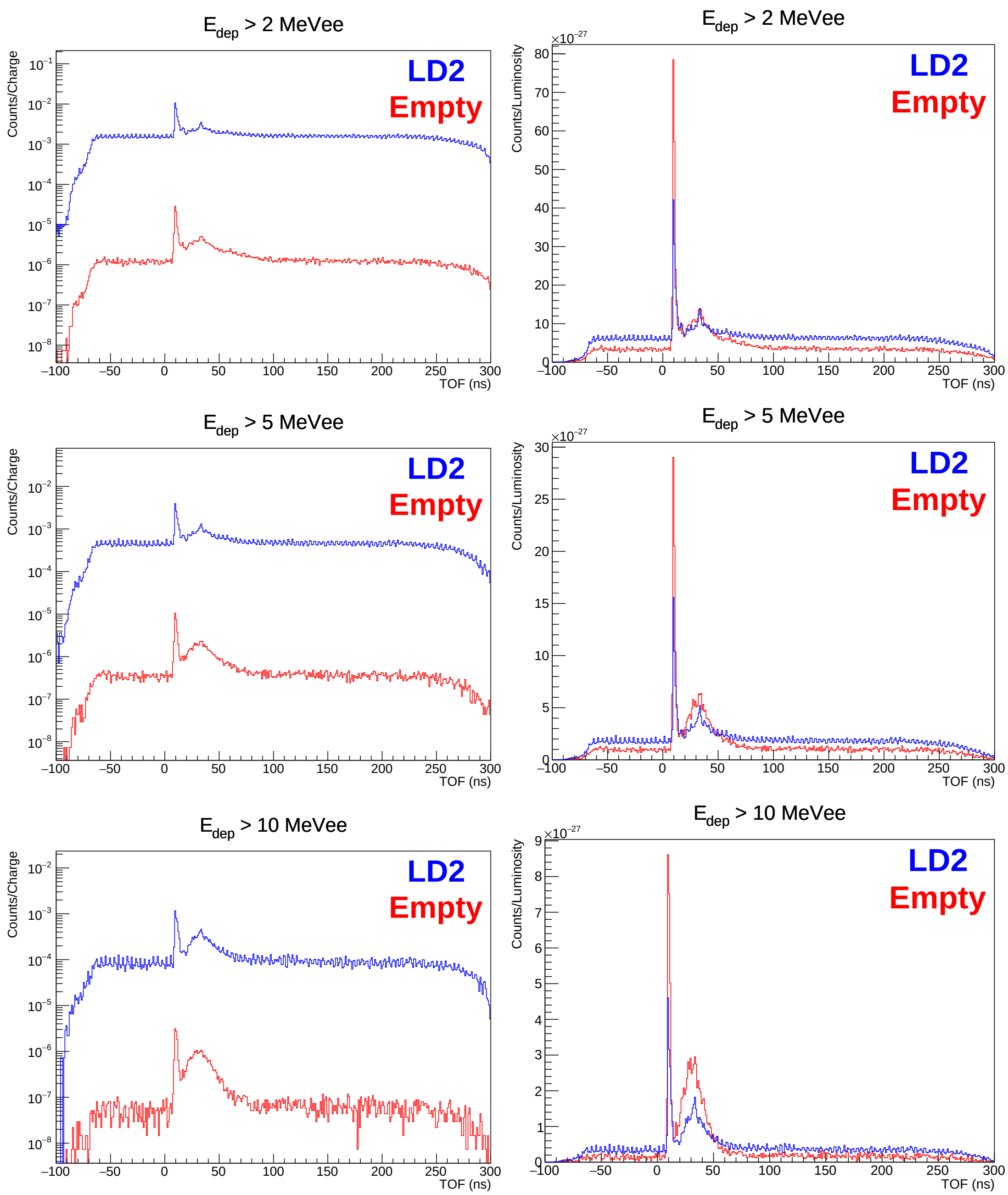

Figure 26: Comparison of the TOF spectrum for the full LD2 target (blue) and empty target (red). The left column shows counts normalized by charge, while the right column shows counts normalized by luminosity. From top to bottom, the three rows have a minimum E_{dep} cut of 2, 5, and 10 MeVee.

6 Good Run Selection

For this analysis, we have developed our own good run list, which is a refinement of the Quality Assurance (QA) analysis of RGB data performed by the CLAS collaboration and RGB collaborators. The QA procedures and Database (QADB) was developed by the CLAS collaboration and implemented in both RGA and RGB. The QA procedure uses trigger electron yield, normalized by the Faraday Cup (FC) charge, in order to identify outlier data. The QADB is the resulting data structure that can be used when reading in data files in order to filter out problematic runs and events. QA and QADB documentation and code can be found at Ref. [9]. The result of the QA analysis for each run period of RGB can be found at Refs. [1, 2, 3]. These results create a "good run" (and event) list for each run period, found at Refs. [4, 5, 6].

This list was further refined by excluding additional runs based on the quality of the data recorded by BAND. Neutron yields in BAND, normalized by the FC charge, are used to improve the good run list that RGB developed, discussed in the next chapter. Data-to-simulation comparisons also further refined the good run list, based on problematic runs that were not captured in the QA analysis, discussed later in this chapter.

6.1 BAND Good Run Selection

Based on the good runlist for RGB runs, we also checked the quality of these runs for BAND events. The quality criteria were the photon, background and signal rate per charge for each run. Since the rate on BAND is limited, we can not do this analysis for a group of events per run. We can only disregard full runs or not. In the following, we describe the selection criteria for the different rates, the analysis procedure to determine bad runs and the obtained outliers.

6.1.1 Event Selection

We measured three types of events in BAND: neutron signal (signal), off-time background (background), and photon events. The time-of-flight (ToF) window for the events were as follows: signal events were between 18 to 48 ns, background events were between -10 to 5 ns, and the photon events were between 8 to 13 ns. The background and photon events had an energy cut of 2 MeV while the signal had a stricter 5 MeV cut.

6.1.2 Analysis Procedure

We used a ROOT script called "counts_charge.cpp" to analyze a set of skimmed files for BAND neutrons. The script read in data from a skimmed file, applied the cuts mentioned in the previous section, and wrote the new obtained counts for each cut to a file. If told to, it differentiates events based on which layer of BAND it hit. A python plotting script creates plots of counts per charge as a function of run number for the signal, background, and photon events. It did this for all hits in BAND, or in each layer. The program also calculate the weighted mean and standard deviation of the counts per run. It used these to plot the mean and standard deviation lines. The standard deviation lines were 2σ and 3σ for all hits in BAND or 3.5σ and 4σ for hits in each layer. We removed runs that were outside 3σ for all hits in BAND and outside 4σ for each layer. The higher σ for each layer in BAND is because the lower statistics which causes extra fluctuations in the data.

There were four types of run periods we analyzed. In order of analysis, they were the 10.2 GeV run, 10.6 GeV run, Low-Energy Run (LER), and 10.4 GeV run periods. Because of many changes in its run conditions, we divided the 10.6 GeV run period into four epochs for our analysis (these are similar to the epochs in the QA timelines and are due to trigger changes). We similarly divided the 10.4 GeV run period into two epochs. The 10.2 GeV run conditions were consistent enough to analyze all at once. For the LER analysis, we found that sector 4 data acquisition problems resulted in inconsistent counts per charge strength. We removed sector 4 from the LER skims, and found the results much more consistent. We only considered production runs; consequently, we removed low luminosity, empty target, and other non-production runs. In addition to these non-production runs, we occasionally removed runs that had spurious values. We performed two passes on the 10.2 GeV, 10.4 GeV and 10.6 GeV runs; the second pass removed bad runs found in the first pass in addition to the non-production and spurious runs. Counts per charge plots for all runs are shown in the Appendix C.

6.1.3 Analysis Results

We found many runs to remove from the original RGB good runs list (see RGB wiki). For the 10.2 GeV period, we had one such run, 6515, which had values of infinity. In addition to that run, we found four other bad runs: 6459, 6460, 6471, and 6551. As mentioned in 6.1.2, we divided our 10.6 GeV analysis into four epochs. Epoch 1 had a spurious run, 6199, which had negative values. No other bad runs were found in epoch 1. Epoch 2 had two bad runs: 6209 and 6242. Epoch 3 had five bad runs in

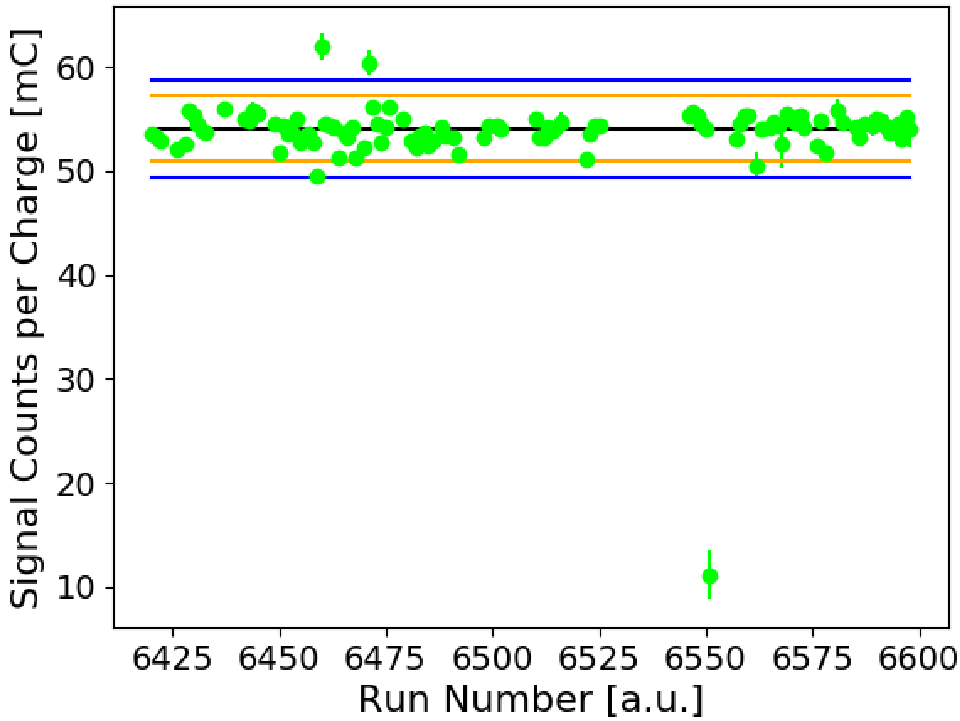

Figure 27: The counts per charge as a function of run number for the 10.2 GeV period. The black line is the mean while the orange and blue lines show the 2σ and 3σ lines respectively.

the first pass (6252, 6254, 6285, 6287, and 6288) and four in the second (6248, 6250, 6251, and 6266). Epoch 4 have five (6303, 6352, 6356, 6357, and 6359) which brings the total of bad runs for the 10.6 GeV run period to sixteen. The LER analysis revealed five bad runs: 11287, 11292, 11293, 11295, and 11300. For the 10.4 GeV period, we analysized only production and low luminosity runs. We also removed all runs before 11360. Excluding these, the bad runs for epoch 1 were 11361 and 11372 in the first pass and 11394 in the second. For epoch 2, we removed nine runs (11421, 11445, 11485, 11486, 11487, 11508, 11537, 11538, and 11548) in the first pass and only 11553 in the second. We removed all thirty-nine (twenty-six) of these runs from the good run list plus the 10.4 GeV runs before 11360. At the end we created different runlists for the good, bad and special runs. These can be found in runlist folder at the *bandsoft_tools* software (`https://github.com/hauenst/bandsoft_tools`).

6.2 Other problematic runs

To identify outlier runs that may remain, even after the RGB QA procedure, comparisons to simulation were performed. The data and simulation were both luminosity normalized, and then a ratio between data and simulation taken for many detector variables, in fine bins of p, θ, ϕ. A test-statistic was constructed for each ratio, and the variation of this test-statistic over the run period was observed.

A few runs appeared to have transient problems with some detector systems, and as such removed from the data set. Below the problematic runs are indicated with why they were removed:

- 006420 – DC Sector 6 has missing strips
- 006443 – PCAL and FTOF Sector 2 has lower yield
- 006558 – PCAL and FTOF Sector 3 has lower yield
- 006568 – Small statistics, run was only ~ 10 min long
- 006573 – PCAL and FTOF Sector 3 has lower yield
- 006592 – PCAL and FTOF Sector 2 has lower yield
- 006598 – Small statistics, run was only ~ 10 min long

The removal of these runs from the good run list after the BAND rate selection was applied constitutes the final run list for this analysis.

7 Inclusive Analysis

In the first step of the analysis, we compared inclusive electron events with GEMC simulations based on a deuteron structure function event generator. The event generator also includes radiation.

7.1 Cuts and Coverage

We select our electron events with the following cuts

- Eventbuilder PID = -11
- DC and ECAL fiducials
- ECAL PID cuts (see Section 3.2)
- $Q^2 > 2$ GeV^2
- $W^2 > 4$ GeV^2
- $3\,\mathrm{GeV} < p_e < E_{beam}$

Also, a tight vertex cut is implemented to identify electrons originating from within the target. For this analysis, an electron vertex between $-5\,\mathrm{cm} < vtz_e < -1$ cm. This allows for a large reduction of contamination originating from the target cell walls, see later discussion, as well as removing any contamination from the beamline, see Fig. 28.

The final kinematic coverage in Q^2, W, x_B for the DIS electrons is shown in Fig. 29.

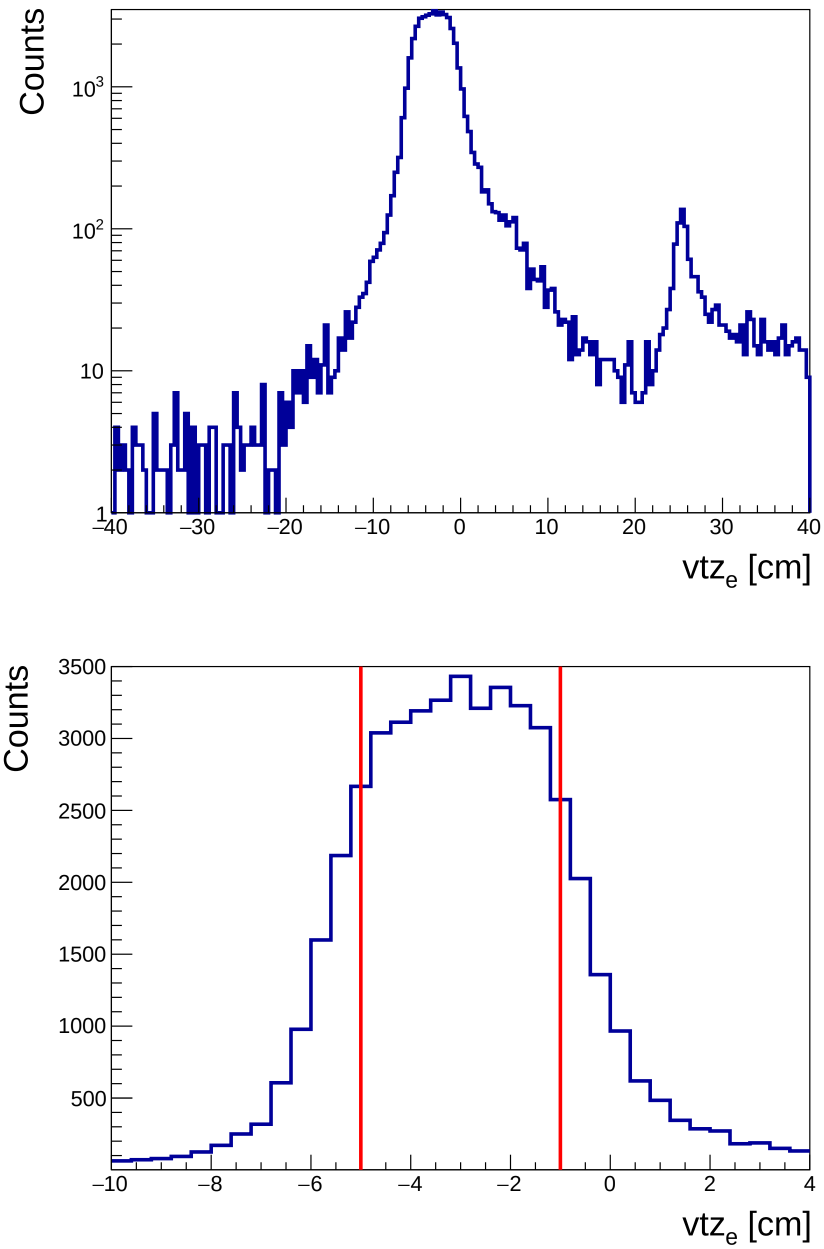

Figure 28: (Top): Electron vertex distribution for EB electrons from RGB (only a partial run). (Bottom): Zoomed in electron vertex distribution with lines indicating the vertex cut implemented for electron identification refinement.

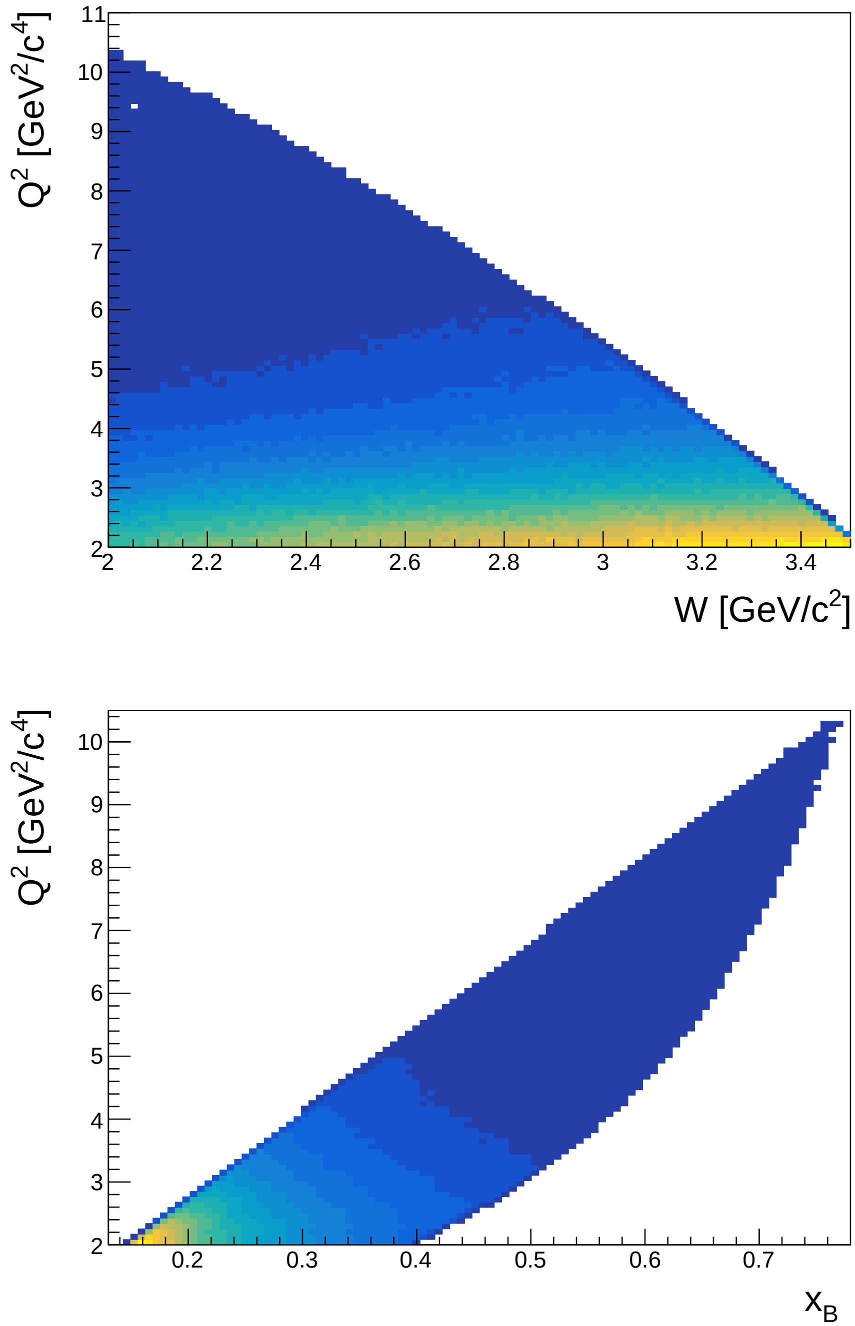

Figure 29: (Top): W vs Q^2 phase space of $d(e,e')X$ RGB data (a single run) with event selection cuts. (Bottom): Same but for x_B vs Q^2 phase space.

7.2 Data to MC comparisons

We simulated 25M inclusive events for each beam energy and compare them separately to data. As described in section 2, we apply radiative corrections in the simulation, add extra smearing to the electron kinematics to match data and MC resolutions, and include background merging independently for each beam energy.

For our comparison plots, we scale the simulation results via the histogram integral to data. Luminosity-normalized comparisons are not required as the observable of this analysis is a double ratio to remove luminosity uncertainties. Figs. **??** shows the comparisons for various electron kinematic variables for the data at 10.2 GeV. We observe a very good agreement between data and MC with a maximum deviation of 10% at the edges of phase space. In most cases, the agreement is better than 5%. This indicates that the electron side for our tagged data and MC comparison is well under control. We want note that the largest deviation between data and MC are observed in the electron ϕ distributions as it is observed also in other RGA analyses. However, we think this does not affect the current result strongly, since our physics channel is symmetric in ϕ and the kinematic distributions match very well.

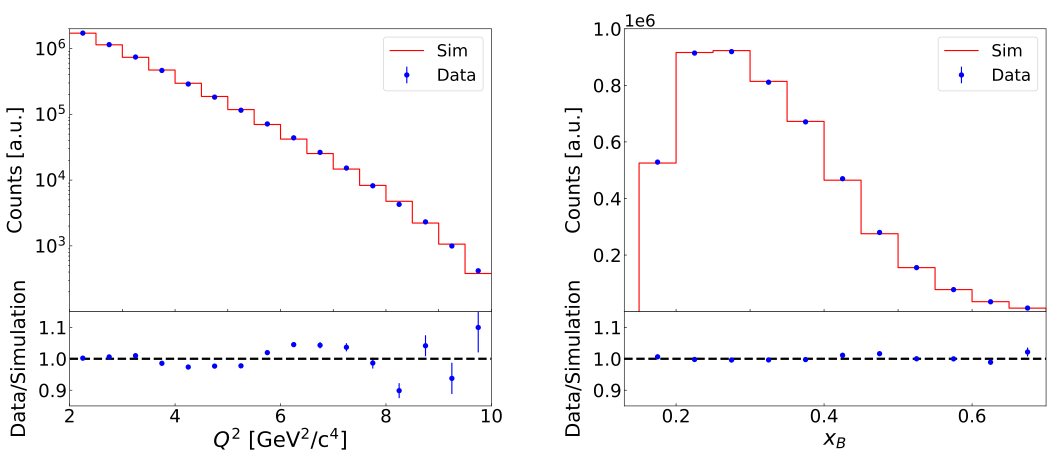

Figure 30: (Left): Q^2 (Right): x_B. Distributions of data (blue) and simulation (red).

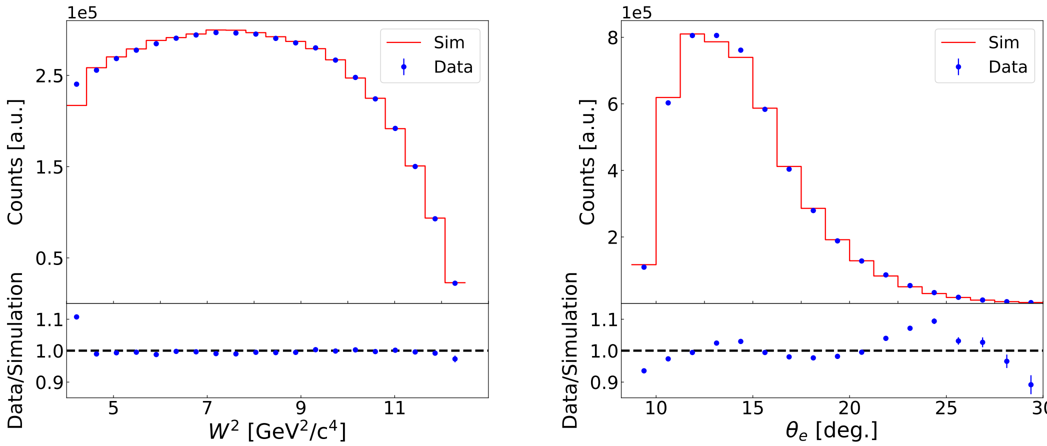

Figure 31: (Left): W^2 (Right): θ_e. Distributions of data (blue) and simulation (red).

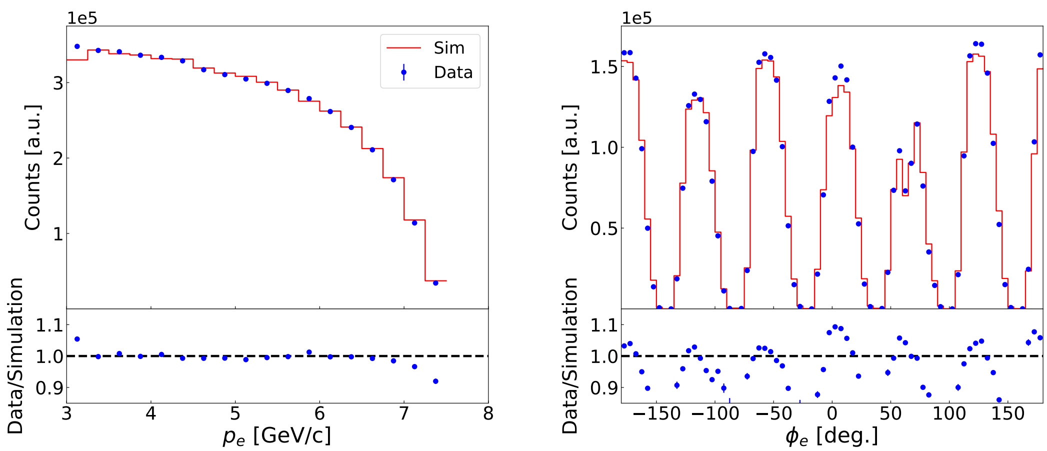

Figure 32: (Left): p_e (Right): ϕ_e. Distributions of data (blue) and simulation (red).

8 Tagged Analysis

The experimental and simulated tagged yields were extracted using the same software package. The selection of electrons in CLAS12 corresponds to the inclusive analysis selection (Section 7) with details given in Section 3). The selection of neutrons in BAND is described in Section 3.4. Table 3 list all selection cuts for the tagged analysis

Electron	Inclusive Cuts
Neutron	BAND fiducials
Neutron	0.25 GeV/c $< p_n <$ 0.6 GeV/c
Neutron	$E_{dep} >$ 10 MeVee
Tag	$W' >$ 1.8 GeV
Tag	$\alpha_S > 1.2$
Tag	-1 $< \cos\theta_{nq} <$ -0.8

Table 3: Kinematic cuts in tagged analysis.

8.1 Data - MC Comparisons

The first step of the tagged analysis is to compare data and simulation yields. The simulation has been scaled to the integrated number of data counts. The simulation is based on the tagged generator described in Sec. 2.1 with 100M events for each beam energy.

Comparisons of some key tagged kinematic variables (namely, α_S, p_T, x', and W') are shown in Figure 33. For the complete set of data/MC comparisons, see Appendix B.

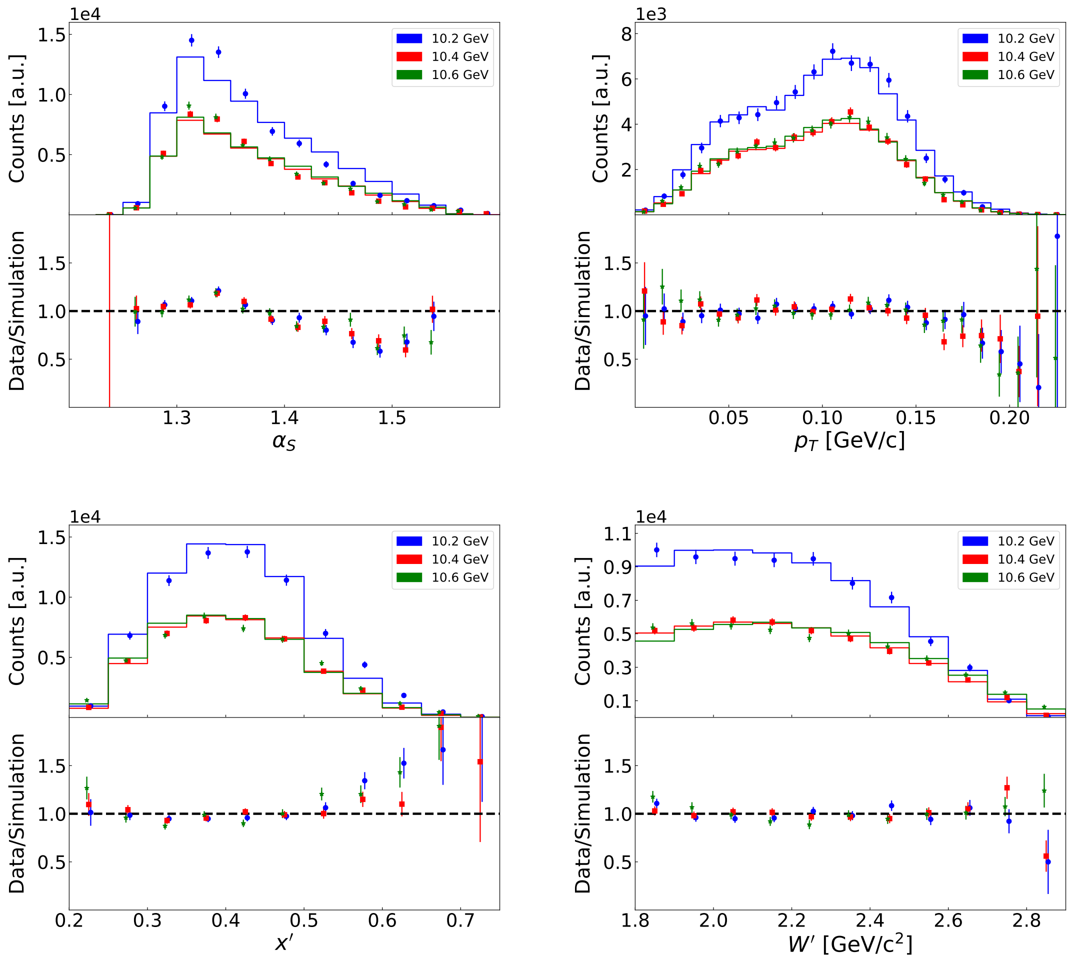

Figure 33: Comparison of data (points) to simulation (histograms) for various tagged kinematic variables at each beam energy.

8.2 Tagged double ratio results

Here we show results for the tagged double ratio discussed in Section 1.2. Specifically, we determine the following ratio:

$$\begin{aligned} &\frac{d\sigma_{\text{dat}}(x', \alpha_S, p_T, Q^2)}{d\sigma_{\text{dat}}(x'_{\text{ref}}, \alpha_S, p_T, Q^2_{\text{ref}})} \Bigg/ \frac{d\sigma_{\text{sim}}(x', \alpha_S, p_T, Q^2)}{d\sigma_{\text{sim}}(x'_{\text{ref}}, \alpha_S, p_T, Q^2_{\text{ref}})} = \\ &\frac{N_{\text{dat}}(x', \alpha_S, p_T, Q^2)}{N_{\text{dat}}(x'_{\text{ref}}, \alpha_S, p_T, Q^2_{\text{ref}})} \Bigg/ \frac{N_{\text{sim}}(x', \alpha_S, p_T, Q^2)}{N_{\text{sim}}(x'_{\text{ref}}, \alpha_S, p_T, Q^2_{\text{ref}})} \equiv \mathcal{R}, \end{aligned} \tag{19}$$

where we choose $x'_{\text{ref}} = 0.3$, Q^2_{ref} emphasizes that the acceptance in Q^2 changes for different x', $d\sigma$ is the sixfold differential cross section, and N is the number of un-normalized counts observed. The equality from the differential cross section ratio to an un-normalized count ratio is dependent on how well the simulation can accurately model and describe bin-migration effects, acceptance effects, radiative effects, etc.. As this observable is a double ratio, normalizing both simulation and data to a relative kinematic point, luminosity exactly cancels and detection effects are largely reduced.

Figs. 34 and 35 show the available phase space in $x' - Q^2$ when looking in bins of α_S, p_T. The double ratio, $\mathcal{R}$ (Eqn. 19), is shown as a function of x' for bins of α_S and p_T, integrating over the full Q^2 coverage in Figs. 36 and 37. The statistics for each beam energy setting have been combined. The uncertainty shown is only point-to-point, where data, background, and simulation statistics have been incorporated:

$$\begin{aligned} \mathcal{R} &\equiv f_1 \Big/ f_2 = \frac{D}{D_{\text{ref}}} \Bigg/ \frac{M}{M_{\text{ref}}} \\ \delta\mathcal{R}^2 &= \left(\frac{1}{f_2}\delta f_1\right)^2 + \left(\frac{f_1}{f_2^2}\delta f_2\right)^2 \\ \delta f_1^2 &= \left(\frac{1}{D_{\text{ref}}}\delta D\right)^2 + \left(\frac{D}{D^2_{\text{ref}}}\delta D_{\text{ref}}\right)^2 \\ \delta f_2^2 &= \left(\frac{1}{M_{\text{ref}}}\delta M\right)^2 + \left(\frac{M}{M^2_{\text{ref}}}\delta M_{\text{ref}}\right)^2 \equiv \mathcal{R}, \end{aligned} \tag{20}$$

with $D = N_{\text{dat}}(x', \alpha_S, p_T, Q^2)$ and $D_{\text{ref}} = N_{\text{dat}}(x'_{\text{ref}}, \alpha_S, p_T, Q^2_{\text{ref}})$ and similarly M refers the the simulation counts. Moreover, D are the counts **after** background subtraction, $D = Y - B$, where Y is the raw yield (signal and background) and B are the

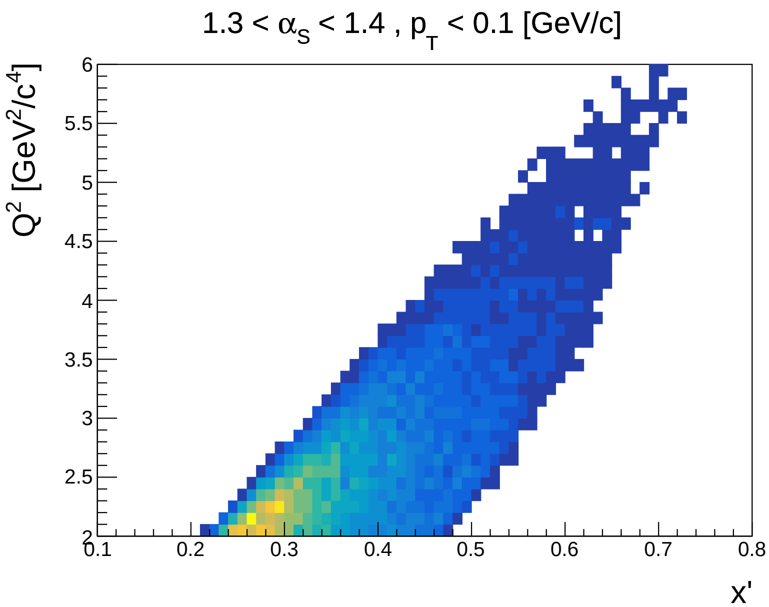

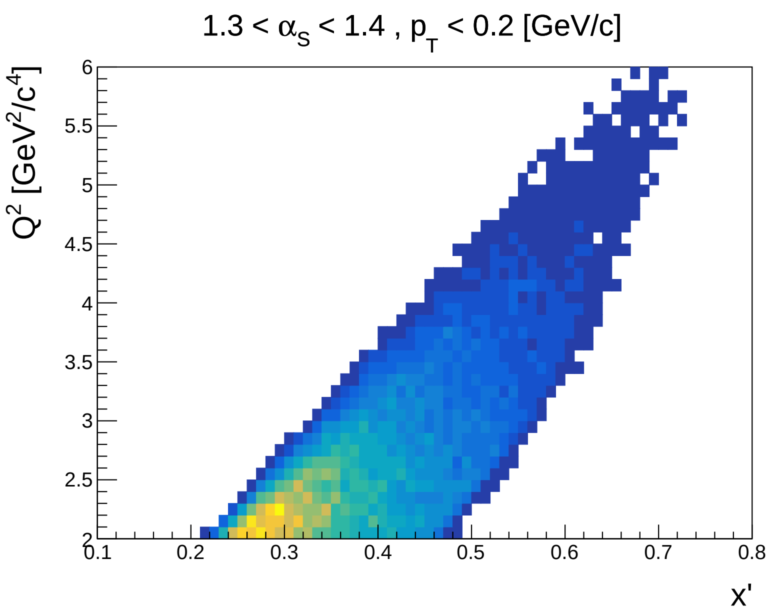

Figure 34: $x' - Q^2$ phase space for (Top): $1.3 < \alpha_S < 1.4$ and $p_T < 0.1$ GeV/c and (Bottom): $1.3 < \alpha_S < 1.4$ and $p_T < 0.2$ GeV/c. Note for higher x', higher Q^2 is probed.

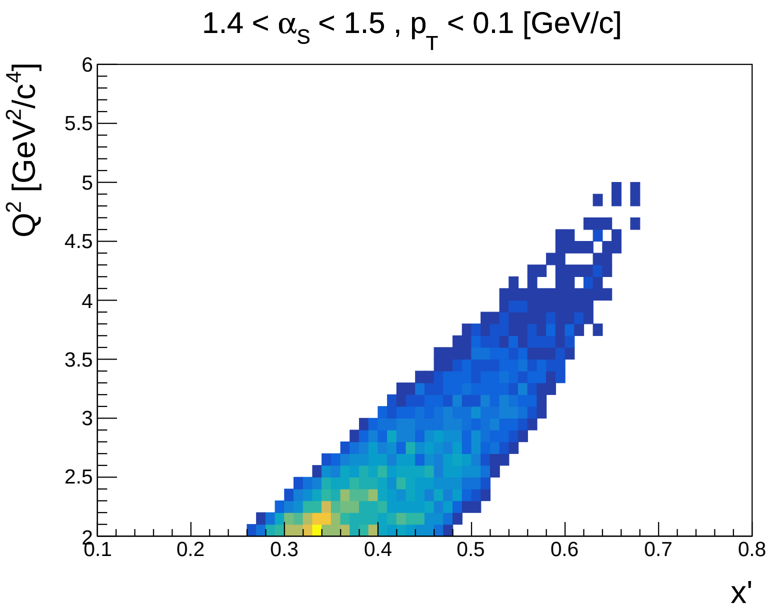

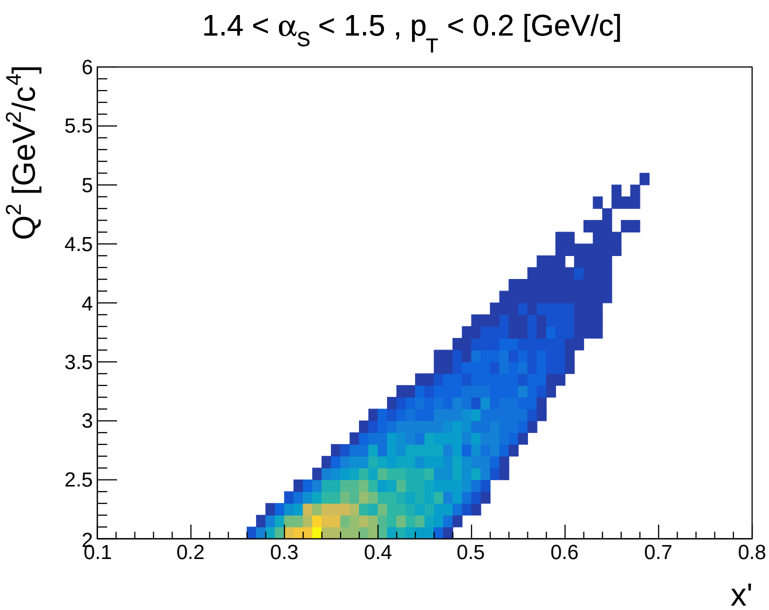

Figure 35: $x' - Q^2$ phase space for (Top): $1.4 < \alpha_S < 1.5$ and $p_T < 0.1$ GeV/c and (Bottom): $1.4 < \alpha_S < 1.5$ and $p_T < 0.2$ GeV/c. Note for higher x', higher Q^2 is probed.

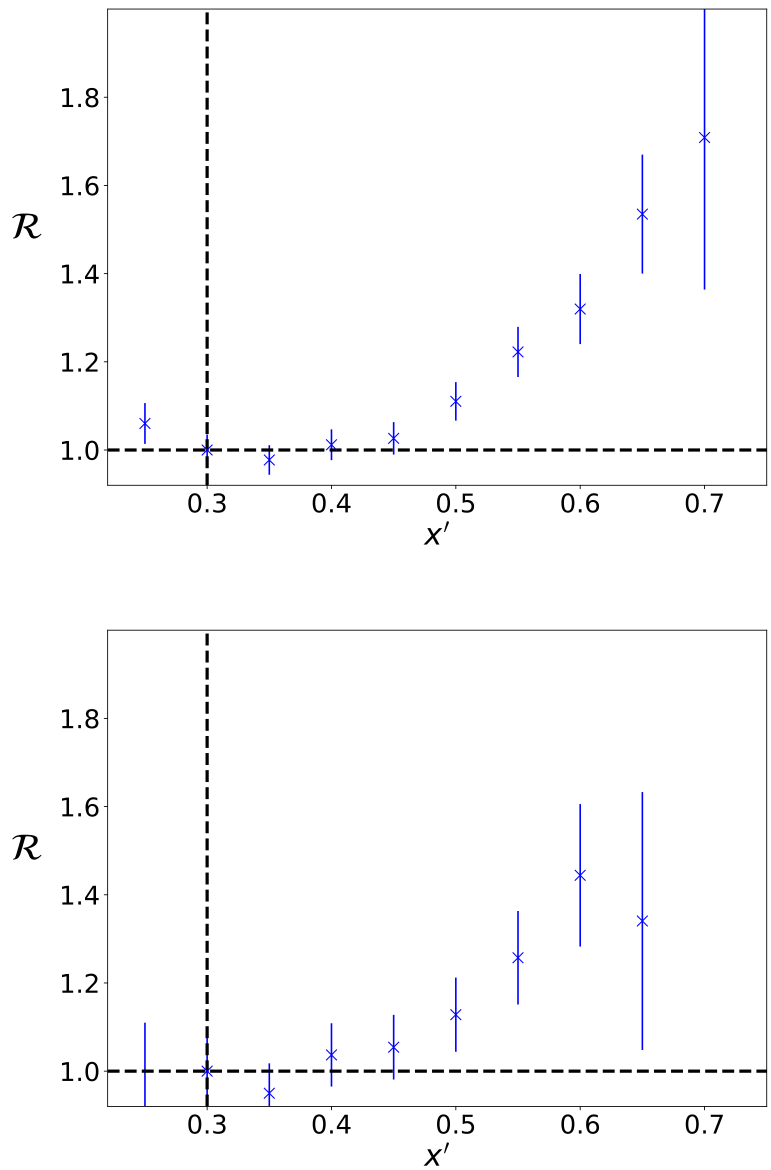

Figure 36: Double ratio results for (Top): $p_T < 0.2$ GeV/c and $1.3 < \alpha_S < 1.4$ and (Bottom): $p_T < 0.2$ GeV/c and $1.4 < \alpha_S < 1.5$.

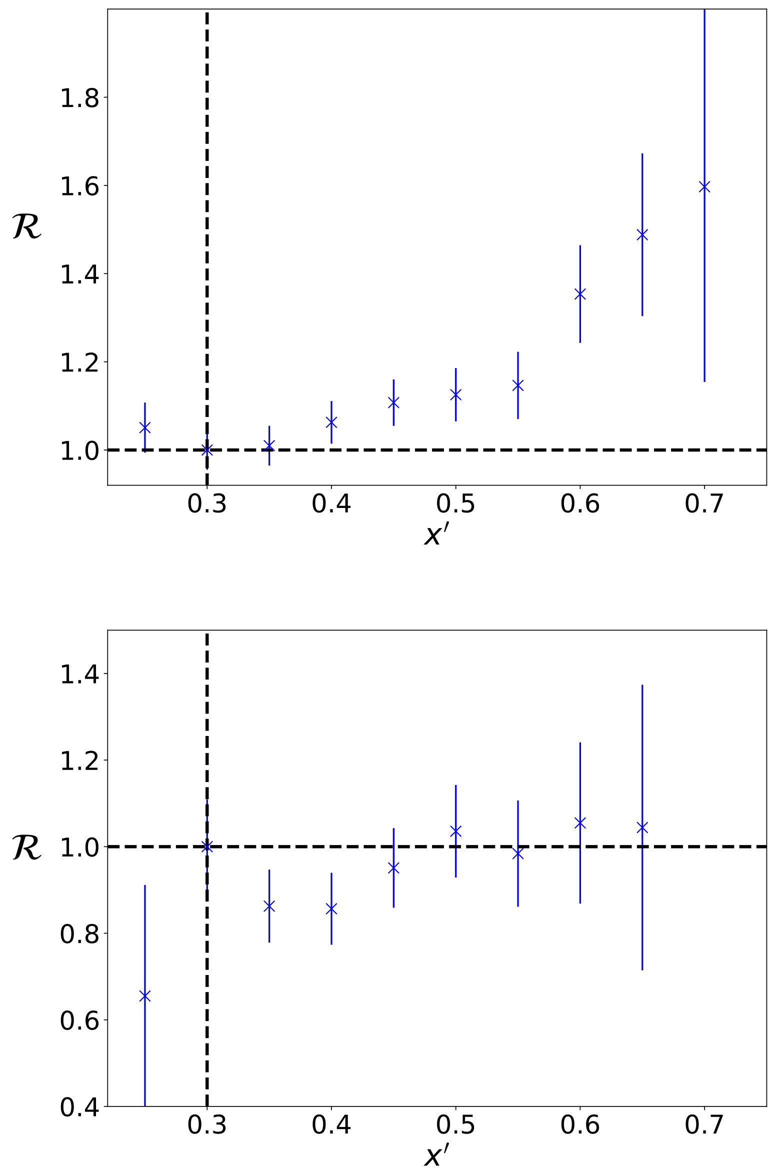

Figure 37: Double ratio results for (Top): $p_T < 0.1$ GeV/c and $1.3 < \alpha_S < 1.4$ and (Bottom): $p_T < 0.1$ GeV/c and $1.4 < \alpha_S < 1.5$.

background counts. Thus, $\delta D^2 = \delta Y^2 + \delta B^2$. As B is estimated from event-mixing, it is a combination of the statistics of the full mixed sample (B_{mixed}), the statistics of the background that is contaminating the signal region (C_{scale}), and the statistics of the mixed sample that fall within the bin of interest (B_{bin}): $B = B_{\text{bin}} C_{\text{scale}}/B_{\text{mixed}}$. As such, $\delta B^2 = \left(\frac{C_{\text{scale}}}{B_{\text{mixed}}}\delta B_{\text{bin}}\right)^2 + \left(\frac{B_{\text{bin}}}{B_{\text{mix}}}\delta C_{\text{scale}}\right)^2 + \left(\frac{B_{\text{bin}}C_{\text{scale}}}{B_{\text{mix}}^2}\delta B_{\text{mix}}\right)^2$. Here, C_{scale} is taken to be negligible, and the uncertainty on the counts for Y, B_{bin}, B_{mixed}, and M is assumed to be Poissonian ($\delta M = \sqrt{N_{\text{sim}}(x', \alpha_S, p_T, Q^2)}$).

Figs. 36 and 37 indicate a strong deviation of the bound proton structure from the free proton structure as x' grows. The deviation is seen in both α_S bins for the full $p_T < 0.2$ GeV/c. In the lower bin of p_T, the modification is only seen in the lowest bin of α_S as the statistics become limited at higher α_S. An expectation of the traditional virtuality-dependent modification ($F_2^{p*} \sim F_2^p(1 + vf^{\text{off}})$) is that modification should *grow* with increasing α_S. The double ratio does not permit the study of the α_S-dependence of modification, as the ratio is normalized to 1 at $x' = 0.3$.

We also studied the consistency of the double ratio across beam energies. Figs. 38-40 show the double ratio per beam energy. The highest bin of α_S from $1.4 - 1.5$ for the lower bin of $p_T < 0.1$ is not shown per beam energy as the combined ratio already has very limited statistics (see bottom of Fig. 37). Within statistical uncertainty, all beam energies appear to be consistent with each other.

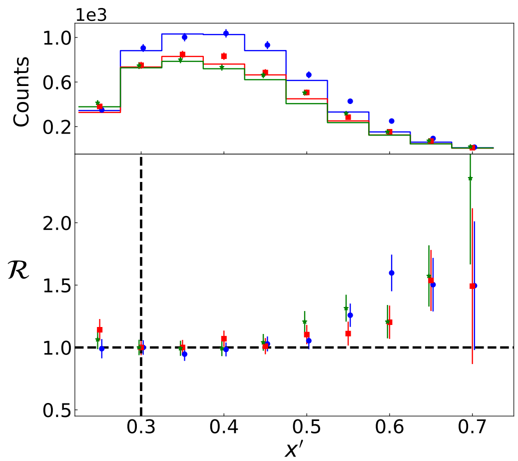

Figure 38: Double ratio results per beam energy for $p_T < 0.2$ GeV/c and $1.3 < \alpha_S < 1.4$. Blue, red, green are beam energy of 10.2 GeV, 10.4 GeV, and 10.6 GeV, respectively. (Top): Data (points) and simulation (histogram) yields are shown individually. (Bottom): double ratio $\mathcal{R}$ is shown.

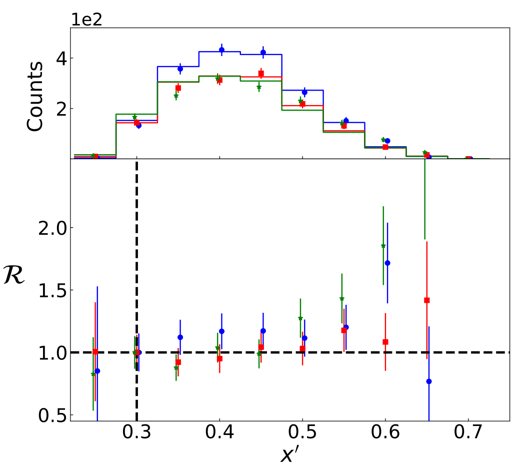

Figure 39: Double ratio results per beam energy for $p_T < 0.2$ GeV/c and $1.4 < \alpha_S < 1.5$. Blue, red, green are beam energy of 10.2 GeV, 10.4 GeV, and 10.6 GeV, respectively. (Top): Data (points) and simulation (histogram) yields are shown individually. (Bottom): double ratio $\mathcal{R}$ is shown.

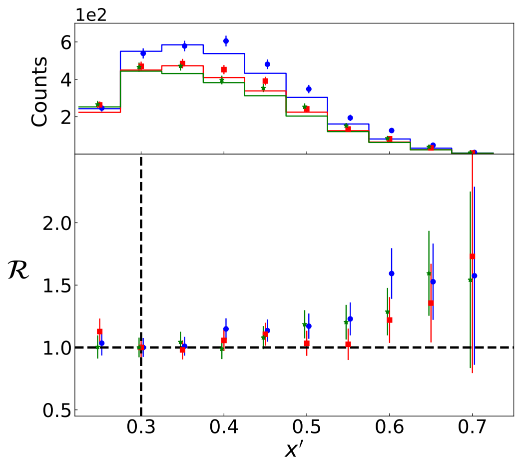

Figure 40: Results per beam energy for $p_T < 0.1$ GeV/c and $1.3 < \alpha_S < 1.4$. Blue, red, green are beam energy of 10.2 GeV, 10.4 GeV, and 10.6 GeV, respectively. (Top): Data (points) and simulation (histogram) yields are shown individually. (Bottom): double ratio $\mathcal{R}$ is shown.

9 Systematic effect on double ratio

Finalizing the systematic uncertainties for the tagged double-ratio is still in progress. These systematics include:

- Electron PID and cuts
- Neutron PID and cuts (in particular cuts on E_{dep} and p_n)
- BAND neutron detection efficiency
- Impact of finite Q^2 effects in event generator
- Model dependence of cross section model in generator

Some work has already been done on quantifying the impact of systematic effects that are expected to dominate. This is summarized below.

9.1 BAND efficiency

A systematic study was carried out to assess the impact of BAND neutron detection efficiency on R_{tag}. The numerator and denominator of R_{tag} contains the experimental and simulated yields, respectively, normalized to the yield in a fixed kinematic bin of $x' = 0.3$. Note that this cancels any overall scale disagreement in the average experimental and simulated BAND efficiencies (e.g., if the simulated and experimental efficiencies had the same shape but the simulated one was larger by a factor of 2). If the BAND efficiency was independent of neutron momentum, the experimental and simulated efficiencies would exactly cancel. However, since both the efficiency and x' depend on the neutron momentum, the efficiency does not cancel exactly. This is largely mitigated by the fact that the double ratio is extracted for bins in $alpha_S$ (which are effectively bins in neutron momentum), although momentum dependence of the efficiency across the bin could in theory impact the double ratio.

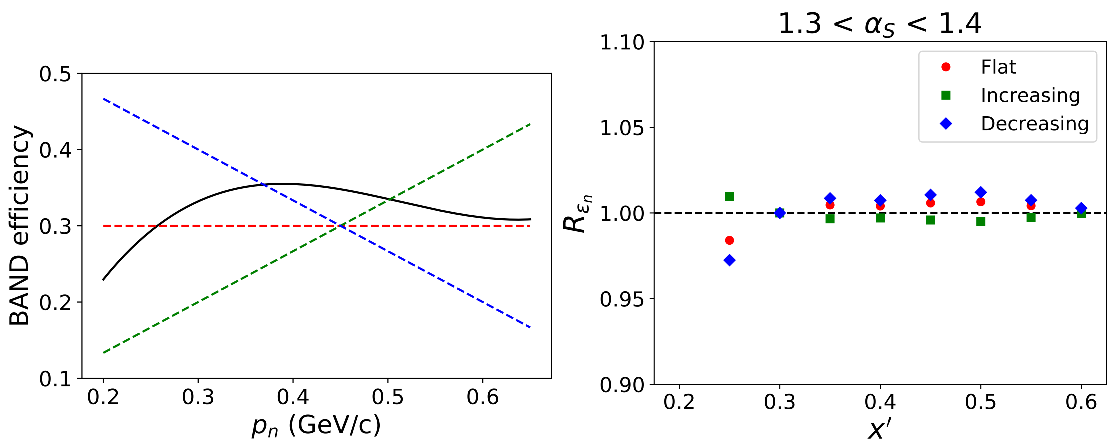

Figure 41: (left) BAND efficiency from simulation (solid black line) and an extreme range of possible efficiency curves (dashed colored lines) used to assess the impact of efficiency on R_{tag}; (right) The change in the double ratio of Fig. **??** of the different neutron efficiencies.

A simulation was performed to quantify the impact of different BAND efficiency shapes on R_{tag}. Figure 41a shows several BAND efficiency curves. The solid black line shows the efficiency obtained from an idealized simulation of BAND in GEANT4. The colored dashed lines show several possible efficiency behaviors (these are not physically motivated, but chosen to cover an extreme range of momentum dependence). Simulated events from GEMC were re-weighted by the ratio of the dashed curves to solid curve based on the neutron momentum for each event. The impact was quantified by the ratio:

$$R = \frac{Y_{standard}(x')/Y_{standard}(x' = 0.3)}{Y_{reweight}(x')/Y_{reweight}(x' = 0.3)}, \tag{21}$$

where $Y_{standard}$ is the yield from our standard GEMC simulation, and $Y_{reweight}$ is the yield reweighted to apply a different neutron efficiency. As can be seen in Figure 41b, even with these extreme variations in momentum dependence, the impact on R remains less than a few percent. Thus, the systematic uncertainty due to a possible momentum dependence of the BAND efficiency is very small.

9.2 Finite Q^2 effects

While it is common when dealing with DIS to work in the Bjorken limit ($Q^2 \to \infty$), actual experiments are performed at finite Q^2. The cross section model described in Section 2.1 is formulated in the sub-scaling limit regime. In order to assess the size of these effects, we compared these simulated results to those obtained from an asymptotic $Q^2 \to \infty$ PWIA event generator. The size of the effect was quantified by the ratio:

$$R = \frac{Y_{standard}(x')/Y_{standard}(x'=0.3)}{Y_{asymp}(x')/Y_{asymp}(x'=0.3)} \tag{22}$$

where $Y_{standard}$ is the yield from the GEMC simulation with the standard generator, and Y_{asymp} is the GEMC simulation with the asymptotic generator. As shown in Figure 42, the effect on the double ratio is less than 10%.

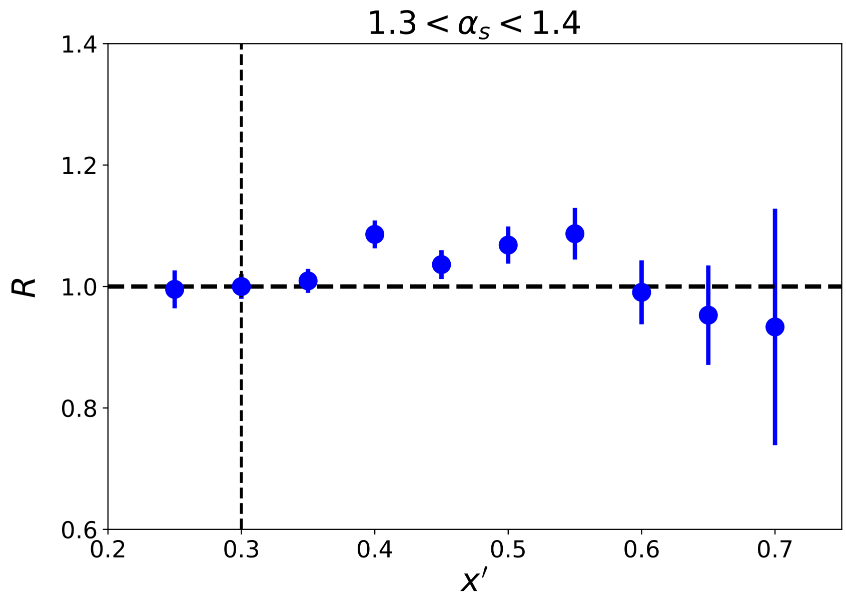

Figure 42: Double ratio comparing simulation double ratio of the finite Q^2 PWIA generator to the asymptotic $Q^2 \to \infty$ PWIA generator.

10 Conclusion

This note described the analysis of tagged DIS measurements, $d(e, e'n_S)X$, with CLAS12 and the BAND detector during the RGB data collection period in Spring 2019 and Winter 2019/2020 at various beam energies between 10-11 GeV and at about 4.2 GeV for calibration purposes. We measured a DIS electron in coincidence with a recoil spectator neutron in BAND which allows to determine nucleon modification of highly-virtual high-momentum protons in deuterium

Inclusive data to MC comparisons of the DIS electrons show good agreements giving confidence in the selection of electrons and performance of the CLAS12 detector. Comparisons of tagged neutron distributions from data and simulation also indicate a good understanding and calibration of BAND. The resulting data to simulation double ratio show a strong enhancement for large x' relative to $x' = 0.3$ which points to a strong modification of the highly-virtual protons in deuterium. Most detector related effects such as acceptances, efficiency and luminosity are canceling in this double ratio.

Initial systematic studies of BAND neutron detection efficiency and finite Q^2 effects show only a small effect. More systematic studies are still in progress but are not expected to have a significant effect compared to the statistical uncertainty.

References

[1] https://clas12mon.jlab.org/rgb/pass1/qa/rgb_spring_QA/timeline/.

[2] https://clas12mon.jlab.org/rgb/pass1/qa/rgb_fall_QA/timeline/.

[3] https://clas12mon.jlab.org/rgb/pass1/qa/rgb_winter_QA/timeline/.

[4] https://clasweb.jlab.org/wiki/images/7/70/Spring2019_final.pdf.

[5] https://clasweb.jlab.org/wiki/images/4/45/Fall2019_final.pdf.

[6] https://clasweb.jlab.org/wiki/images/a/a5/Winter2020_final.pdf.

[7] *BAND Technical Note, CLAS12Note 2022-003,* *https://misportal.jlab.org/mis/physics/clas12/viewFile.cfm/2022-003.pdf?documentId=81*.

[8] M. E. Christy and P. E. Bosted. "Empirical fit to precision inclusive electron-proton cross sections in the resonance region". In: *Phys. Rev. C* 81 (5 May 2010), p. 055213. DOI: 10.1103/PhysRevC.81.055213. URL: https://link.aps.org/doi/10.1103/PhysRevC.81.055213.

[9] CLAS Collaboration. *clasqaDB*. https://github.com/JeffersonLab/clasqaDB. 2021.

[10] *CLAS12 RG-A - Analysis Note Overview and Procedures (Level-1):* *https://www.jlab.org/Hall-B/shifts/admin/paper_reviews/2020/RGA_Analysis_Overview_and_Procedures_Nov_4_2020-6245173-2020-12-09-v3.pdf*. 2021.

[11] Wim Cosyn and Misak Sargsian. "Final-state interactions in semi-inclusive deep inelastic scattering off the Deuteron". In: *Phys. Rev. C* 84 (2011), p. 014601. DOI: 10.1103/PhysRevC.84.014601. arXiv: 1012.0293 [nucl-th].

[12] R. Ent et al. "Radiative corrections for $(e, e^{'} p)$ reactions at GeV energies". In: *Phys. Rev. C* 64 (5 Oct. 2001), p. 054610. DOI: 10.1103/PhysRevC.64.054610. URL: https://link.aps.org/doi/10.1103/PhysRevC.64.054610.

[13] L.L. Frankfurt and M.I. Strikman. "High-energy phenomena, short-range nuclear structure and QCD". In: *Physics Reports* 76.4 (1981), pp. 215–347. ISSN: 0370-1573. DOI: https://doi.org/10.1016/0370-1573(81)90129-0. URL: https://www.sciencedirect.com/science/article/pii/0370157381901290.

[14] M. Strikman and C. Weiss. “Electron-deuteron deep-inelastic scattering with spectator nucleon tagging and final-state interactions at intermediate x”. In: *Phys. Rev. C* 97 (3 Mar. 2018), p. 035209. DOI: 10.1103/PhysRevC.97.035209. URL: https://link.aps.org/doi/10.1103/PhysRevC.97.035209.

A Open issues

A.1 Known analysis issues

Here we give a short summary on known issues in the analysis and what has been done or is being done

A.1.1 Lower BAND efficiency from data than simulation

We determined the BAND efficiency from the low-energy run of RGB by using quasi-elastic $d(e,e'pn)$ and $d(e,e'p)X$ events. When comparing to simulation, we obtained about a factor of 2 less efficiency in data. This factor is independent on energy deposition cuts, BAND fiduciual cuts, extra smearing of electrons. However, a difference in efficiency does not impact the double ratio significantly as shown in Sec. 9.1. We also plan to use higher-statistics from RGM in the future to map the BAND efficiency accross the detector.

A.1.2 Data/MC discrepancy in absolute rate

The comparisons for inclusive and tagged data are normalized to each other. When the data/MC ratio is normalized by the luminosity the ratio differs for inclusive by $\sim 0.6 - 0.7$ while for tagged events it is $\sim 7 - 10$. We compared multiple event generators with the same result. However, the double ratio minimizes sensitivity to the absolute rate.

A.1.3 Peak in BAND TOF spectrum around 34ns

In the TOF spectrum with a loose $E_{dep} > 2\,\text{MeVee}$ cut and no fiducial cut on BAND, a peak around 34 ns is observed (see Fig. 43) which is much enhanced compared to the surrounding photon and neutron peak convoluted with peaks from the CEBAF 4 ns beam structure. We studied the distribution of events in this peak area and found that it is more concentrated in the top bars of bars. Therefore, the top 3 bars in each of the BAND layers were removed by the BAND fiducial cuts. Furthermore, the 34-ns peak is also suppressed by the analysis $E_{dep} > 10\,\text{MeVee}$ cut.

A.1.4 Peak in E_{dep} distribution around 10 MeVee

In Fig. 44 the energy deposited by BAND hits is compared between MC and data. We observe a peak around 10 MeVee in data which is not visible in MC. This

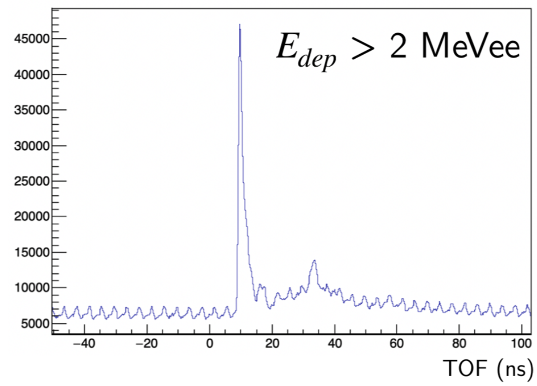

Figure 43: BAND TOF spectrum with and $E_{dep} > 2\,\text{MeVee}$ cut and electron in CLAS12. Beam bunch structure of 4 ns is visible together with photon peak and neutron shoulder. There is also an unusual peak around 34 ns.

peak only occurs for neutron momenta between $0.25 GeV$ and $0.275 GeV$. It is not correlated with the peak in the TOF spectrum (see previous section). We also note the difference in the energy spectrum for values above 20 MeVee. This is due to the limited dynamic range of the FADCs and overflow of the signal amplitude, hence some of the signal strength is cut in the digitization. This behaviour is not simulated in GEMC. However, the overflow of the signal amplitude has no effect on the data analysis itself since events pass anyway the energy deposition cuts and the time-walk correction is very small for large amplitudes.

A.2 Questions raised by committee

Questions in Sebastian's email from July 10 as response to first informal meeting on July 07

1. Can you explain the last 3 slides in your presentation? I am quite interested to look at the spectrum from the empty target vs. the full LD2 target, but I can't tell whether you apply the same cuts (and how they are normalized relative to each other). Obviously, it can't be literally true that the empty target spectra are much larger than the LD2 ones.

2. Could you send me the simply experimental ratio $Y(x')/Y(x' = 0.3)$ for the two α_S bins, $1.3 - 1.4$ and $1.4 - 1.5$? No corrections - just the ratio of counts.

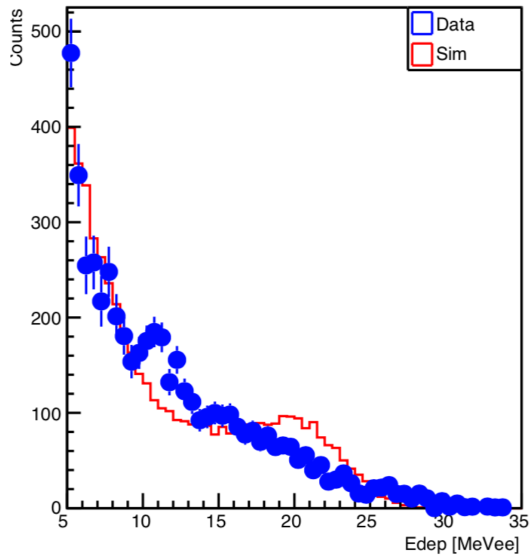

Figure 44: Comparison of BAND energy deposition between data and GEMC.

3. For an ABSOLUTE comparison, I would just need the unnormalized yields $Y(x')$ for the 2 α_S bins themselves, plus the integrated luminosity corresponding to the runs that you integrate over. I would think that I should be able to get an answer to better than within a factor of 7.

Response:

1. The last 3 slides show the TOF for BAND hits that have passed veto algorithm and been identified as the good neutron hit candidate (short, of course, of TOF cut). The distributions for full and empty targets have been normalized by luminosity. If they were simply normalized by charge, you would see that the empty target rates are orders of magnitude lower than full target rates.

2. to be done

3. to be done

Followup questions by Sebastian on empty target runs (July 12, 2022):

1. For these 3 slides, did you apply all of the DIS and spectator cuts in your slides, also including the vertex cut?

2. For the latter, does it remove the exit and entrance windows? It would be useful to see a vertex distribution for both empty and full target with all cuts.

3. When you say that if they were normalized by charge, the rates are "orders of magnitude lower" - can you quantify that? E.g., for the 10 MeVee case, the neutron peak appears to be at least 3x larger for the empty than for the full target - by which factor would that be reduced if you would normalize by FC instead?

Response: to be done

B Tagged data/MC comparisons

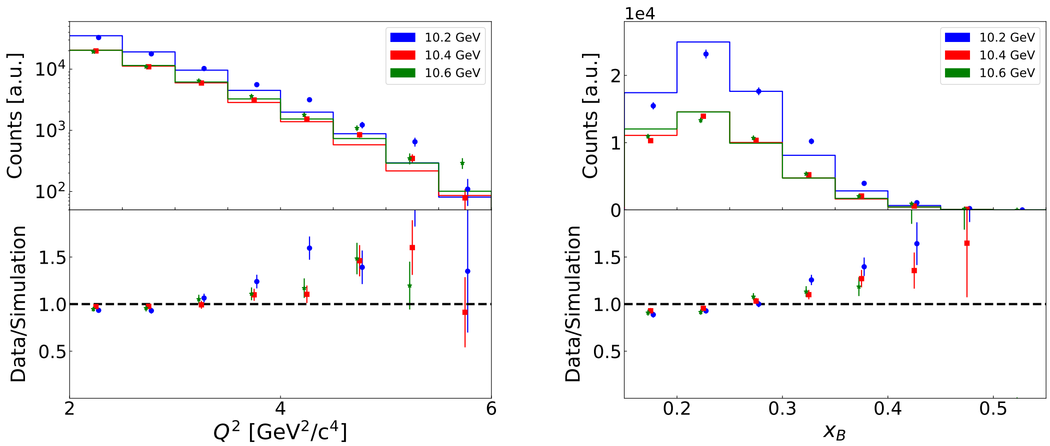

Figure 45: (Left): Q^2. (Right): x_B. Distributions of data (points) and simulation (histogram) per beam energy.

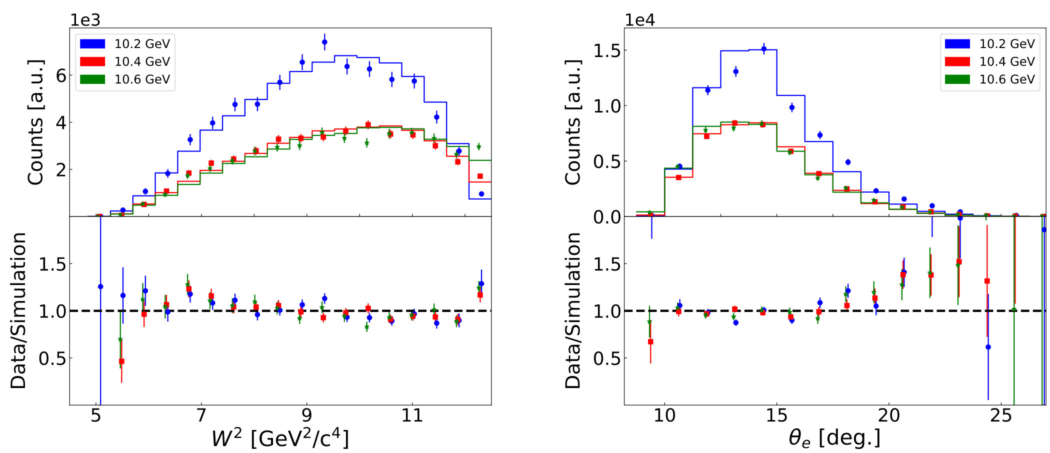

Figure 46: (Left): W^2 (Right): θ_e. Distributions of data (points) and simulation (histogram) per beam energy.

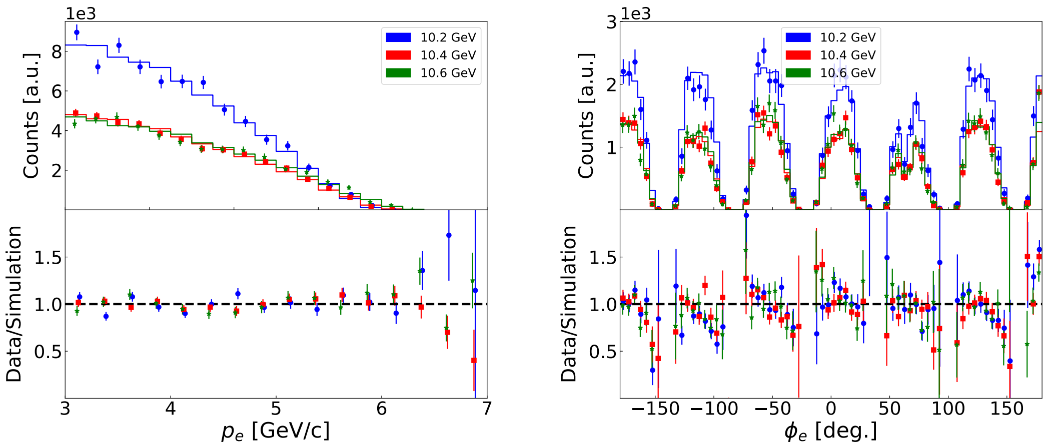

Figure 47: (Left): p_e (Right): ϕ_e. Distributions of data (points) and simulation (histogram) per beam energy.

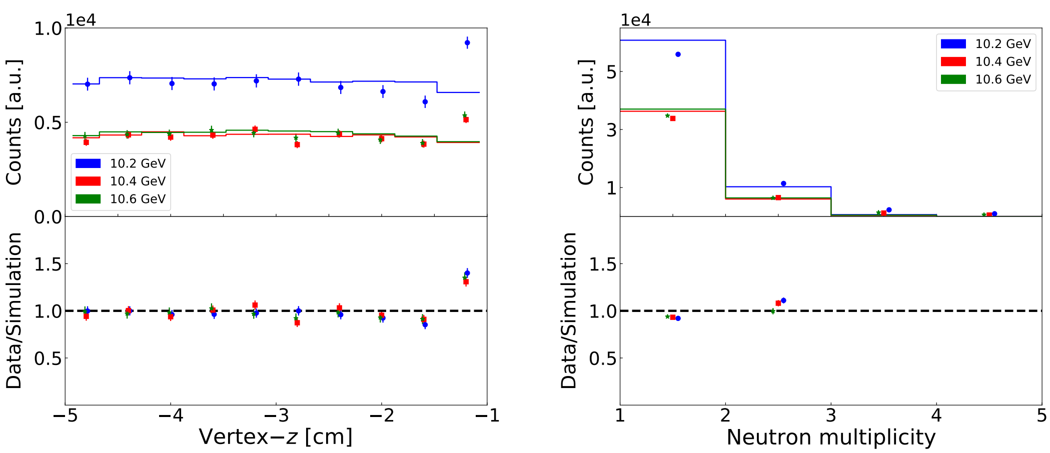

Figure 48: (Left): Vertex-z (Right): Neutron multiplicity. Distributions of data (points) and simulation (histogram) per beam energy.

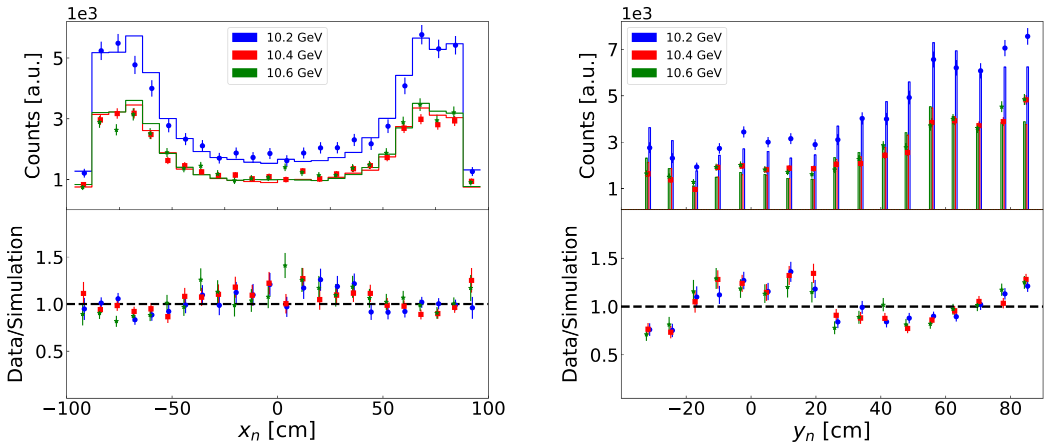

Figure 49: (Left): x_n (Right): y_n. Distributions of data (points) and simulation (histogram) per beam energy.

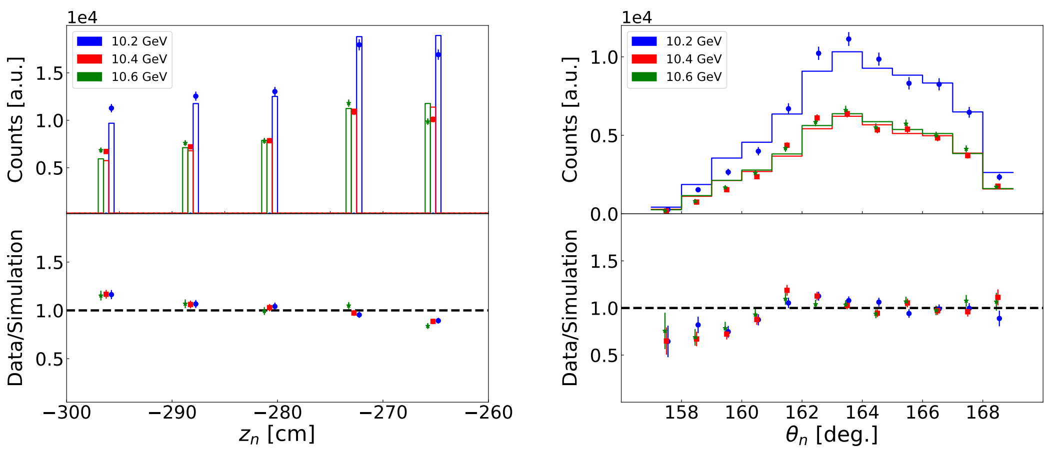

Figure 50: (Left): z_n (Right): θ_n. Distributions of data (points) and simulation (histogram) per beam energy.

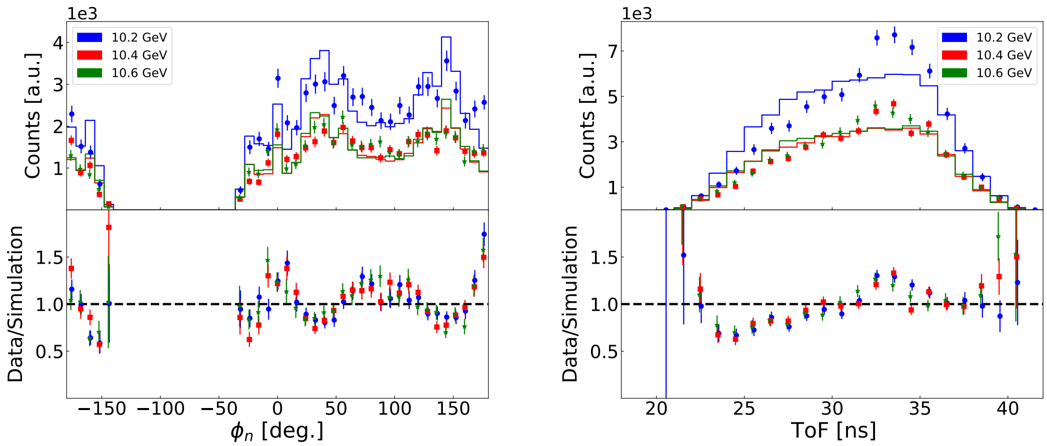

Figure 51: (Left): ϕ_n (Right): ToF. Distributions of data (points) and simulation (histogram) per beam energy.

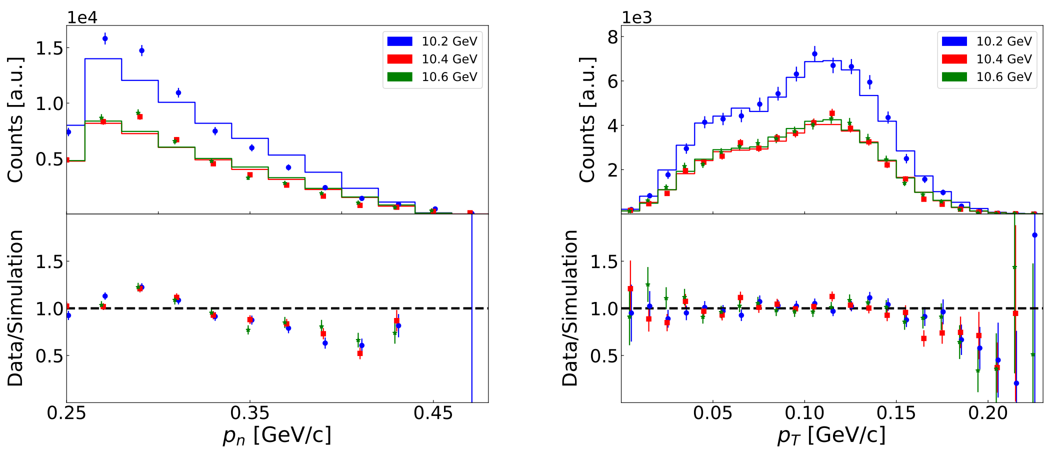

Figure 52: (Left): p_n (Right): p_T. Distributions of data (points) and simulation (histogram) per beam energy.

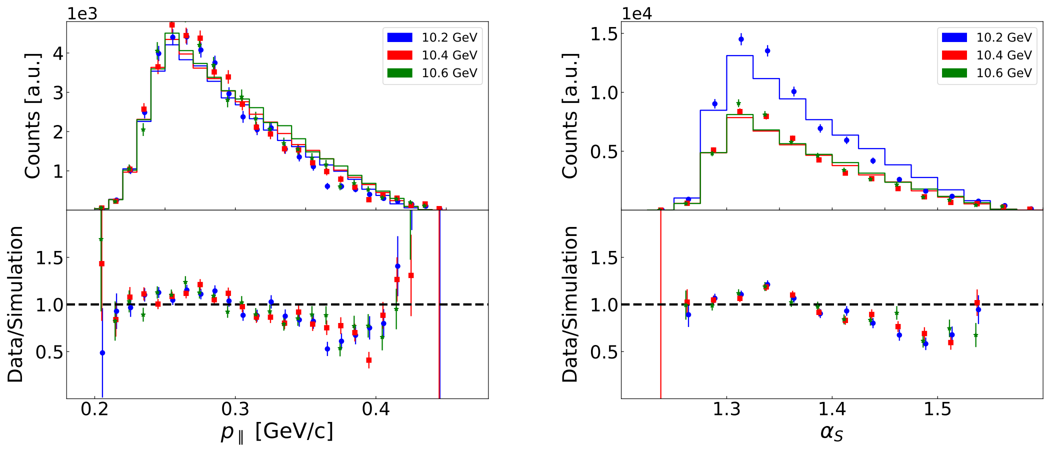

Figure 53: (Left): $p_{\parallel}$ (Right): α_S. Distributions of data (points) and simulation (histogram) per beam energy.

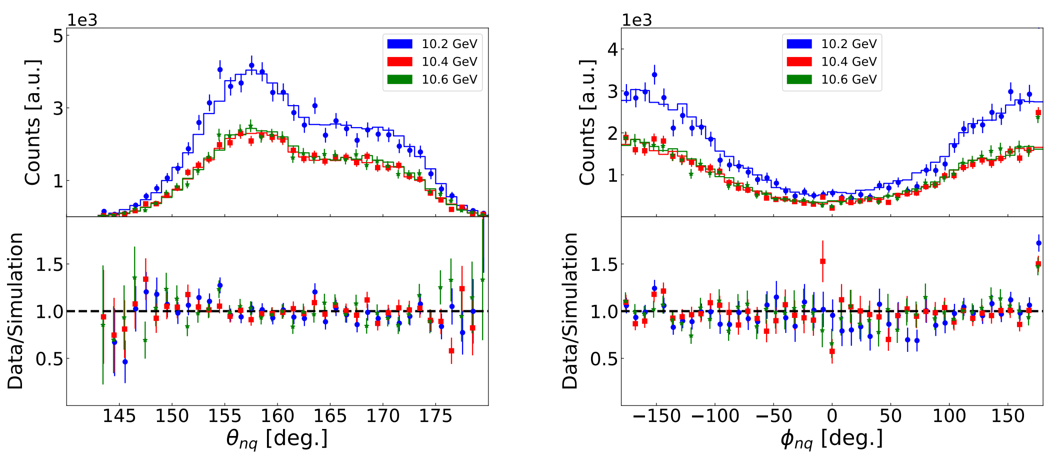

Figure 54: (Left): θ_{nq} (Right): ϕ_{nq}. Distributions of data (points) and simulation (histogram) per beam energy.

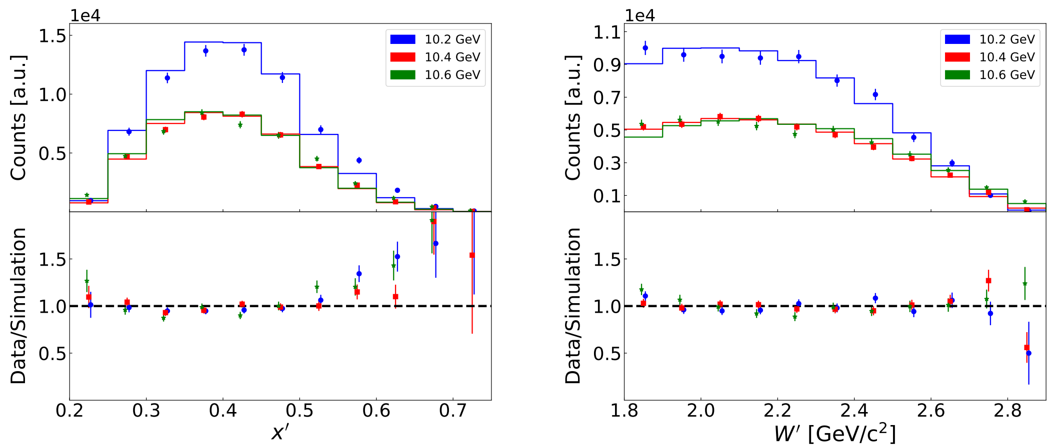

Figure 55: (Left): x' (Right): W'. Distributions of data (points) and simulation (histogram) per beam energy.

C Good Run Selection Plots

C.1 10.2 GeV Good Runs

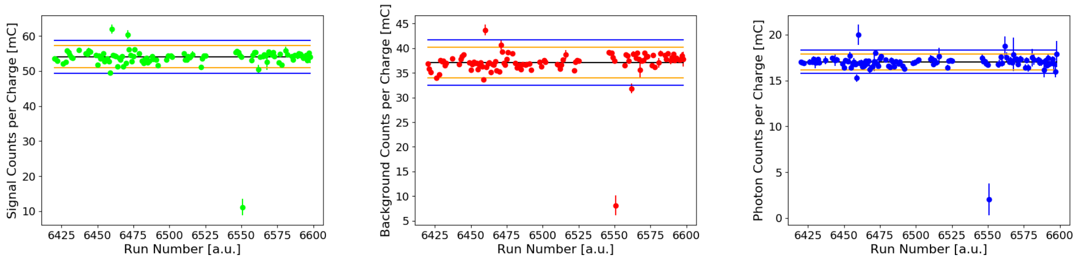

Figure 56: The counts per charge as a function of run number for the 10.2 GeV period. The black line is the mean while the orange and blue lines show the 2σ and 3σ lines respectively.

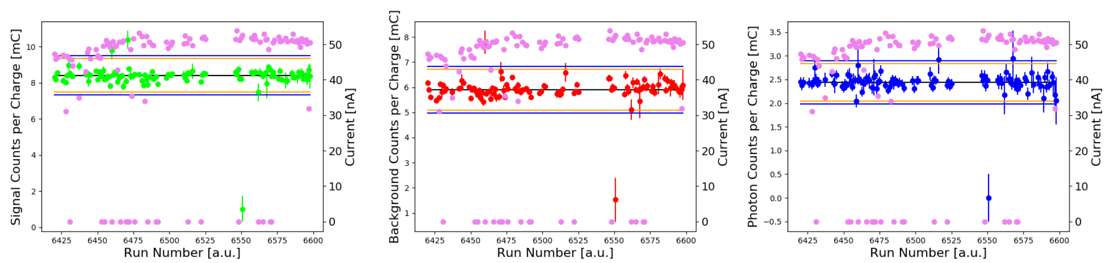

Figure 57: The counts per charge for BAND Layer 1 as a function of run number for the 10.2 GeV period. The black line is the mean while the orange and blue lines show the 3.5σ and 4σ lines respectively. The "violet" points are the current.

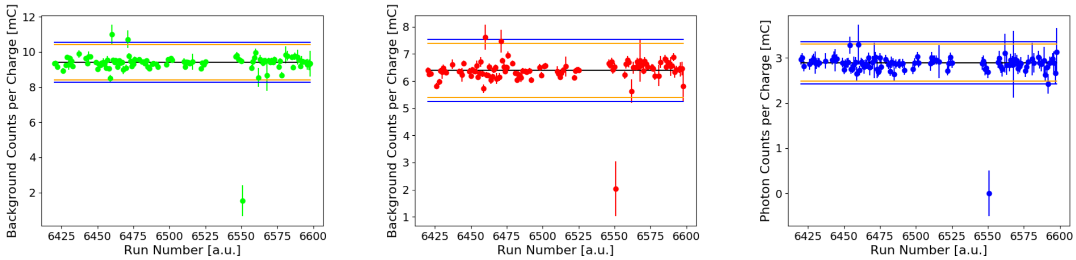

Figure 58: The counts per charge for BAND Layer 2 as a function of run number for the 10.2 GeV period. The black line is the mean while the orange and blue lines show the 3.5σ and 4σ lines respectively.

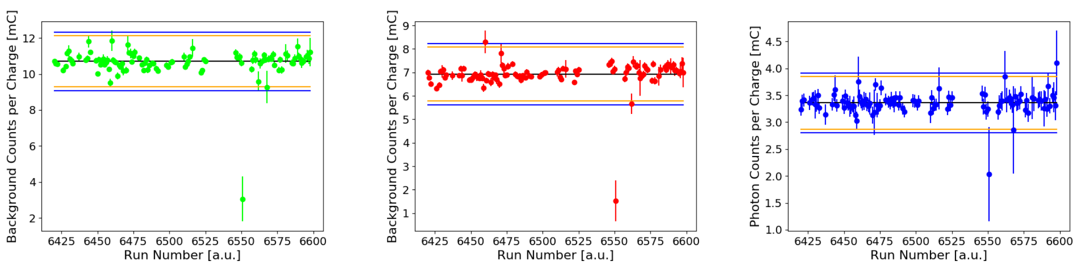

Figure 59: The counts per charge for BAND Layer 3 as a function of run number for the 10.2 GeV period. The black line is the mean while the orange and blue lines show the 3.5σ and 4σ lines respectively.

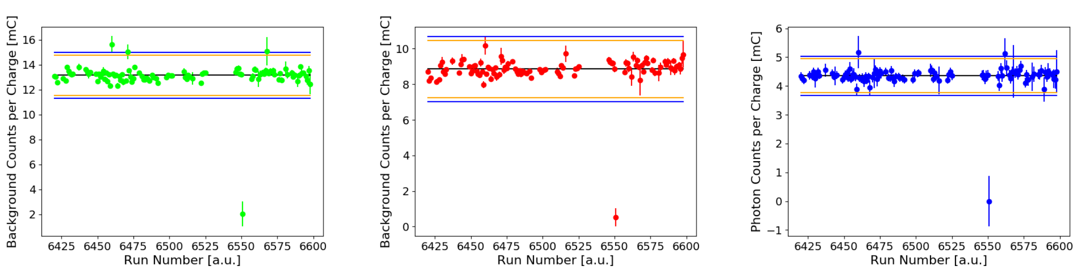

Figure 60: The counts per charge for BAND Layer 4 as a function of run number for the 10.2 GeV period. The black line is the mean while the orange and blue lines show the 3.5σ and 4σ lines respectively.

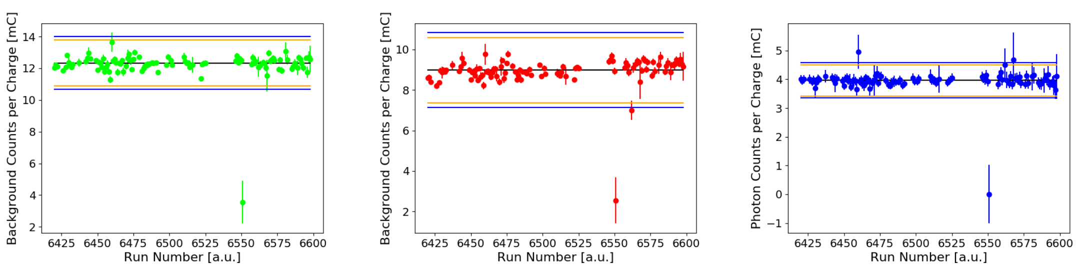

Figure 61: The counts per charge for BAND Layer 5 as a function of run number for the 10.2 GeV period. The black line is the mean while the orange and blue lines show the 3.5σ and 4σ lines respectively.

C.2 10.6 GeV Good Runs

C.2.1 Epoch 1

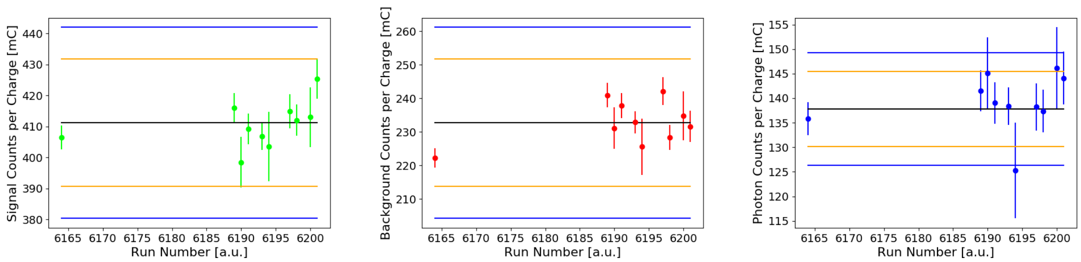

Figure 62: The counts per charge as a function of run number for epoch 1 in the 10.6 GeV period. The black line is the mean while the orange and blue lines show the 2σ and 3σ lines respectively.

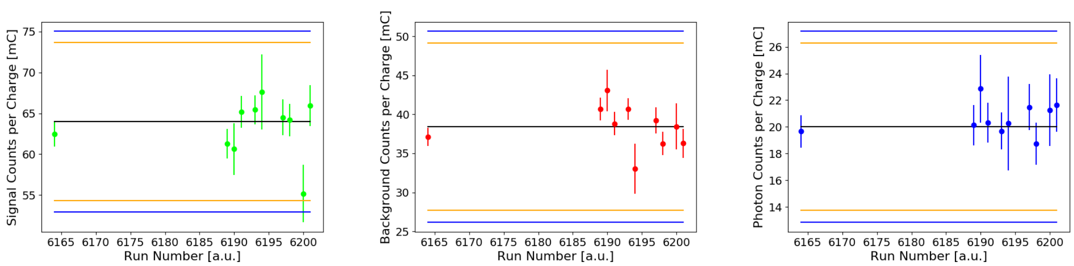

Figure 63: The counts per charge for BAND Layer 1 as a function of run number for epoch 1 in the 10.6 GeV period. The black line is the mean while the orange and blue lines show the 3.5σ and 4σ lines respectively. The "violet" points are the current.

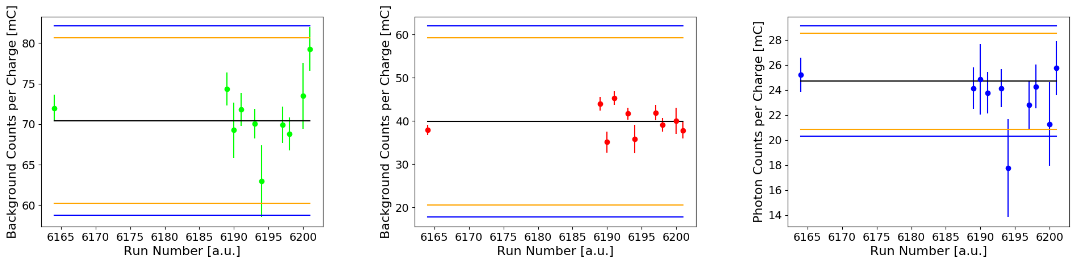

Figure 64: The counts per charge for BAND Layer 2 as a function of run number for epoch 1 in the 10.6 GeV period. The black line is the mean while the orange and blue lines show the 3.5σ and 4σ lines respectively.

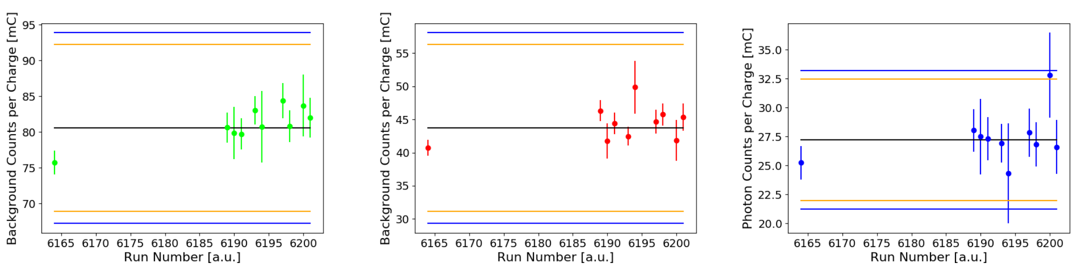

Figure 65: The counts per charge for BAND Layer 3 as a function of run number for epoch 1 in the 10.6 GeV period. The black line is the mean while the orange and blue lines show the 3.5σ and 4σ lines respectively.

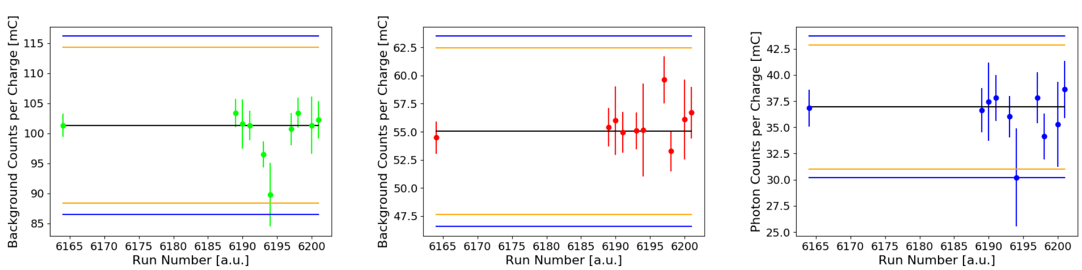

Figure 66: The counts per charge for BAND Layer 4 as a function of run number for epoch 1 in the 10.6 GeV period. The black line is the mean while the orange and blue lines show the 3.5σ and 4σ lines respectively.

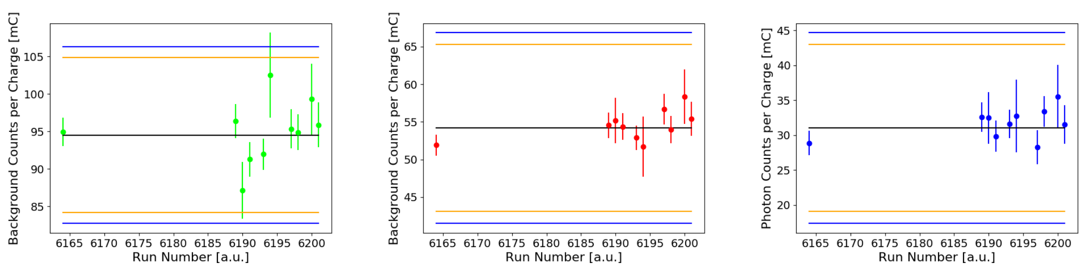

Figure 67: The counts per charge for BAND Layer 5 as a function of run number for epoch 1 in the 10.6 GeV period. The black line is the mean while the orange and blue lines show the 3.5σ and 4σ lines respectively.

C.2.2 Epoch 2

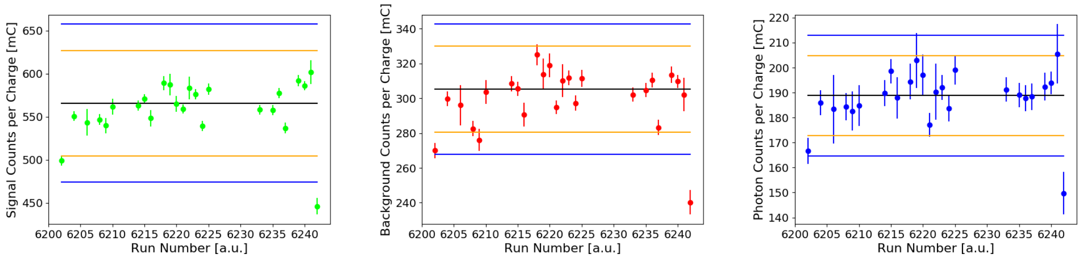

Figure 68: The counts per charge as a function of run number for epoch 2 in the 10.6 GeV period. The black line is the mean while the orange and blue lines show the 2σ and 3σ lines respectively.

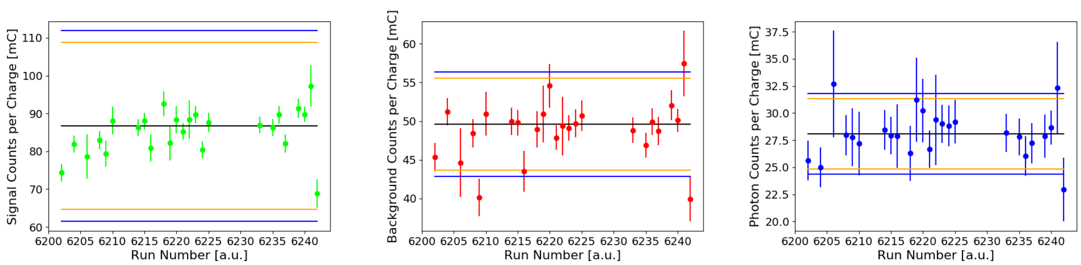

Figure 69: The counts per charge for BAND Layer 1 as a function of run number for epoch 2 in the 10.6 GeV period. The black line is the mean while the orange and blue lines show the 3.5σ and 4σ lines respectively. The "violet" points are the current.

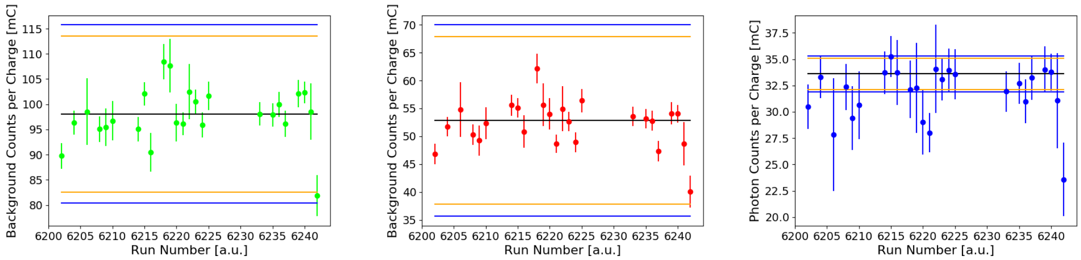

Figure 70: The counts per charge for BAND Layer 2 as a function of run number for epoch 2 in the 10.6 GeV period. The black line is the mean while the orange and blue lines show the 3.5σ and 4σ lines respectively.

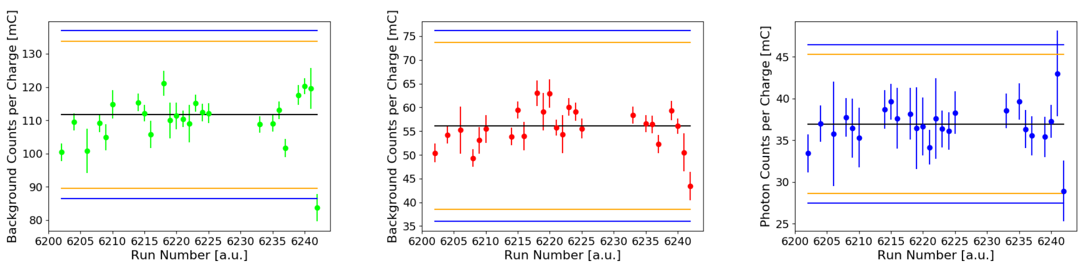

Figure 71: The counts per charge for BAND Layer 3 as a function of run number for epoch 2 in the 10.6 GeV period. The black line is the mean while the orange and blue lines show the 3.5σ and 4σ lines respectively.

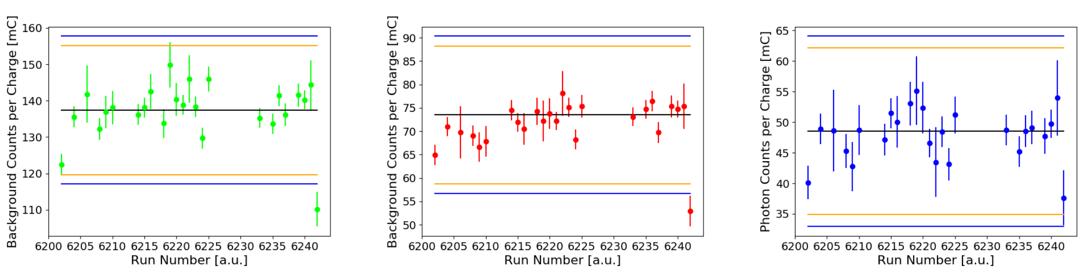

Figure 72: The counts per charge for BAND Layer 4 as a function of run number for epoch 2 in the 10.6 GeV period. The black line is the mean while the orange and blue lines show the 3.5σ and 4σ lines respectively.

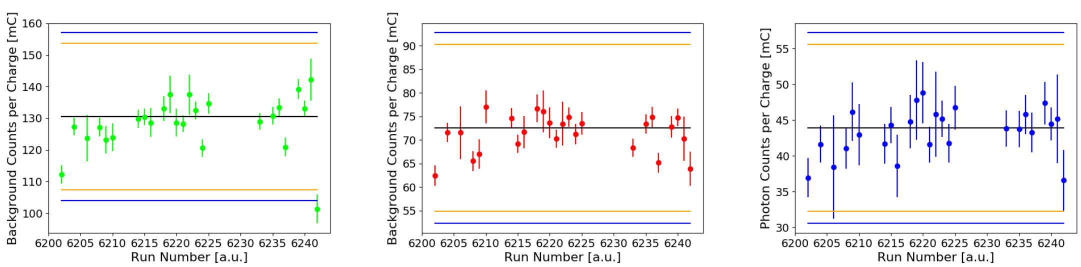

Figure 73: The counts per charge for BAND Layer 5 as a function of run number for epoch 2 in the 10.6 GeV period. The black line is the mean while the orange and blue lines show the 3.5σ and 4σ lines respectively.

C.2.3 Epoch 3

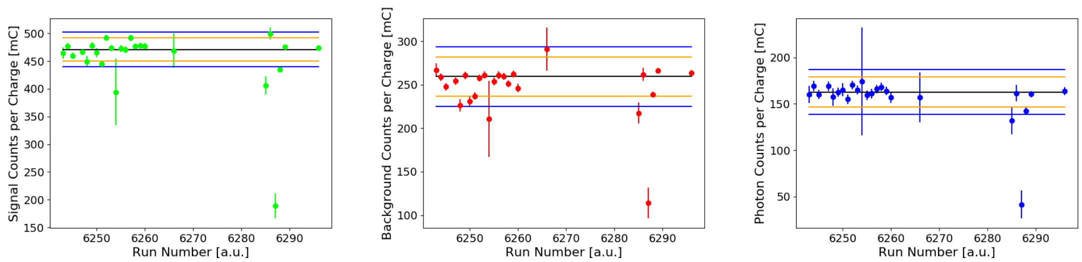

Figure 74: The counts per charge as a function of run number for epoch 3 in the 10.6 GeV period. The black line is the mean while the orange and blue lines show the 2σ and 3σ lines respectively.

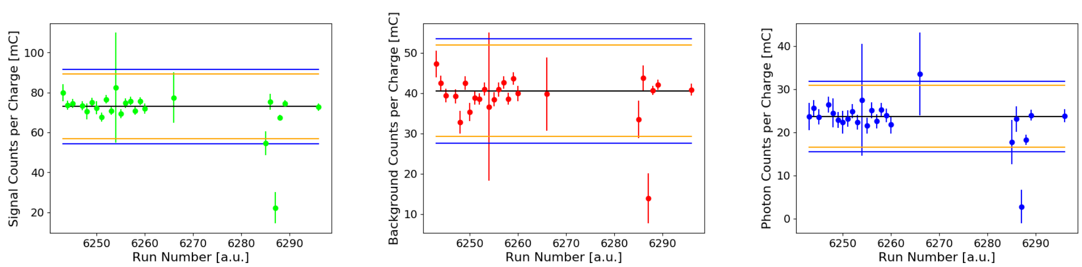

Figure 75: The counts per charge for BAND Layer 1 as a function of run number for epoch 3 in the 10.6 GeV period. The black line is the mean while the orange and blue lines show the 3.5σ and 4σ lines respectively. The ”violet” points are the current.

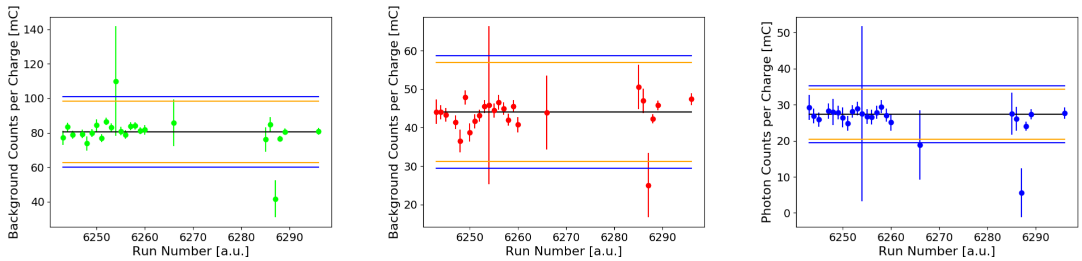

Figure 76: The counts per charge for BAND Layer 2 as a function of run number for epoch 3 in the 10.6 GeV period. The black line is the mean while the orange and blue lines show the 3.5σ and 4σ lines respectively.

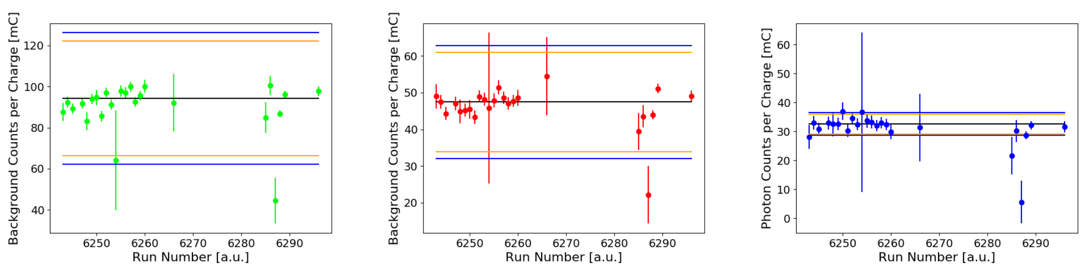

Figure 77: The counts per charge for BAND Layer 3 as a function of run number for epoch 3 in the 10.6 GeV period. The black line is the mean while the orange and blue lines show the 3.5σ and 4σ lines respectively.

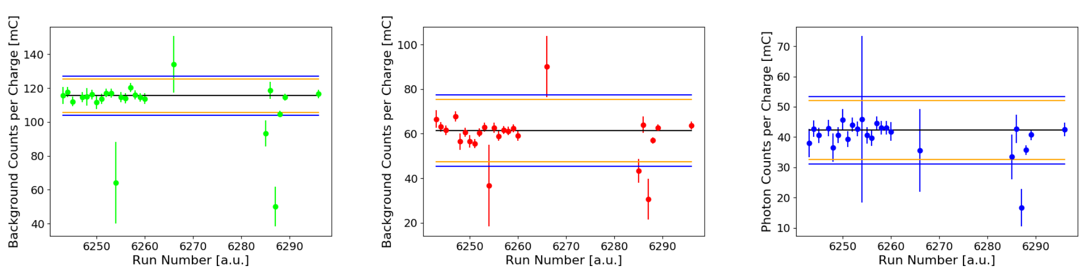

Figure 78: The counts per charge for BAND Layer 4 as a function of run number for epoch 3 in the 10.6 GeV period. The black line is the mean while the orange and blue lines show the 3.5σ and 4σ lines respectively.

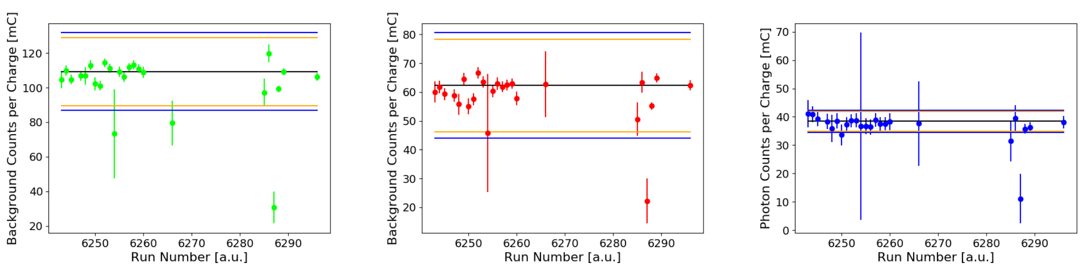

Figure 79: The counts per charge for BAND Layer 5 as a function of run number for epoch 3 in the 10.6 GeV period. The black line is the mean while the orange and blue lines show the 3.5σ and 4σ lines respectively.

C.2.4 Epoch 4

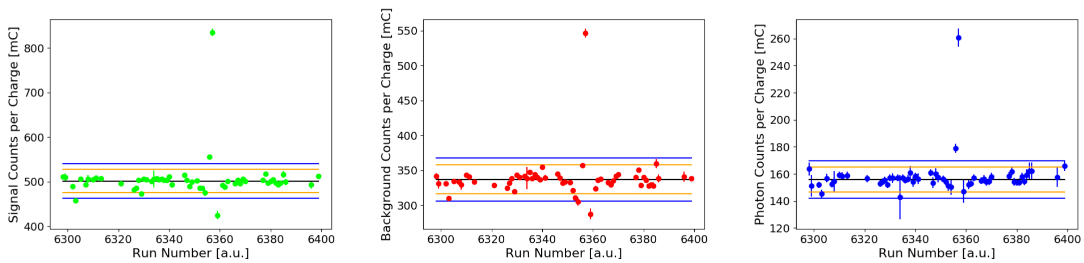

Figure 80: The counts per charge as a function of run number for epoch 4 in the 10.6 GeV period. The black line is the mean while the orange and blue lines show the 2σ and 3σ lines respectively.

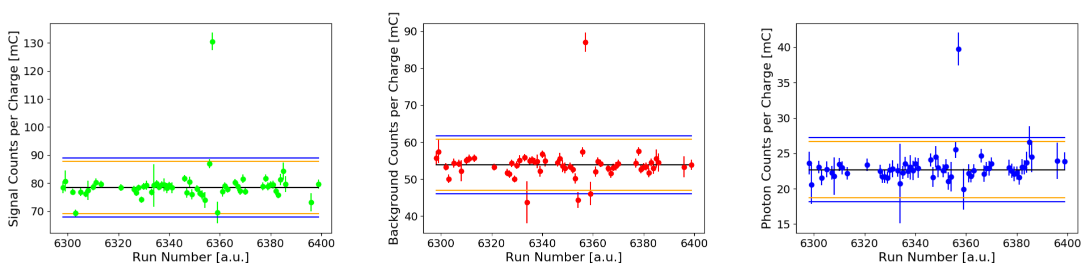

Figure 81: The counts per charge for BAND Layer 1 as a function of run number for epoch 4 in the 10.6 GeV period. The black line is the mean while the orange and blue lines show the 3.5σ and 4σ lines respectively. The ”violet” points are the current.

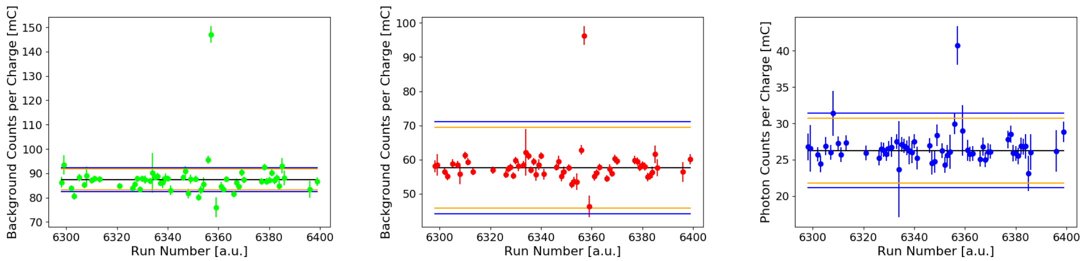

Figure 82: The counts per charge for BAND Layer 2 as a function of run number for epoch 4 in the 10.6 GeV period. The black line is the mean while the orange and blue lines show the 3.5σ and 4σ lines respectively.

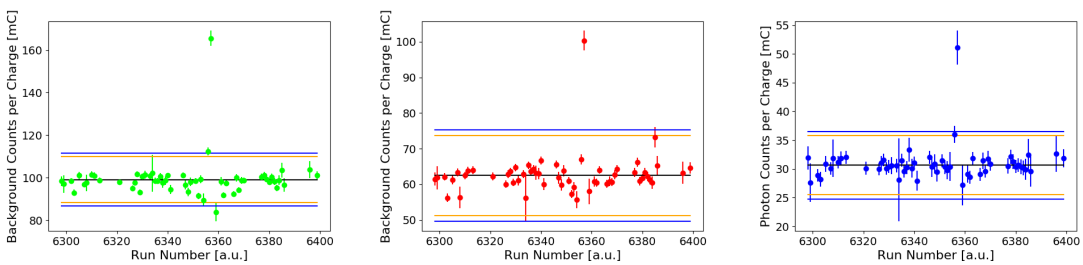

Figure 83: The counts per charge for BAND Layer 3 as a function of run number for epoch 4 in the 10.6 GeV period. The black line is the mean while the orange and blue lines show the 3.5σ and 4σ lines respectively.

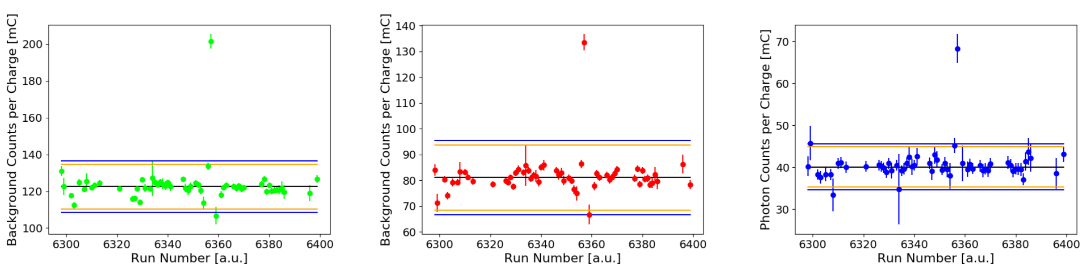

Figure 84: The counts per charge for BAND Layer 4 as a function of run number for epoch 4 in the 10.6 GeV period. The black line is the mean while the orange and blue lines show the 3.5σ and 4σ lines respectively.

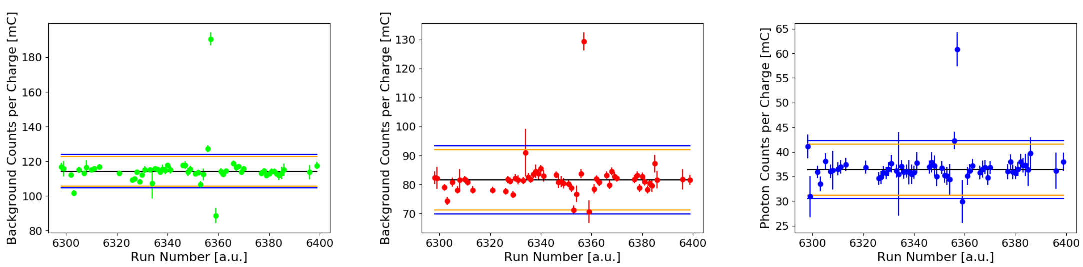

Figure 85: The counts per charge for BAND Layer 5 as a function of run number for epoch 4 in the 10.6 GeV period. The black line is the mean while the orange and blue lines show the 3.5σ and 4σ lines respectively.

C.3 Low-Energy Runs (LERs)

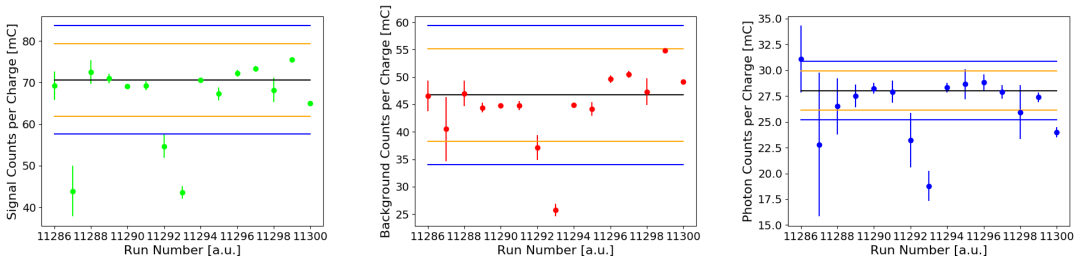

Figure 86: The counts per charge as a function of run number for the LER period. The black line is the mean while the orange and blue lines show the 2σ and 3σ lines respectively.

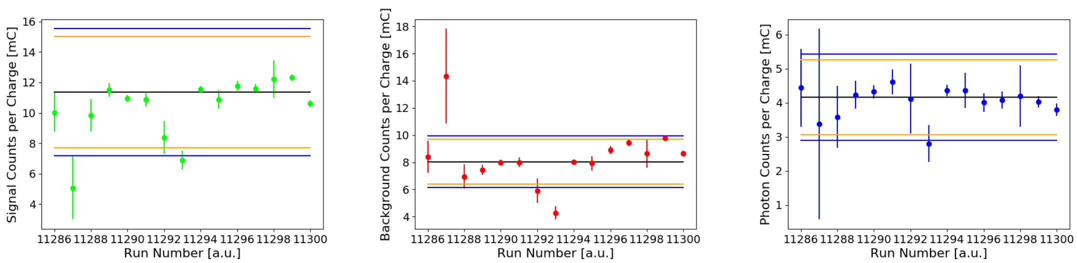

Figure 87: The counts per charge for BAND Layer 1 as a function of run number for the LER period. The black line is the mean while the orange and blue lines show the 3.5σ and 4σ lines respectively.

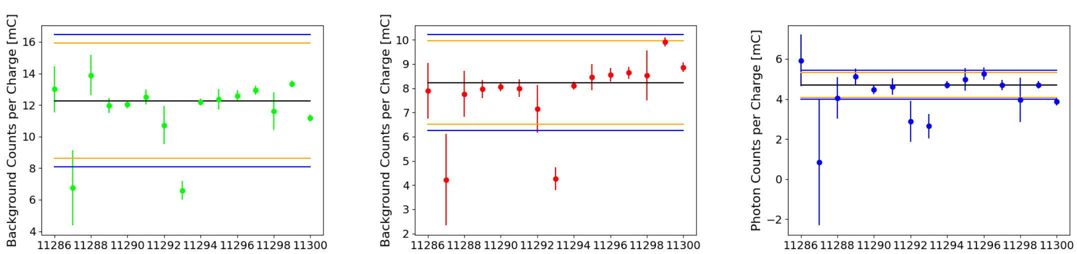

Figure 88: The counts per charge for BAND Layer 2 as a function of run number for the LER period. The black line is the mean while the orange and blue lines show the 3.5σ and 4σ lines respectively.

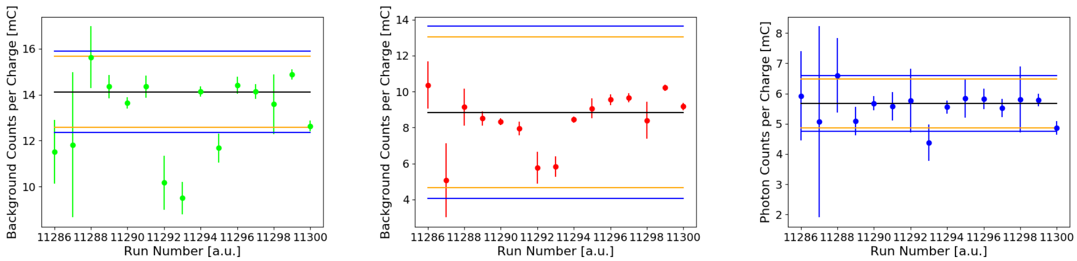

Figure 89: The counts per charge for BAND Layer 3 as a function of run number for the LER period. The black line is the mean while the orange and blue lines show the 3.5σ and 4σ lines respectively.

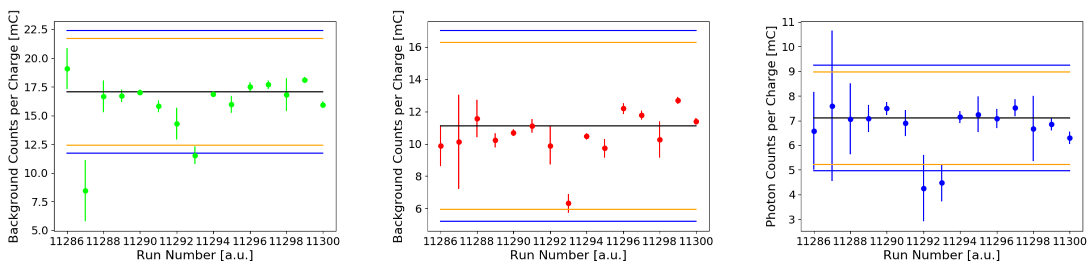

Figure 90: The counts per charge for BAND Layer 4 as a function of run number for the LER period. The black line is the mean while the orange and blue lines show the 3.5σ and 4σ lines respectively.

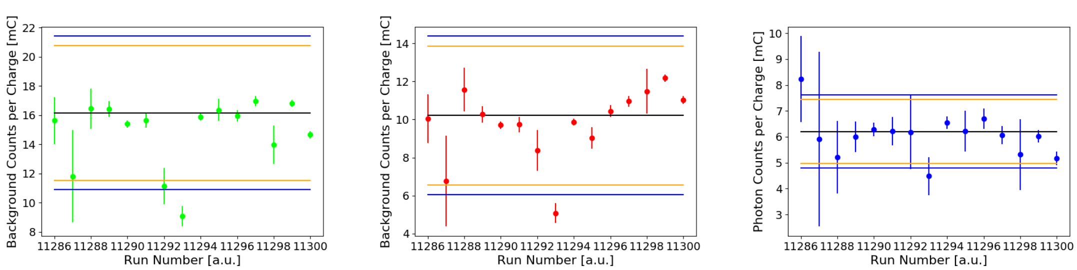

Figure 91: The counts per charge for BAND Layer 5 as a function of run number for the LER period. The black line is the mean while the orange and blue lines show the 3.5σ and 4σ lines respectively.

C.4 10.4 GeV Good Runs

C.4.1 Epoch 1

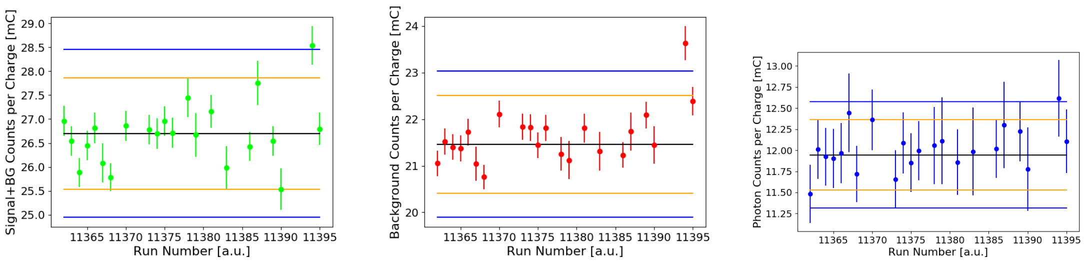

Figure 92: The counts per charge as a function of run number for epoch 1 in the 10.4 GeV period. The black line is the mean while the orange and blue lines show the 2σ and 3σ lines respectively.

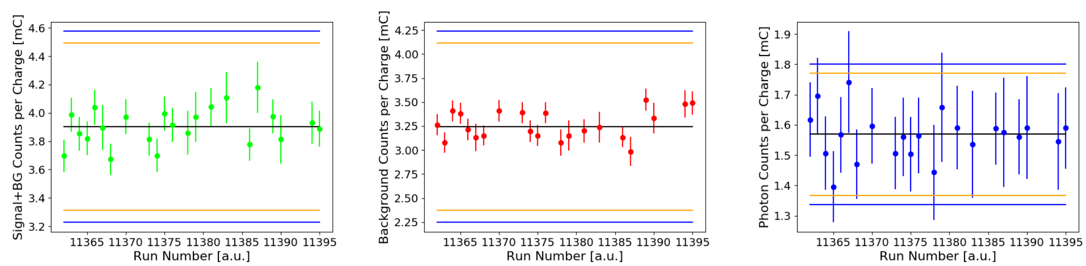

Figure 93: The counts per charge for BAND Layer 1 as a function of run number for epoch 1 in the 10.4 GeV period. The black line is the mean while the orange and blue lines show the 3.5σ and 4σ lines respectively. The ”violet” points are the current.

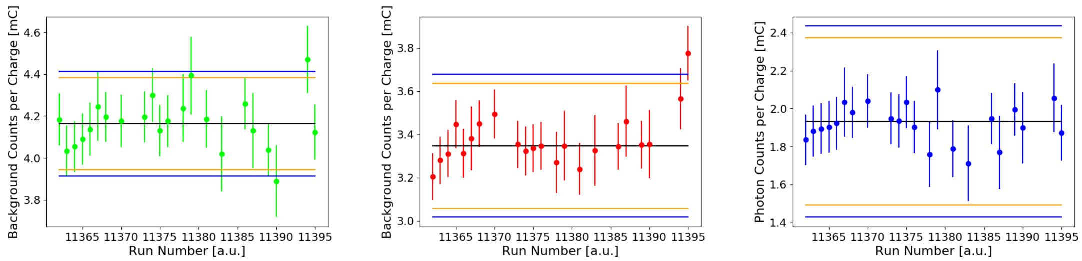

Figure 94: The counts per charge for BAND Layer 2 as a function of run number for epoch 1 in the 10.4 GeV period. The black line is the mean while the orange and blue lines show the 3.5σ and 4σ lines respectively.

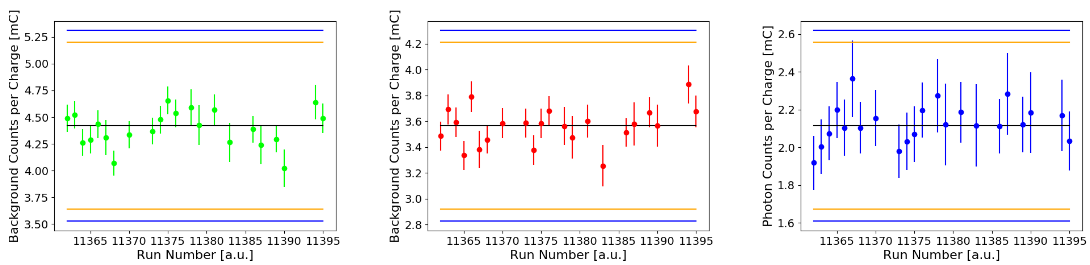

Figure 95: The counts per charge for BAND Layer 3 as a function of run number for epoch 1 in the 10.4 GeV period. The black line is the mean while the orange and blue lines show the 3.5σ and 4σ lines respectively.

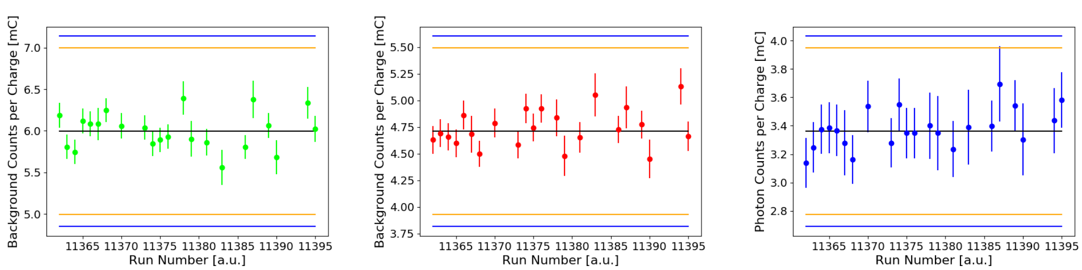

Figure 96: The counts per charge for BAND Layer 4 as a function of run number for epoch 1 in the 10.4 GeV period. The black line is the mean while the orange and blue lines show the 3.5σ and 4σ lines respectively.

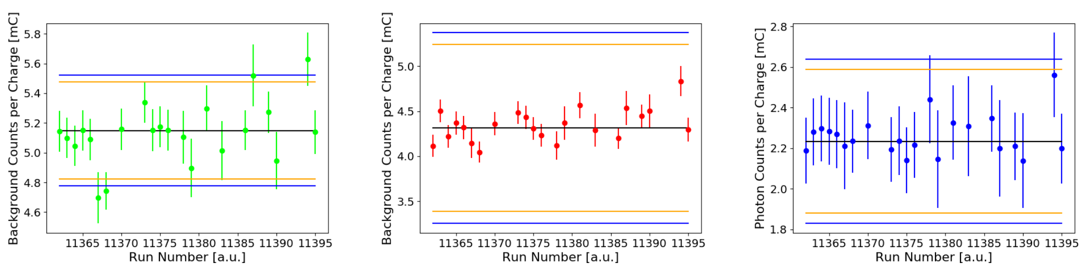

Figure 97: The counts per charge for BAND Layer 5 as a function of run number for epoch 1 in the 10.4 GeV period. The black line is the mean while the orange and blue lines show the 3.5σ and 4σ lines respectively.

C.4.2 Epoch 2

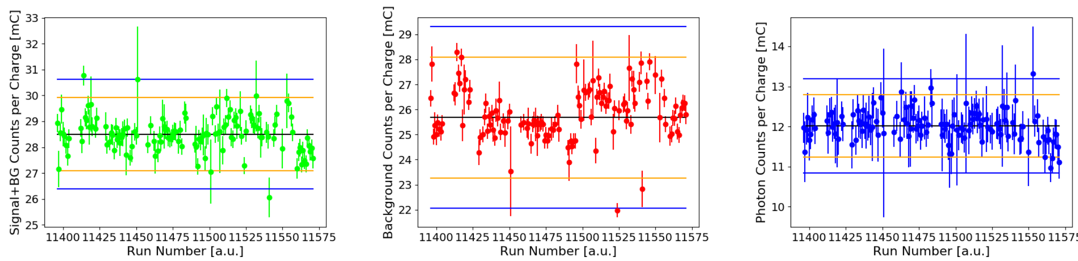

Figure 98: The counts per charge as a function of run number for epoch 2 in the 10.4 GeV period. The black line is the mean while the orange and blue lines show the 2σ and 3σ lines respectively.

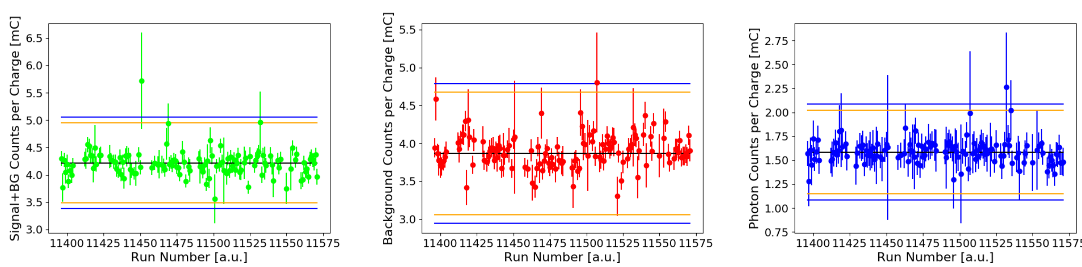

Figure 99: The counts per charge for BAND Layer 1 as a function of run number for epoch 2 in the 10.4 GeV period. The black line is the mean while the orange and blue lines show the 3.5σ and 4σ lines respectively. The "violet" points are the current.

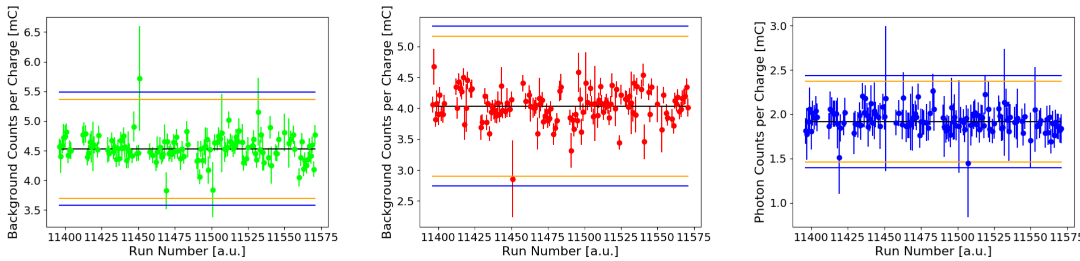

Figure 100: The counts per charge for BAND Layer 2 as a function of run number for epoch 2 in the 10.4 GeV period. The black line is the mean while the orange and blue lines show the 3.5σ and 4σ lines respectively.

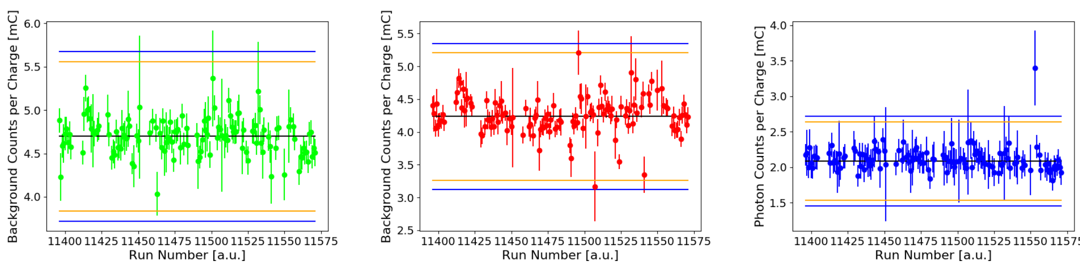

Figure 101: The counts per charge for BAND Layer 3 as a function of run number for epoch 2 in the 10.4 GeV period. The black line is the mean while the orange and blue lines show the 3.5σ and 4σ lines respectively.

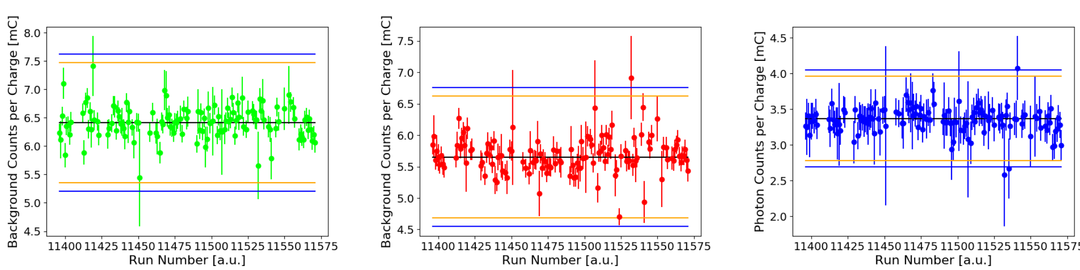

Figure 102: The counts per charge for BAND Layer 4 as a function of run number for epoch 2 in the 10.4 GeV period. The black line is the mean while the orange and blue lines show the 3.5σ and 4σ lines respectively.

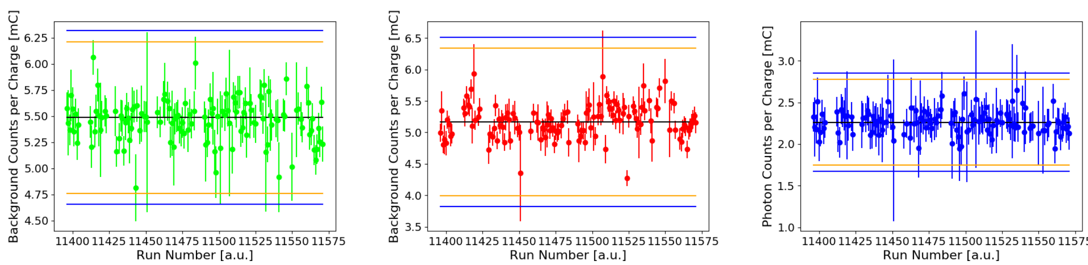

Figure 103: The counts per charge for BAND Layer 5 as a function of run number for epoch 2 in the 10.4 GeV period. The black line is the mean while the orange and blue lines show the 3.5σ and 4σ lines respectively.